Development and Optimization of Polymeric Carriers for Lymphatic Imaging and Drug Delivery

By

Taryn R. Bagby

B.S., Chemistry, Kansas State University, 2006

M.S., Pharmaceutical Chemistry, University of Kansas, 2009

Submitted to the graduate degree program in Pharmaceutical Chemistry and the Graduate Faculty of the University of Kansas in partial fulfillment of the requirements for the degree of Doctor of Philosophy.

Chairperson: Dr. M. Laird Forrest

Dr. Cory Berkland

Dr. Jeffery Krise

Dr. Valentino Stella

Dr. Xinmai Yang

Date Defended: September 23, 2011

The Dissertation Committee for Taryn R. Bagby

certifies that this is the approved version of the following dissertation:

Development and Optimization of Polymeric Carriers for Lymphatic
Imaging and Drug Delivery

Chairperson: Dr. M. Laird Forrest

Date approved: December 13, 2011

Abstract

Many cancers, including melanoma and breast cancer, metastasize via the lymphatic system, a mono-directional network of vessels and nodes that parallels the circulatory system. Accurate determination of the lymph nodes involved in the early lymphatic spread of the primary tumor is paramount for survival of the patient. Melanoma and breast cancer, when detected early offer promising 5-year survival rates of more than 90%; however, once the metastases have spread beyond the lymph node basin draining the primary tumor, the typical first metastatic site, to successive lymph nodes or organs, the 5-year survival dramatically drops to less than 20%. However, conventional systemic chemotherapy offers limited penetration into the lymphatic to treat lymphatic metastases, and often the dose limiting toxicities associated with systemic chemotherapy limit the dose to below that needed for effective treatment. Therefore, there is a great need to develop localized treatment and imaging agents for the delivery and identification of the tumor lymphatics and metastases, which can offer enhanced detection and improved efficacy and reduced toxicity over systemic therapy. Specific targeting of the lymphatics is possible by utilizing the natural structure of the lymphatic capillaries by tailoring the size and charge of the carriers to 10 to 100 nm in diameter and modifying the surface charge to be neutral to anionic in nature.

Herein this dissertation focuses on the development and optimization of two different polymeric platforms for enhanced lymphatic uptake by tailoring the size and degree of anionic charge, utilizing hyaluronan and star polymers, respectively, as intralymphatic delivery platforms for the use in imaging and treatment of lymphatically metastatic cancers, such as melanoma and breast cancer. Further, the development of a geldanamycin-polymer conjugate utilizing the

optimized star polymer and evaluation of its efficacy in three orthotopic tumor models for melanoma and breast cancer will also be discussed.

This dissertation is dedicated to my husband Tom and my parents Mary and Larry for their unconditional love and support.

Acknowledgements

First, I would like to express my gratitude to my advisor, Dr. Laird Forrest, for his guidance, encouragement, and support throughout my graduate career.

I would also like to thank my committee members, Drs. Cory Berkland, Jeffery Krise, Valentino Stella, and Xinmai Yang for taking time out of their busy schedules to serve on my committee, and for all of their valuable insight and suggestions throughout my graduate career. In particular, I would like to thank Drs. Forrest, Berkland, and Krise, for reading my dissertation and providing helpful and insightful feedback.

Without the following people, this dissertation would not be possible: Sharadvi Thati for the endless hours of imaging data analysis, animal work and cell culture; Dr. Shuang Cai and Qiuhong Yang for help with all of the animal work; Dr. Shaofeng Duan for his amazing synthetic chemistry knowledge and expertise; Grace Unruh and Lei Cheung for their assistance with cell culture; and Dr. Sarah Kieweg and Thora Whitmore for the assistance with the rheometry.

To all of the past and present Forrest Lab members that I have had the pleasure to work with, my day to day lab experience would not have been the same without you: David Hart, Dr. Yumei Xie, Dr. Shuang Cai, Dr. Hassam-Mustafa Diab, Shara Thati, Dr. Padmaja Gunda, Yomna Badawi, Dr. Yepeng Luan, Jason Christian, Dr. Shaofeng Duan, Qiuhong Yang, Yunqi Zhao, Ti Zhang, Adel Alhowyan, Lei Cheung, and Grace Unruh. A special thank you to David Hart for teaching me the power of the “5-question rule”; without this advice, both myself and many others would not have personally grown as scientists by learning to think for yourself and to not rely solely on others.

My time at the University of Kansas would not have been the same without the many friends that I made (in no particular order): Dr. Courtney (Kuhnline) Sloan, Dr. Diana Sperger,

Maria (Thorson) Feeney, Dr. Brooke Barrett, Shara Thati, Dr. Bob Berendt, Dr. Natalie Ciaccio, Sarah Pyszczynski, Elodie Dempah, Dr. Kelly Desino, Dr. Dan Mudra, Dr. Allyn Kaufmann, Dr. Leon van Haandel, Justin Thomas, Yomna Badawi, Dr. Ahmed Badawi, Josh Woods, Dr. Joshua Sestak, Dr. Ryan Funk, Randy Logan, Jessica Creamer, Jessica Haywood, Bo Pornputtapitak, Qiuhong Yang, Dr. Yumei Xie, Talia Martin, Dr. Mary Krause, Dr. Barlas Buyuktimkin, and Alana Toro-Ramos. I would also like to thank the incoming class of 2006, Dr. Chuda Chitaspuphoo and Dr. Supang Khondee, although we were a small class, it was a pleasure getting to know and work with the both of you. A special thank you to Nancy Helm, for her friendship, encouragement, support, and her constant reassurance with the words "hang in there kiddo."

Thank you, Shuang, Shara, Courtney, Yumei, and Qiuhong, for your friendship over the last five years; I don't think that I could have made it through the stress and continued frustrations of graduate school without any of you. And to Shuang for always being on the other side of the cubicle to listen and offer advice to the joys of life and frustrations of research; also for you willingness to always go and get ice cream. Shara, I have enjoyed all of our time together both in and outside of the lab; your love of singing, dancing and sense of humor made all of those countless hours of synthesis, imaging, and data analysis fly bye and less miserable. Your personality and love of learning and science is truly contagious, and I have enjoyed seeing you grow over the last four years and am lucky to call you a friend.

I would like to thank Janice (Malone) Raliff for first introducing me to chemistry in high school, without your initial fostering of my interest in chemistry, guidance, and encouragement to pursue chemistry, I would not be where I am today; I am forever indebted to you. To PJ for always fostering my inquisition, for teaching me to always think of others before myself, and for instilling the philosophy of "always taking more out then you go in with." You are the best teacher I have ever have, and all of the lessons that you taught me, I will forever carry with me.

Finally, I would like to thank those closest to me. To my best friend, Amanda, I could have not asked for a better friend than you. Thank you for all of the late nights of singing at the top of our lungs, watching the Princess Diaries, and determining the ideal properties of an electrode or man. Thank your for always believing in me. The last eight years would not have been the same without knowing you.

To my late Grandma Jared, for deciding that I didn't need help winning and that I could do it on my own, at such a young age. And for being such a positive role model, and teaching me that as long as I put my mind to it, I can achieve it. To my Grandma Anderson, thank you helping me learn to cook and fostering my creative side. Also, thank you for always having delicious cinnamon rolls whenever I come to visit, they are much appreciated. From both of my grandmothers, I learned to be patient and how to be a better teacher.

I would like to thank my in-laws, Susan, Bob, and Lisa Bagby, for so graciously accepting me into your family eleven and a half years ago, and for your continued support. I would like my brother Wesley for teaching me to stand up for myself and to be independent, although your ways were rather unconventional. I would not be the person I am today with out you. Of course, I would like to thank my parents for their love and guidance, and for teaching me to always strive for the best with anything I do. Thank you for always encouraging and supporting me to make my own decisions, whether it was to switch from playing the violin to flute to oboe, or my decision to change my major from chemical engineering to chemistry, no matter what I decided, you were always right there behind me. Also, thank you for being my biggest fans. Lastly, I would like to thank my husband for his unconditional love and support. Tom you have always encouraged me to follow my dreams. You are my best friend, always know when and how to make me laugh, or just listen; I would not have made it throughout the last five years without you by my side.

Table of Contents

Abstract iii

Dedication v

Acknowledgements vi

Table of Contents ix

Chapter 1. Introduction 1

- 1.1 Objectives and Thesis Overview 2
- 1.2 Introduction 3
- 1.3 Lymphatic System and it Role in Drug Delivery 3
  - 1.3.1 Physiology of the Lymphatic System 3
  - 1.3.2 Lymphatic Spread of Cancer 7
- 1.4 Lymphatic Imaging and Drug Delivery 9
  - 1.4.1 Requirements for Lymphatic Targeting 9
  - 1.4.2 Clinical Methods for Lymphatic Imaging 10
    - 1.4.2.1 Sentinel Lymph Node Biopsy (SLNB) 10
    - 1.4.2.2 Magnetic Resonance Imaging (MRI) 11
  - 1.4.3 Immerging Platforms for Lymphatic Imaging and Drug Delivery 12
    - 1.4.3.1 Liposomes 12
    - 1.4.3.2 Dendrimers 18
    - 1.4.3.3 Quantum Dots (QDs) 19
    - 1.4.3.4 Synthetic and Natural Polymers 20
- 1.5 Conclusions 23
- 1.6 References 25

Chapter 2. Development of Hyaluronan (HA)-Fluorescent Dye Conjugates and the Molecular Weight Optimization of for Intralymphatic Delivery Using *in vivo* Fluorescence Imaging 32

- 2.1 Introduction 33
- 2.2 Experimental 37
  - 2.2.1 Synthesis of HA-Texas Red using N-(3-Dimethylaminopropyl)-N'-ethylcarbodiimide hydrochloride (EDAC) 37
  - 2.2.2 Synthesis of HA-Texas Red using 2-chloro-1-methylpyridinium iodide (CMPI) 37
  - 2.2.3 Characterization of HA-Texas Red Conjugates 39

2.2.4 *In vivo* Imaging with HA-Texas Red 39
2.2.5 Synthesis of 5-carboxypentyl-amino-IR820 40
2.2.6 Synthesis of HA-IR820 Conjugates 40
2.2.7 Size Exclusion Chromatography (SEC) of HA-IR820 Conjugates 43
2.2.8 Fluorescence of HA-IR820 Conjugates 43
2.2.9 Zeta Potential of HA 43
2.2.10 *In vivo* Imaging of HA-IR820 Conjugates 44
2.2.11 *In vivo* Imaging Data Analysis of HA-IR820 Conjugates 44
2.3 Results 45
2.3.1 HA-Texas Characterization 45
2.3.2 *In vivo* Imaging with HA-Texas Red 46
2.3.3 HA-IR820 Characterization 48
2.3.4 Spectral Properties of HA-IR820 48
2.3.5 Zeta Potential of HA 50
2.3.6 Optimization of *In vivo* Lymphatic Imaging 51
2.3.7 *In vivo* Imaging Control Experiments 54
2.3.8 Molecular Weight Dependence on Lymphatic Uptake 56
2.4 Discussion 58
2.4.1 *In vivo* Imaging with HA-Texas Red 58
2.4.2 Characterization of HA 58
2.4.2.1 HA Polydispersities 58
2.4.2.2 Zeta Potential of HA 60
2.4.3 Characterization of HA-IR820 61
2.4.4 *In vivo* Fluorescence Imaging Optimization and Data Analysis 63
2.4.5 *In vivo* Imaging Control Experiments 64
2.4.6 Molecular Weight Dependence on Lymphatic Uptake 65
2.5 Conclusions 66
2.6 References 69

Chapter 3. Development and Optimization of Polyanionic Star Polymer-Fluorescent Dye Conjugates for Intralymphatic Delivery Using *in vivo* Fluorescence Imaging **74**
3.1 Introduction 75
3.2 Experimental 78
3.2.1 Star Polymer Synthesis 78
3.2.2 Star-IR820 Synthesis 81
3.2.3 Rheological Properties 84

3.2.4 Zeta Potential of the Star Polymers 84
3.2.5 *In vitro* Toxicity of the Star Polymers 85
3.2.6 *In vivo* Imaging of Star-IR820 86
3.2.7 *In vivo* Imaging Data Analysis 87
3.3 Results 88
3.3.1 Characterization of the Star Polymer and Star-IR820 Conjugates 88
3.3.2 Rheological Properties 89
3.3.3 Zeta Potential of the Star Polymers 91
3.3.4 *In vitro* Toxicity of the Star Polymers 93
3.3.5 *In vivo* Imaging of Star-IR820 94
3.4 Discussion 99
3.5 Conclusions 104
3.6 References 106

Chapter 4. Development of a Star Polymer-Geldanamycin (GA) Conjugate and the Intralymphatic Delivery of Star-GA for the Treatment of Three Orthotopic Tumor Models 109

4.1 Introduction 110
4.2 Experimental 114
4.2.1 Synthesis and Characterization of the Star-Geldanamycin Conjugate 114
4.2.2 *In vitro* Cytotoxicity 117
4.2.3 *In vitro* Release 118
4.2.4 B16F10 Murine Melanoma Tumor Model 118
4.2.4.1 B16F10 Tumor Model Optimization 118
4.2.4.2 *In vivo* Imaging with 74-kD HA-IR820 Conjugate in B16F10 Tumor Bearing Mice 119
4.2.4.3 Anticancer Efficacy in B16F10 Tumor Bearing Mice 120
4.2.5 4T1.2 Neu Murine Breast Cancer Tumor Model 121
4.2.5.1 Anticancer Efficacy Pilot Study in 4T1.2 Neu Tumor Bearing Mice 122
4.2.5.2 Increased Maximum Tolerable Dose (MTD) of Star-GA 122
4.2.5.3 Anticancer Efficacy in 4T1.2 Neu Tumor Bearing Mice 123
4.2.5.4 Metastatic Analysis of Axillary Lymph Nodes by Nodal Volume and Real Time Polymerase Chain Reaction (rtPCR) 123
4.2.6 A2058 Human Melanoma Tumor Model 124
4.3 Results 126

4.2.1 Synthesis and Characterization of the Star-Geldanamycin Conjugate 126
4.3.2 *In vitro* Cytotoxicity..128
4.3.3 *In vitro* Release 129
4.3.4 B16F10 Murine Melanoma Tumor Model 131
4.3.4.1 B16F10 Murine Melanoma Tumor Model Optimization 131
4.3.4.2 Effect of B16F10 Tumors on the *in vivo* Lymphatic Drainage of 74-kD HA-IR820 Using *in vivo* Fluorescence Imaging 133
4.3.4.3 *In vivo* Treatment Efficacy with Melphalan in the B16F10 Murine Melanoma Tumor Model 136
4.3.4.4 *In vivo* Treatment Efficacy with 17-DMAG and Star-GA in the B16F10 Murine Melanoma Tumor Model 137
4.3.5 4T1.2 Neu Murine Breast Cancer Tumor Model...139
4.3.5.1 *In vivo* Treatment Efficacy with 17-DMAG and Star-GA in the 4T1.2 Neu Murine Breast Cancer Tumor Model – Pilot Study.........139
4.3.5.2 Increased Maximum Tolerable Dose (MTD) of Star-GA.......................141
4.3.5.3 *In vivo* Treatment Efficacy with 17-DMAG and Star-GA in the 4T1.2 Neu Murine Breast Cancer Tumor Model..............................141
4.3.5.4 Metastatic Analysis of Axillary Lymph Nodes by Nodal Volume and Real Time Polymerase Chain Reaction (rtPCR)..............................142
4.3.6 A2058 Human Melanoma Tumor Model Optimization and Efficacy with 17-DMAG and Star-GA – Pilot Study..145
4.4 Discussion 147
4.4.1 *In vitro* Characterization 147
4.4.2 B16F10 Murine Melanoma Tumor Model 148
4.4.3 4T1.2 Neu Murine Breast Cancer Tumor Model...152
4.4.4 A2058 Human Melanoma Tumor Model 154
4.5 Conclusions 155
4.6 References 157

Chapter 5. Summary and Future Work 162
5.1 Summary 163
5.2 Future Work 166
5.2.1 Further Optimization of Lymphatic Carriers and Imaging Agents........................166
5.2.2 Future Optimization of the Star-GA Conjugates and Dosing Regimens................169
5.2 References 174

Appendix 1. Synthesis of 4-Arm-Acid-Star Polymers 175
A.1 Materials 176
A.2 Synthesis of Acid-Star Polymers 176
A.2.1 Synthesis of the Bromide Intermediate Compound 176
A.2.2 Synthesis of the MADIX Agent 177
A.2.3 Synthesis of the RAFT Agent, 1,2:3,4-di-O-isopropylidene-6-O-acryloyl-α-D-galactopyranose 178
A.2.4 Synthesis of the Protected Sugar-Star Polymer, poly-(1,2:3,4-di-O-isopropylidene-6-O-methacryloyl-α-D-galactopyranose) by MADIX/RAFT Polymerization 178
A.2.5 Deprotection Reaction to Form the Sugar-Star Polymer, the Multi-Arm poly-(6-O-methacryloyl-D-galactopyranose) 179
A.2.4 Modification of the Multi-Arm poly-(6-O-methacryloyl-D-galactopyranose) with Succinic Anhydride to Yield the Acid-Star Polymers 180
A.3 References 180

Chapter 1. Introduction

1.1 Objectives and Thesis Overview

The objectives of this work are to develop and optimize the size and charge of polymeric nano-carriers for localized lymphatic imaging and drug delivery, and to develop a intralymphatic chemotherapy using one of the optimized polymeric nano-carriers for the treatment of lymphatically metastatic cancers, such as melanoma and breast cancer. This work can be divided into three parts: 1) Development of hyaluronan (HA)-fluorescent dye conjugates and the molecular weight optimization of the HA-dye conjugates for intralymphatic delivery utilizing whole body fluorescent imaging; 2) Development of star polymer-fluorescent dye conjugates and the optimization of the degree of negative charge required for intralymphatic delivery utilizing whole body fluorescent imaging; and 3) Development of a star polymer-geldanamycin conjugate (Star-GA) for the intralymphatic delivery and determination of the *in vitro* and *in vivo* efficacy of Star-GA in melanoma and breast cancer.

The following chapter will provide a brief background on the physiology of the lymphatic system and how cancers metastasize, followed by examples of clinical and preclinical lymphatic imaging and drug delivery platforms that exploit the physiology of the lymphatics and the natural lymphatic progression of cancer allowing for the specific lymphatic targeting for medical diagnosis, imaging, and drug delivery. Both of which lay the foundation for purpose of this work of developing and optimizing two different lymphatic imaging and drug delivery carriers, and the evaluation of their use as a lymphatic drug delivery carrier for the treatment of melanoma and breast cancer.

1.2 Introduction

Many cancers, including melanoma, breast, colon, lung, and ovarian, spread or metastasize via the lymphatic system, a mono-directional network of vessels and nodes that parallels the circulatory system [1,2]. Accurate determination of the lymph nodes involved in the early lymphatic spread of the primary tumor is paramount for survival of the patient. In melanoma and breast cancer, the first metastatic site is usually the lymph node basin draining the primary tumor [3,4]. It is possible to specifically target the lymphatics utilizing the natural structure of the lymphatic capillaries, which have pores of approximately 100 nm in diameter, by tailoring the size of bimodal imaging and drug carriers to be 10 to 100 nm in diameter. By exploiting the physiology of the lymphatics along with the pathology of cancer spread, we can localize imaging agents and chemotherapeutics to the lymphatics, where the metastases reside. Localized lymphatic delivery of multimodal imaging and drug carriers will allow the accurate identification of the diseased nodes and along with treating the primary tumor and metastases. In addition, this approach will minimize toxicities associated with systemic administration of cytotoxic chemotherapeutics and maximize the localized dose to the affected tissues, with the potential to significantly increase the treatment efficacy.

1.3 Lymphatic System and its Role in Drug Delivery

1.3.1 Physiology of the Lymphatic System

The lymphatic system is a unidirectional network of capillaries, vessels, and nodes that parallel the systemic circulation. Lymphatics are found virtually everywhere in the body where blood vessels are present, with the exception of the central nervous system. The propulsion of the lymph is mainly driven by muscle contractions and relaxations, although increased muscular activity will increase the interstitial pressure resulting in an increase in the lymph flow. The presence of one-way valves throughout the lymphatic vessels prevents backflow and assists in the lymph propulsion. The primary function of the lymphatic system is to maintain fluid balance and absorption of plasma proteins and cellular waste materials from the extracellular space and returning them to the systemic circulation [5-8].

The interstitium is the space between the capillary walls and the cells in the tissue. Its structure is similar to that of tissue, in that it is a fibrous network of collagen and reticular fibers embedded in a gel-like ground substance. The fibrous network provides physical support for the interstitium. The ground substance is composed of glycosaminoglycans (GAGs), salts, and plasma proteins [5,9]. The GAGs are polyanionic, unbranched, polysaccharides consisting of disaccharide units of an amino sugar and an uronic acid [9,10]. With the exception of hyaluronan (HA), the GAGs are covalently bound to a protein and are referred to as proteoglycans. However, the major GAG in the skin is HA, which accounts for approximately two thirds of the total GAG content [9]. Further, about one half of the total HA in the body is found in the dermis and epidermis [9,11]. The GAGs are ionized at physiological pH resulting in a net negative charge of the ground substance. Within the interstitium, there are areas of aggregated and disaggregated polysaccharides forming narrow aqueous channels with diameters of 100 nm [5].

The interstitial fluid that drains from the interstitium through the lymphatics is referred to as lymph. The lymph and plasma components are essentially the same, but are present at different concentrations, which may vary based on their location. Some of the major components in both the plasma and lymph are: proteins, enzymes, lipids, and electrolytes. The proteins found in the plasma are also in the lymph, but at a lower concentration; for example, the protein concentration in the thoracic duct lymph is approximately 60% of that found in the serum. Similarly, most of the enzymes found in the plasma are also present in the lymph. However, in the tissues that produce the enzymes, their concentrations are higher in the lymph than in the plasma, suggesting that the primary route of these enzymes entering the plasma is through the lymphatics. The lipid concentration in the lymph is also lower than that of the plasma, with the exception of the intestinal lymph. Finally, the concentration of the electrolytes is similar in both the lymph and plasma, however, the cation (Na^+, Ca^{2+}, K^+, and Mg^{2+}) concentration is slightly lower, and the anion (Cl^- and HCO_3^-) concentration is slightly higher in the lymph than the plasma [5,7].

The physiology and size of the lymphatic capillaries and vessels vary along the course of the lymphatic network. The initial or terminal lymphatic capillaries are the smallest in nature (10 to 60 μm), but unlike blood capillaries, lymphatic capillaries consist of a single layer of non-fenestrated endothelial cells and lack a continuous basal lamina [5-7]. Anchoring filaments between the outer portion of the plasma membrane of the endothelial cells and the interstitium, provide the structural support of the capillaries. Along the initial lymphatics, there is a considerable amount of overlap of the endothelial cells and gaps within the intercellular junctions, leading to the formation of clefts and pores along the capillary wall. When the interstitial pressure exceeds the intraluminal lymphatic pressure, these clefts and pores are "opened" allowing for the passage of macromolecules into the lymphatic capillaries [5-7]. This is an important property of the lymphatic capillaries that leads to the ability to natural "recycling" of extracellular proteins, fluids, and lipids, to the systemic circulation via the lymphatics.

The initial lymphatics merge into the collecting lymphatics, which drain to the lymph nodes. The collecting lymphatic capillaries are larger in size (0.5 to 0.75 mm in diameter) [6,8], also the emergence of thicker walls and valves distinguish the collecting lymphatics from their predecessors. This increase in wall thickness is due to the appearance of a connective tissue and smooth muscle, and they eventually progress to having a trilaminar structure, resembling more that of blood vessels. In addition to fewer open junctions, the basal lamina is continuous. Because lymphatic system lacks a "pump", the presence of the smooth muscle allows for vessel contractions to help propel the lymph. Additionally, to prevent back-flow, there are valves, usually unicuspid or bicuspid in nature, at regular intervals along the lymphatic vessels [5-7].

The afferent lymphatic vessels are the collecting lymphatics from the peripheral tissue that drain into the lymph nodes through the subcapsular sinus of the node. The efferent lymphatic vessels, vessels from the lymph nodes, upon exiting from the hilum of the node merge to form post-nodal vessels, which either lead to the successive lymph nodes or larger lymphatic vessels. These vessels have a similar structure to that of the collecting lymphatics, but are equipped with thicker walls, larger lumina, and tricuspid valves. These larger lymphatic vessels combine with the lymphatic trunks, which eventually drain into the thoracic duct and the right lymphatic ducts that return the lymph to the systemic circulation through the internal jugular and right subclavian veins, respectively [5,7].

The lymph nodes are kidney bean shaped dense masses of tissues located throughout the lymphatic system, they are highly compartmentalized and are usually found in principal groups near the blood vessels for which there are named. In the average adult, there are anywhere from 500 to 1000 lymph nodes of 1 mm to 1 cm in diameter [7]. The two main functions of the lymph nodes are: 1) to serve as a filter for the lymph, and 2) carry out immunological functions [5,7].

The lymph enters the node through the afferent lymphatics into the subcapsular sinus, progressing through the cortical and then the medullary sinuses, finally exiting the node through the hilum to the efferent lymphatics [5,7]. The sinuses are lined with fixed or stationary macrophages along with having mobile macrophages that can act as both antigen presenting cells and as a filter for the removal of antigens and non- antigenic particulates [5].

1.3.2 Lymphatic Spread of Cancer

Cancer cells can metastasize via the lymphatics, circulatory system, or by invading local tissues; however, many cancers, including melanoma and breast cancer, metastasize preferentially via the lymphatics [2-4]. As early as the late nineteenth century, Halstead theorized that breast cancer is a localized disease that metastasizes through the lymphatics to the regional lymph nodes (RLN). Today it is well-established that cancers can progress lymphatically without systemic involvement [1]. The process of lymphatic metastasis follows a stepwise progression from the primary tumor to the regional lymph nodes through the intervening lymphatic vessels. Once metastases are established in the sentinel lymph node (SLN), the further metastatic progression can continue through the draining lymphatics and eventually enter the systemic circulation to form distant metastases. However, direct hematological metastasis can proceed without SLN involvement; though, we are primarily interested in the lymphatic route of metastasis and treatment.

The general metastatic pathway via the lymphatics is thought to be similar in all vertebrates. Once the primary tumor growth reaches a critical mass [4], it secretes lymphangiogenic cytokines to induce the formation of new lymphatic capillaries, also known as lymphangiogenesis [1]. Invading tumor cells can then enter the extracellular matrix (ECM), where they can then enter the new lymphatic vessels with the lymph due to the increase in interstitial pressure. Further, as the tumor grows, the intratumoral interstitial fluid pressure increases, resulting in an increase in the interstitial fluid volume, thus causing the anchoring filaments to widen the lymphatic lumen and open the intercellular junctions; allowing for uptake of fluid and cells into the lymphatics [1]. Although many cancers are reported to have non-functional intratumoral lymphatics, functional lymphatics have been identified within the tumor margin (<100 μm from the tumor edge) [2,12,13]. Once the cancer cells enter the lumen of the lymphatic capillaries, single cell or clustered embolisms, "in-transit" metastases, are formed in the draining lymphatics to the RLNs. The surviving "in-transit" metastases can either adhere to the lymphatic endothelium, proliferate, and invade the surrounding tissue, or enter the afferent lymphatics of the SLN. Once the "in-transit" metastasis has entered the SLN, the cells can invade the LN cortex forming a lymph node metastasis or continue through the lymphatics to the subsequent LNs [1].

In both breast cancer and melanoma, the first site of metastasis is usually the regional lymph node basin [3,4]. Further, lymphatic vessel growth within the tumor has been shown to have a positive correlation with the metastatic spread of melanoma, breast and head and neck cancers [14]. The use of sentinel lymph node biopsies, discussed in the next section, has been used for the clinical staging of melanoma and breast cancer since the early 1990s [15]. Where the lymph nodes that test positive for micrometastases by pathology are identified and removed, potentially saving the patient from a complete lymphadenectomy of unaffected nodes or a radical mastectomy. In spite of this, nanometastases are often overlooked leading to relapse.

1.4 Lymphatic Imaging and Drug Delivery

Imaging of the lymphatics plays a role in disease discovery and diagnosis, as many cancers metastasize via the lymphatic system, including: melanoma, breast, colon, lung, and ovarian cancers [1,2]; accurate determination of the lymph nodes involved in the early lymphatic spread of the primary tumor is paramount for survival of the patient. In melanoma for example, the five year survival rates are >90%, 40-60%, and 15-20%, if the primary tumor is small (<1-2 mm thick) and completely localized, has spread locally only around the primary tumor with 1-3 local lymph node involvement, or any distant spread including distant lymph nodes and organs, respectively [16].

1.4.1 Requirements for Lymphatic Targeting

Uptake of particulates into the lymphatic capillaries after subcutaneous administration is dependent on several factors, including: size, charge, and hydrophobicity; however, size is the predominantly governing factor in the absence of macrophage interactions [17,18]. Due to the natural structure of the clefts and pores along the lymphatic capillaries and the presence of aqueous channels (100 nm in diameter) within the interstitium [19], particles with sizes of 10 to 100 nm are preferentially taken up by the lymphatics [18,20]. Whereas particles >100 nm largely remain at the injection site as a depot, and particles <10 nm are reabsorbed by the blood capillaries. Though it is generally recognized that the pores in the blood capillaries in the skin are ca. 5 nm in diameter and non-fenestrated, it was found that the capillaries of rodent footpads are fenestrated with pores of 6 to 12 nm [21-23], thus the use of the 10 nm cutoff rather than 5 nm for lymphatic targeting.

It has been reported that negatively charged particles are more readily taken up by the lymphatics compared to neutrally to positively charged particles [24-26]. In part due to the electrostatic repulsions between the negatively charged particle and the extracellular matrix [18] that is primarily negatively charged [5,17,18]. Also, negatively charged particles have been shown to have longer lymph node retention due to the activation of macrophages [18]. However, little research has been conducted into the extent of negative charge needed for optimal lymphatic uptake. Further, hydrophilic particles have increased lymphatic uptake and decreased nodal retention compared to hydrophobic particles [18,27].

1.4.2 Clinical Methods for Lymphatic Imaging

Conventional imaging for the diagnosis of lymphadenopathy and lymph node metastases rely on the identification of enlarged lymph nodes using computed tomography (CT) and magnetic resonance imaging (MRI). These methods are susceptible to errors in that they rely on the identification of enlarged lymph nodes, which may be due to metastases, infection, or an autoimmune disease, leading to false-positives. Further, these techniques are not very sensitive in that the lymph nodes have to be significantly enlarged for identification; for CT a lymph node with a short axis diameter of ≥1cm is considered to have metastases. These techniques are not able to identify the SLN or micro-metastases, mainly found with breast cancer, where these nodes are usually “normal” in size and shape [28,29].

1.4.2.1 Sentinel Lymph Node Biopsy (SLNB)

The clinical method for determining the SLN, the first draining lymph node, has not changed significantly since its first use in the 1960s. Currently, sentinel lymph node biopsies are used for the clinical staging of melanoma and breast cancer [15,30-33]. The SLN mapping consists of an injection proximal to the primary tumor of a blue dye (isosulfan blue, patent blue, or methylene blue) or ^{99m}Tc-sulfur colloid, used singly, or in combination, is performed prior to the sentinel lymph node biopsy (SLNB). Both the dye and colloid drain to the regional lymphatic vessels, sentinel lymph node, and regional nodes, which is observed visually (dyes) or with a gamma camera (^{99m}Tc colloids). Both methods have their own disadvantages; including, rapid dispersion and lack of localization to only the SLN (dye), risk of anaphylaxis (dye), propensity for long term staining of skin (dye), low resolution (^{99m}Tc), and radiative isotopes (^{99m}Tc) [15,29,34]. Further, the two injections do not occur simultaneously, thus causing the differing distribution and clearance kinetics of the two substances. In order to overcome this issue and simplify the presurgical injection procedure, the kit was developed by combining the isosulfan blue dye with the ^{99m}Tc labeled liposomes.

In 2002, Plut et al. developed a formulation kit by chemically combining a pyrogen-free low molecular weight isosulfan blue dye solution and ^{99m}Tc labeled liposomes, producing a radioactive blue liposomal formulation for pre-surgical injections [35]. This formulation avoids the non-synchronized distribution and clearance kinetics of the small molecular weight dye and the radioactive liposomes when they are administered separately. Because of the importance in SLN staging and the disadvantages in the current clinical methods, there is a great need for new imaging and targeted drug delivery vehicles to the lymphatics.

1.4.2.2 Magnetic Resonance Imaging (MRI)

Magnetic resonance imaging (MRI) could become another useful tool for imaging the lymphatic system. MRI can overcome the poor resolution of ^{99m}Tc, but lymphcentric contrast agents are required to provide clinically useful imaging of the lymphatic system. Fujimoto et al. developed gadolinium-diethylenetriamine pentaacetic acid (Gd-DTPA) labeled liposomes using long-circulating palmityl-D-glucuronide liposomes [36]. After a subcutaneous injection of the liposomal formulation into the hind feet of rabbits, the popliteal lymph nodes as well as the deep retroperitoneal lymph node were detected. The enhanced lymphatic liposomal accumulation was likely due to the trapping of liposomes by the macrophages [36-38]. Rapid clearance post injection is the major drawback of liposomal formulations; therefore, a liposomal drug delivery system with prolonged retention is of high interest to physicians. More recently, the Kobayashi group at the NCI has investigated dendrimer-Gd conjugates for lymphatic imaging, discussed further in the dendrimer section [39-41].

1.4.3 Immerging Platforms for Lymphatic Imaging and Drug Delivery

1.4.3.1 Liposomes

Liposomes have probably been the most widely studied platform for the use in lymphatic delivery, and most of the early work developing optimized lymphatic carriers used liposomes [25,42-45]. In a study of negatively, neutrally, and positively charged ^{99m}Tc and ^{125}I labeled poly(vinyl pyrrolidone) liposomes, Patel et al. determined that negatively charged liposomes are localized in the lymph nodes more than positively and neutrally charged liposomes after s.c. administration in the rat footpads [25]. Further, using liposomes, it was found that the size cutoff for lymphatic uptake is approximately 100 nm for neutral liposomes [46].

Liposomal formulations can encapsulate anti-cancer drugs for intravenous infusion for the treatment of various types of cancers. The primary advantages of systemic liposomal chemotherapy encompass reduced side effects compared to the standard i.v. therapy, and inhibit the anti-cancer drug from enzymatic digestion in the systemic circulation. Early i.v. liposomal delivery formulations had short circulatory half-life due to the rapid clearance by the reticuloendothelial system (RES). In addition, these formulations were unstable in the plasma and gastrointestinal tract resulting in lipid degradation and drug leakage [47]. PEGylation of liposomes is one method for prolonging the systemic retention and decreasing the volume of distribution and clearance [48] by protecting the liposomes from opsonization and subsequent macrophage uptake by Kupffer cells in the liver [49]. The increased systemic circulation allows for an increase in liposomal tumor accumulation through the enhanced permeability and retention (EPR) effect [48]. As the lymphatic system is difficult to target via the intravenous route, due to the separation from systemic vasculature and the unidirectional flow [50], local parenteral administration, such as subcutaneous, intraperitoneal (for intestinal delivery), and intramuscular injections, is more extensively investigated for lymphatic delivery via liposomal carriers. Another characteristic of pegylated liposomes is that their size can be adjusted through the modification of the PEG chains or lipid bilayer core of the carrier, promoting its potential use as a drug delivery vehicle to the lymphatics after subcutaneous injection [51].

Doxil™, a pegylated liposomal doxorubicin chemotherapy formulation, is widely used as first-line therapy of AIDS-related Kaposi's sarcoma, breast cancer, ovarian cancer, and other solid tumors [48,52-55]. Intravenous liposomal doxorubicin (i.e. Doxil™) has substantially improved pharmacokinetics of the drug compared to standard i.v. doxorubicin therapy, including increased AUC and half life. Multiple clinical trials with i.v. Doxil™ alone or in combination with other chemotherapeutics, such as paclitaxel and other taxanes, cyclophophamide, docetaxel, and gemcitabine, have been conducted since the mid-1990s [56] for various different cancers. In a randomized Phase III clinical trial of patients with stage IIIB or IV metastatic breast cancer, 509 women with normal cardiac function were treated with either pegylated liposomal doxorubicin HCl (PLD) (50 mg/m^2, every 4 weeks) or i.v. doxorubicin (DOX) (60 mg/m^2, every three weeks) [57]. Although the PLD formulation exhibited a significant reduction in the cardiotoxicity (DOX to PLD hazard ratio = 3.16, $p<0.001$), myelosuppression, vomiting, and alopecia, it did not exhibit increased efficacy compared to conventional i.v. DOX (21 vs. 22 month mean survival, 23% response rate). In addition, the PLD formulation increased the incidence of palmar-plantar erythrodysesthesia (PPE, hand-foot syndrome) (48% vs. 2%), stomatitis (22% vs. 15%), and mucositis (23% vs. 13%) compared to i.v. DOX [57].

Keller et al. conducted a randomized Phase III trial with 301 women with taxane-refractory advanced breast cancer [58]. Following previous failure with first- or second-line treatment regimens with taxanes, patients were treated with PLD (50 mg/m^2, every 28 days, n=150), vinorelbine (5 mg/m^2, weekly, n=129) or mitomycin C (10 mg/m^2, day 1 and every 28 days) plus vinblastine (5 mg/m^2, days 1, 14, 28, and 42) (n=22), as a comparison for salvage regimens. In patients with taxane-refractory breast cancer, treatment with vinorelbine or the combination of mitomycin C and vinblastine are common salvage treatment regimens (comparator). Patients receiving PLD exhibited comparable progression free survival (PFS) and overall survival (OS) efficacy compared to the comparator [2.9 vs. 2.5 months (PFS) and 11.0 and 9.0 months (OS), for the PLD and comparator, respectively]. PLD was hematologically safer than the comparator, with a grade 3 to 4 decrease in the leukocytes of 20% for PLD, 54% for vinorelbine, and 30% for mitomycin C – vinblastine. The commonly reported adverse effects of nausea, vomiting, and fatigue, were comparable amongst all of the treatment groups. However, PPE was the most common reported treatment related adverse event with 37% of patients experiencing grade 3 and one patient experiencing grade 4. Further PLD treatment increased the incidence of stomatisis from 4% to 22%, for treatment with vinorelbine compared to PLD, respectively.

Although i.v. Doxil™ reduces cardiotoxicity compared to conventional i.v. DOX, along with improved pharmacokinetics, it does not exhibit an increase in efficacy over conventional treatment in the aforementioned clinical trials. However, Doxil™ liposomes are approximately 90 nm in size [59], thus they could be potentially be delivered lymphatically and have increased efficacy compared to i.v. administration. Ling et al. compared subcutaneous administration of liposomal doxorubicin with the standard intravenous doxorubicin treatment in a rabbit breast cancer model [60]. Female New Zealand rabbits were inoculated with VX2 carcinomas and treated three times with 1-mg/kg (doxorubicin equivalent) of subcutaneous liposomal doxorubicin, intravenous adriamycin, or saline, once the axillary lymph nodes reached 5 mm in diameter. Two days after the completion of the treatment, the nodal volume was measured and compared between different treatment groups. Data revealed that the liposomal doxorubicin treatment and intravenous doxorubicin decreased the nodal volume by 57% and 27%, respectively, and increased the number of apoptotic cells by 3.2- and 2.0-fold, respectively, compared to the saline control. The subcutaneous administration of doxorubicin demonstrated a more robust inhibitory effect relative to systemic doxorubicin, with a p value equal to 0.002 between the two treatment groups. Site inflammation including allergy and skin ulceration was not observed, likely due to the low dose of the drug administered, as well as the relatively short treatment period. In summary, the liposomal doxorubicin treatment exhibited effective inhibition of tumor progression and induction of apoptosis of metastatic cells, which may be a promising method for the treatment of node-positive advanced breast cancer.

Harrington et al. reported improved delivery of anticancer drugs to tumors using

PEGylated liposomes as vehicles for intratumoral and subcutaneous injection [51]. The authors compared the pharmacokinetics and tissue distribution, of subcutaneously or intratumorally injected pegylated liposome-encapsulated ^{111}In-labeled diethylenetriaminepentaacetic acid (IDLPL) with the unencapsulated IDLPL. The encapsulated form increased the carrier residence time and concentration in the head and neck tumors and their nodal metastases (both inguinal and axillary lymph nodes) in a nude mouse xenograft model, yielding a 11.6-fold increase in the area-under-the-curve (AUC) (96 h). Although the addition of PEG to liposomes increases the systemic retention after i.v. administration in comparison to uncoated liposomes or the free drug, for subcutaneous administration, the addition of PEG to liposomes only slightly increases the lymphatic absorption and retention compared to non-PEG coated liposomes [61].

Melphalan is a nitrogen mustard alkylating agent with high systemic toxicity but extremely poor stability at physiological conditions (half-life < 1 h) owing to its rapid hydrolysis resulting in the inactive form of the drug. Melphalan was encapsulated into liposomes made of egg phosphatidylcholine (PC) and cholesterol with average entrapment efficiency of 8.1% [62]. The release study in PBS at 37°C indicated the rapid release of melphalan during the first 4 h (> 70%) and only 20% remained after 24 h. After subcutaneous injection of free melphalan into left leg of rats, different melphalan concentrations were seen between ipsilateral and contralateral nodes at 0.5 h, but no differences were observed at subsequent time points. In the liposomal melphalan group, the liposome concentration in the ipsilateral lymph nodes was 200- and 100-fold higher than that in the plasma and contralateral nodes, respectively. The encapsulated melphalan demonstrated a sustained release from the liposome *in vivo*. At 24 h post dose, the melphalan level in the ipsilateral nodes was 20- and 10-fold greater than in the plasma and the contralateral nodes, respectively. In the tumor-bearing rats (mammary adenocarcinoma 13762), melphalan-encapsulated liposomes were more efficient in reduction of lymph node metastasis weight than for the same dose of free melphalan (0.125 mg/kg). An equivalent effect on the reduction of lymph node metastases was achieved comparing 0.125 mg/kg liposome-melphalan and 1 mg/kg free melphalan. The role of the liposomal size in lymphatic uptake was investigated in a separate study [63]. Both large and small melphalan-encapsulated liposomes were prepared by sonication, with sizes of upto 250 nm or 34.3 ± 7.8 nm, respectively. When melphalan encapsulated liposomes were given by subcutaneous injection into the left thigh of rats, the melphalan level in the ipsilateral lymph nodes was increased such that 24 h post dosing, the melphalan levels reached a 10-fold higher concentration for small liposomes compared to large liposomes, where the larger liposomes remained primarily at the injection site. The melphalan concentration in the plasma was relatively low for both small and large liposome groups.

A major issue of conventional liposomal formulations is that liposomes are poorly retained in the draining lymph nodes following injection (<2% injected dose). In order to enhance the retention of liposomes to lymph nodes, Phillips et al. developed an avidin activated biotin-coated liposome, resulting in prolonged lymphatic retention and extended lymph node localization, in an experimental rabbit model [64]. Biotin-coated liposomes were injected subcutaneously into both hind feet of rabbits, followed by an adjacent subcutaneous injection of avidin, causing the formation of liposomal aggregates in the lymphatic vessels. Twenty-four hours post injection, the retention of the liposomes was increased by 7.1- and 6.7-fold in the popliteal and iliac nodes, respectively.

1.4.3.2 Dendrimers

Kobayashi *et al.* reported successful detection of lymphatic drainage of breast cancer in normal mice and spontaneous (BALB-neuT mice) and xenografted (PT-18) breast tumor models after a direct mammary gland or peritumoral injection of the generation-6 polyamidoamine dendrimer Gd contrast agent [41]. In a following study, Gd-labeled dendrimer-based contrast agents (1 to 12 nm in diameter) were compared in terms of the efficiency of delivery of the agents to the sentinel lymph nodes [40]. The generation 6 polyamidoamine (PAMAM-G6) Gd-dendrimer agent (ca. 9 nm) illustrated the axillary lymph nodes and lymphatic vessels more clearly in non-tumor-bearing mice than the other agents including PAMAM-G2, G4, G8 and generation 5 polypropylenimine dendrimer Gd agents. The peak concentration of the PAMAM-G6 agent (> 400 ppm) was achieved at 24 – 36 min post injection with high signal-to-background ratio (> 100). Although no significant differences were found between micrometastatic or non-metastatic lymph nodes for the accumulation of Gd in the axillary lymph nodes, the PAMAM-G6 Gd dendrimer showed the potential for targeted delivery to the lymph nodes.

Dendrimers are appealing for lymphatic imaging and drug delivery due to their low polydispersities, compact size (nm in size), multi-valent surface groups, and high water solubility [65-68]. However, issues with their clearance, toxicity, and biodegradability have limited their use as therapeutic or imaging agents. Two commercially available dendrimers are polyamidoamine (PAMAM) and polypropylenimine diaminobutane (DAB), where PAMAM is the most commonly used dendrimer in part due to its increased solubility, owing to its polyamido backbone, and decreased immunogenicity [69]. Both PAMAM and DAB dendrimers are highly cationic with terminal amino groups, but these groups can be derivatized to give neutral or negatively charged surface chemistries that are more optimal for lymphatic uptake and reduced toxicity [70,71]. In addition, PAMAMs are not biodegradable, thus the sizes for in vivo use are limited to less than 5 to 6 nm for renal clearance, corresponding to a G6 PAMAM dendrimer [39,72]. Particles less than 10 nm no longer have specific lymphatic uptake, as they can also be absorbed by the blood capillaries, which have pores up to 12 nm in size depending on their location [23,73,74]. Further, dendrimer based-imaging agents optimized for lymphatic uptake and renal clearance (i.e. small and negatively charged), easily migrate through the lymphatics with little to no nodal retention, thus limiting their use as a localized sustained release drug delivery platform. Because of the toxicity issues, very little investigation into their use as a lymphatic drug delivery carrier has been conducted. Although biodegradable dendrimers have been developed using polyether imine, phosphates, melamine, amino acids as their building blocks to list a few, they are unlikely to exhibit significant accumulation, however, they have been shown to induce hemolysis (polyether imine), echinocytosis (phosphate), in vivo liver necrosis (melamine), and toxic degradation products (amino acids) [69,75].

1.4.3.3 Quantum Dots (QDs)

Quantum dots have only been recently investigated in the last decade for in vivo imaging, since their discovery in the late 1980s [76]. Quantum dots are semiconductor nanoparticles that exhibit extremely bright fluorescence, have tunable emission spectra, high quantum yields, excellent photostability, and are typically 5 to 20 nm in size [77,78]. There has been a growing interest in their use for lymphatic imaging due to their enhanced penetration depth, improved photostability, and broad absorption bands coupled with narrow emission spectra. However, there is considerable toxicity concerns surrounding the heavy metals (e.g. Cd, Te, and Se) used in the construction of the QD cores. Further, the surface of QDs must be functionalized due to their innate water insolubility and hydrophobicity for their use in vivo [79]. The size and charge of the QD dictate their clearance mechanism and residence time in vivo. For effective renal clearance, nanoparticles (NP) must be small, especially when vehicle toxicity is of concern, to minimize tissue exposure; the size cut-off for renal clearance of QDs is <6 nm [80,81]. Larger and negatively to neutrally charged (PEG coated) QDs have shown significant liver and spleen retention, from 1 to 6 months [77,78]. Even though, QDs can be conjugated to therapeutic drugs for theranostic applications, with the correct size and emission in the NIR range; toxicity is the greatest concern, therefore biodegradable polymeric carriers utilizing NIR dyes for imaging are of great interest to many researchers, including our laboratory, for lymphatic imaging and drug delivery.

1.4.3.4 Synthetic and Natural Polymer Platforms

Surface properties, including surface charge and hydrophobicity, of nano-/microparticles are one of the chief determinants of lymphatic uptake and biodistribution *in vivo*. Hawley *et al.* investigated the relationship between surface properties of nanoparticles and *in vivo* biodistribution [82]. Poly(lactide)-poly(ethylene glycol) (PLA:PEG) copolymers with PEG lengths of 750, 2,000 and 5,000 Da were used as a surface coating of PS and poly(DL-lactide-co-glycolide 75:25) (PLGA) nanoparticles. The PLGA–PLA:PEG nanoparticles were prepared by an oil-in-water emulsion of PLGA and PLA:PEG. All of the nanoparticles were sub-100 nm in size and negatively charged on their surfaces, with the PEG portion forming steric barriers. ^{125}I radiolabeled, uncoated PS or PLGA nanospheres were retained in the injection site ≤ 24 h after subcutaneous administration in rats. The lymphatic uptake of the nanoparticles was strongly dependent on the surface characteristics. Polystyrene or PLGA nanospheres coated with PLA:PEG (molar ratio 1.5:0.75, PEG length 750 Da) had the most lymph node uptake, ca. 15 to 20%, owing to a suitable hydrophilicity on the surface, which provided an adequate steric barrier to promote drainage from the injection site, while remaining hydrophobic enough to be recognized by the lymph node macrophages. Less than 3% of naked PLGA nanoparticles injected were retained in the lymph nodes, whereas the lymphatics retained 17 and 16% of the nanoparticles prepared by co-precipitation of PLGA and PLA:PEG (1.5:0.75) with 75 and 65% PLGA content, respectively. The uptake into the lymph nodes decreased with further increase (> 65%) of PLA:PEG content, possibly owing to the surface being too hydrophilic. The incorporation of hydrophilic PEG onto PS and PLGA nanoparticles improved their lymphatic drainage, but the rate of lymph node uptake was closely related to the length of the PEG chain and eventually the hydrophilicity of the nanoparticles.

Rao et al. studied the effect of size, charge, and hydrophobicity of polymeric nanoparticles on the lymphatic uptake after s.c. administration in rats [18]. The effect of size and hydrophobicity were studied in parallel studies using PLGA-PMA:PLA-PEG (75:25) (PP) [poly(D,L-lactic-co-glycolic) labeled with 1-pyrenemethylamine (PLGA-PMA): polylactic acid-co-polyethylene glycol (PLA-PEG)] and polystyrene (PS) nanoparticles of ca. 50, 100, and 200 nm in size. With both the PP and PS nanoparticles, the cumulative nodal uptake decreased with increasing nanoparticle size. The hydrophilic PP nanoparticles had significantly increased nodal accumulation (10 to 30-fold increase) compared to the PS nanoparticles of similar size ($p<0.05$) for all three sizes studied. For studying the effect of the degree of negative charge on the lymphatic uptake, the ratio of poly(D,L-lactic-co-glycolic) acid with a terminal carboxylic acid group (PLGA-COOH) to 1-pyrenemethylamine labeled PLGA (PLGA-PMA, 1:1) polymers was varied to give a series of different PLGA-PMA:PLGA-COOH nanoparticles with increasing degrees of negative charge. As the amount of PLGA-COOH was increased from 20% to 80%, thus decreasing the zeta potential from -44.6 ± 11.3 to -57.1 ± 11.1 mV, the cumulative lymphatic uptake was increased by 10-fold. The authors demonstrated that for polymeric nanoparticles, 50 nm hydrophilic particles had the greatest lymph node accumulation and the lymphatic uptake increases with increased negative charge.

Natural polymers, for example, dextran and HA, have been studied for their potential use as carriers for lymphatic drug delivery for cancer. Mitomycin C (MMC) was conjugated to dextran (average MW of 10, 70 and 500 K), and distribution of the mitomycin–dextran (MMC–D) conjugate was compared to free MMC after injection into the left thigh muscle of rats [83]. The MMC–D conjugate slowly cleared from the injection site with a significant amount remaining in the muscle after 48 h (3.4, 13.2, and 21.8 %, for the 10, 70 and 500 kD dextran, respectively), whereas only 0.56% of the free MMC remained at the injection site after 30 min. The free MMC reached a peak regional lymph node concentration of 11.8 μg/g after 5 min, but no drug was detectable after 30 min. MMC-D (T-70K and T-500K) showed a higher and sustained accumulation in the regional lymph nodes even ≤ 48 h post dose. In rats inoculated with L1210 leukemia cells in the left thigh, no significant tumor suppression was observed in the lymph node metastases with free MMC or MMC-D (T-10K) groups owing to low MMC uptake by the nodes. In contrast, the T-70K and T-500K MMC-D (2.5 mg/kg dose) reduced the weight of the left iliac node, indicating the suppression of tumor growth and metastasis via lymphatic system. In subsequent studies, when comparing the drainage of cationic, neutral, and anionic dextran-MMC conjugates, the authors found that negatively charged dextran conjugates were more readily taken up by the lymphatics compared to neutrally to positively charged dextran conjugates [24,26]. In conclusion, anionic dextran-MMC conjugates may be useful for preventing lymphatic metastasis of cancer.

Hyaluronic acid is a natural polysaccharide of D-glucuronic acid and D-*N*-acetylglucosamine found in the interstitial space of tissues and in the synovial fluid of joints. Cisplatin was incorporated with HA by anionic polymer–metal complexation between the HA and cisplatin [84]. The nanoparticles were ca. 100 to 200 nm in size, with cisplatin loading from 3.9 to 11.8% (wt/wt). The cisplatin release kinetics demonstrated that the cisplatin–HA conjugate had an initial burst release in the first 12 h followed by a sustained release for 4 days. The cisplatin release rate was enhanced by the addition of hyaluronidases (HAses), the enzyme that degrades HA. Cai et al. reported an *in vivo* study of cisplatin–HA nanoparticles (25% wt/wt cisplatin), where the cisplatin–HA conjugates showed similar anti-tumor activity and were well tolerated in rodents compared to intravenous cisplatin [85]. The AUC of cisplatin in the axial lymph nodes after subcutaneous injection of cisplatin-HA increased 74% compared to free cisplatin. Therefore, the cisplatin–HA nanoparticles are suitable drug delivery vehicles for platinum chemotherapy in the lymphatics.

1.5 Conclusions

New non-invasive methods for the accurate determination of the SLN and the metastatic nodes are crucial for the improved survival and quality of life for those with lymphatically metastatic cancers. Developing new platforms that can both image and treat the diseased nodes would serve as a stepping-stone for improved treatment outcomes and reduced toxicities in the lives of those affected by cancer. Great strides have been made in the SLNB procedures for the staging of melanoma and breast cancer, providing patients with more treatment options, minimizing drastic surgery, reducing relapse, and providing hope. However, as with any medical procedure, further optimization and development are needed, which has led to the investigations into multiple new imaging agents and carriers for lymphatic imaging and drug delivery. With the advantages of particle engineering and a better understanding of the lymphatic anatomy and the drug transporting mechanism by the lymphatic system, lymphatic delivery via polymeric nano-/micro-particles may improve the efficacy of current cytotoxic chemotherapeutics. However, many of the newly developed agents and carriers have substantial toxicities associated with them, thus limiting their use to preclinical research rather than translational research into the clinic. Promising results in the area of liposomes have been made, especially with the Doxil^{TM} formulation, however, the limited nodal retention after s.c. administration still remains a hurdle to developing a localized sustained release formulation. Our efforts have focused on the development of biodegradable carriers, including hyaluronan and star polymers, for the use in lymphatic imaging and drug delivery utilizing NIR dyes and chemotherapeutics, such as cisplatin, doxorubicin, and geldanamycin for the treatment of lymphatically metastatic cancers.

1.6 References

1. Nathanson, S.D., Insights into the mechanisms of lymph node metastasis. *Cancer* **2003**, *98*, 413-423.

2. Eccles, S.A.; Welch, D.R., Metastasis: Recent discoveries and novel treatment strategies. *Lancet* **2007**, *369*, 1742-1757.

3. Landry, C.S.; McMasters, K.M.; Scoggins, C.R., The evolution of the management of regional lymph nodes in melanoma. *J Surg Oncol* **2007**, *96*, 316-321.

4. Hellman, S.; Harris, J.R., The appropriate breast cancer paradigm. *Cancer Res* **1987**, *47*, 339-342.

5. Hawley, A.E.; Davis, S.S.; Illum, L., Targeting of colloids to lymph-nodes - influence of lymphatic physiology and colloidal characteristics. *Adv Drug Deliver Rev* **1995**, *17*, 129-148.

6. Moghimi, S.M.; Rajabi-Siahboomi, R., Advanced colloid-based systems for efficient delivery of drugs and diagnostic agents to the lymphatic tissues. *Prog Biophys Mol Biol* **1996**, *65*, 221-249.

7. O'Driscoll, C.M., Anatomy and physiology of the lymphatics. In *Lymphatic transport of drugs*, Charman, W.N.; Stella, V.J., Eds. CRC Press: Boca Raton, 1992; pp 1-35.

8. Strand, S.E.; Bergqvist, L., Radiolabeled colloids and macromolecules in the lymphatic system. *Crit Rev Ther Drug Carrier Syst* **1989**, *6*, 211-238.

9. Aukland, K.; Reed, R.K., Interstitial-lymphatic mechanisms in the control of extracellular fluid volume. *Physiol Rev* **1993**, *73*, 1-78.

10. Alberts, B., Molecular biology of the cell. In 4th ed.; Garland Science: New York, 2002; pp 1090-1113.

11. Liu, N.F., Trafficking of hyaluronan in the interstitium and its possible implications. *Lymphology* **2004**, *37*, 6-14.

12. Leu, A.J.; Berk, D.A.; Lymboussaki, A.; Alitalo, K.; Jain, R.K., Absence of functional lymphatics within a murine sarcoma: A molecular and functional evaluation. *Cancer Res* **2000**, *60*, 4324-4327.

13. Padera, T.P.; Kadambi, A.; di Tomaso, E.; Carreira, C.M.; Brown, E.B.; Boucher, Y.; Choi, N.C.; Mathisen, D.; Wain, J.; Mark, E.J*., et al.*, Lymphatic metastasis in the absence of functional intratumor lymphatics. *Science* **2002**, *296*, 1883-1886.

14. Harrell, M.I.; Iritani, B.M.; Ruddell, A., Tumor-induced sentinel lymph node lymphangiogenesis and increased lymph flow precede melanoma metastasis. *Am J Pathol* **2007**, *170*, 774-786.

15. White, V.; Harvey, J.R.; Griffith, C.D.; Youssef, M.; Carr, M., Sentinel lymph node biopsy in early breast cancer surgery--working with the risks of vital blue dye to reap the benefits. *Eur J Surg Oncol* **2011**, *37*, 101-108.

16. Balch, C.M.; Gershenwald, J.E.; Soong, S.J.; Thompson, J.F.; Atkins, M.B.; Byrd, D.R.; Buzaid, A.C.; Cochran, A.J.; Coit, D.G.; Ding, S.L., *et al.*, Final version of 2009 ajcc melanoma staging and classification. *J Clin Oncol* **2009**, *27*, 6199-6206.

17. Porter, C.J., Drug delivery to the lymphatic system. *Crit Rev Ther Drug Carrier Syst* **1997**, *14*, 333-393.

18. Rao, D.A.; Forrest, M.L.; Alani, A.W.; Kwon, G.S.; Robinson, J.R., Biodegradable plga based nanoparticles for sustained regional lymphatic drug delivery. *J Pharm Sci* **2010**, *99*, 2018-2031.

19. Casley-Smith, J.R., The fine structure and functioning of tissue channels and lymphatics. *Lymphology* **1980**, *13*, 177-183.

20. Oussoren, C.; Storm, G., Liposomes to target the lymphatics by subcutaneous administration. *Adv Drug Deliv Rev* **2001**, *50*, 143-156.

21. Takada, M.; Hattori, S., Presence of fenestrated capillaries in skin. *Anat Rec* **1972**, *173*, 213-219.

22. Imayama, S., Scanning and transmission electron-microscope study on the terminal blood-vessels of the rat skin. *J Invest Dermatol* **1981**, *76*, 151-157.

23. Sarin, H., Physiologic upper limits of pore size of different blood capillary types and another perspective on the dual pore theory of microvascular permeability. *J Angiogenes Res* **2010**, *2*, 14.

24. Takakura, Y.; Hashida, M.; Sezaki, H., Lymphatic transport after parenteral drug administration. In *Lymphatic transport of drugs*, Charman, W.N.; Stella, V.J., Eds. CRC Press: Boca Raton, 1992; pp 255-278.

25. Patel, H.M.; Boodle, K.M.; Vaughan-Jones, R., Assessment of the potential uses of liposomes for lymphoscintigraphy and lymphatic drug delivery. Failure of 99m-technetium marker to represent intact liposomes in lymph nodes. *Biochim Biophys Acta* **1984**, *801*, 76-86.

26. Takakura, Y.; Atsumi, R.; Hashida, M.; Sezaki, H., Development of a novel polymeric prodrug of mitomycin c, mitomycin c-dextran conjugate with anionic charge. Ii. Disposition and pharmacokinetics following intravenous and intramuscular administration. *Int J Pharm* **1987**, *37*, 145-154.

27. Hawley, A.E.; Illum, L.; Davis, S.S., Lymph node localisation of biodegradable nanospheres surface modified with poloxamer and poloxamine block co-polymers. *FEBS Lett* **1997**, *400*, 319-323.

28. Barrett, T.; Choyke, P.L.; Kobayashi, H., Imaging of the lymphatic system: New horizons. *Contrast Media Mol Imaging* **2006**, *1*, 230-245.

29. Lucarelli, R.T.; Ogawa, M.; Kosaka, N.; Turkbey, B.; Kobayashi, H.; Choyke, P.L., New approaches to lymphatic imaging. *Lymphat Res Biol* **2009**, *7*, 205-214.

30. Ross, M.I., Sentinel node biopsy for melanoma: An update after two decades of experience. *Semin Cutan Med Surg* **2011**, *29*, 238-248.

31. Gould, E.A.; Winship, T.; Philbin, P.H.; Kerr, H.H., Observations on a "Sentinel node" In cancer of the parotid. *Cancer* **1960**, *13*, 77-78.

32. Lam, T.K.; Uren, R.F.; Scolyer, R.A.; Quinn, M.J.; Shannon, K.F.; Thompson, J.F., False-negative sentinel node biopsy because of obstruction of lymphatics by metastatic melanoma: The value of ultrasound in conjunction with preoperative lymphoscintigraphy. *Melanoma Res* **2009**, *19*, 94-99.

33. Cochran, A.J.; Roberts, A.A.; Saida, T., The place of lymphatic mapping and sentinel node biopsy in oncology. *Int J Clin Oncol* **2003**, *8*, 139-150.

34. Hindie, E.; Groheux, D.; Brenot-Rossi, I.; Rubello, D.; Moretti, J.L.; Espie, M., The sentinel node procedure in breast cancer: Nuclear medicine as the starting point. *J Nuc Med* **2011**, *52*, 405-414.

35. Plut, E.M.; Hinkle, G.H.; Guo, W.; Lee, R.J., Kit formulation for the preparation of radioactive blue liposomes for sentinel node lymphoscintigraphy. *J Pharm Sci* **2002**, *91*, 1717-1732.

36. Fujimoto, Y.; Okuhata, Y.; Tyngi, S.; Namba, Y.; Oku, N., Magnetic resonance lymphography of profundus lymph nodes with liposomal gadolinium-diethylenetriamine pentaacetic acid. *Biol Pharm Bull* **2000**, *23*, 97-100.

37. Misselwitz, B.; Sachse, A., Interstitial mr lymphography using gd-carrying liposomes. *Acta Radiol Suppl* **1997**, *412*, 51-55.

38. Trubetskoy, V.S.; Cannillo, J.A.; Milshtein, A.; Wolf, G.L.; Torchilin, V.P., Controlled delivery of gd-containing liposomes to lymph nodes: Surface modification may enhance mri contrast properties. *Magn Reson Imaging* **1995**, *13*, 31-37.

39. Kobayashi, H.; Brechbiel, M.W., Nano-sized mri contrast agents with dendrimer cores. *Adv Drug Deliv Rev* **2005**, *57*, 2271-2286.

40. Kobayashi, H.; Kawamoto, S.; Bernardo, M.; Brechbiel, M.W.; Knopp, M.V.; Choyke, P.L., Delivery of gadolinium-labeled nanoparticles to the sentinel lymph node: Comparison of the sentinel node visualization and estimations of intra-nodal gadolinium concentration by the magnetic resonance imaging. *J Control Release* **2006**, *111*, 343-351.

41. Kobayashi, H.; Kawamoto, S.; Sakai, Y.; Choyke, P.L.; Star, R.A.; Brechbiel, M.W.; Sato, N.; Tagaya, Y.; Morris, J.C.; Waldmann, T.A., Lymphatic drainage imaging of breast cancer in mice by micro-magnetic resonance lymphangiography using a nano-size paramagnetic contrast agent. *J Nat Cancer Inst* **2004**, *96*, 703-708.

42. Kaledin, V.I.; Matienko, N.A.; Nikolin, V.P.; Gruntenko, Y.V.; Budker, V.G., Intralymphatic administration of liposome-encapsulated drugs to mice: Possibility for suppression of the growth of tumor metastases in the lymph nodes. *J Natl Cancer Inst* **1981**, *66*, 881-887.

43. Osborne, M.P.; Richardson, V.J.; Jeyasingh, K.; Ryman, B.E., Potential applications of radionuclide-labelled liposomes in the detection of the lymphatic spread of cancer. *Int J Nucl Med Biol* **1982**, *9*, 47-51.

44. Tumer, A.; Kirby, C.; Senior, J.; Gregoriadis, G., Fate of cholesterol-rich liposomes after subcutaneous injection into rats. *Biochim Biophys Acta* **1983**, *760*, 119-125.

45. Hirano, K.; Hunt, C.A., Lymphatic transport of liposome-encapsulated agents: Effects of liposome size following intraperitoneal administration. *J Pharm Sci* **1985**, *74*, 915-921.

46. Oussoren, C.; Zuidema, J.; Crommelin, D.J.; Storm, G., Lymphatic uptake and biodistribution of liposomes after subcutaneous injection. Ii. Influence of liposomal size, lipid compostion and lipid dose. *Biochim Biophys Acta* **1997**, *1328*, 261-272.

47. Barenholz, Y.; Amselem, S.; Goren, D.; Cohen, R.; Gelvan, D.; Samuni, A.; Golden, E.B.; Gabizon, A., Stability of liposomal doxorubicin formulations: Problems and prospects. *Med Res Rev* **1993**, *13*, 449-491.

48. Soundararajan, A.; Bao, A.; Phillips, W.T.; Perez Iii, R.; Goins, B.A., [(186)Re]liposomal doxorubicin (Doxil): In vitro stability, pharmacokinetics, imaging and biodistribution in a head and neck squamous cell carcinoma xenograft model. *Nucl Med Biol* **2009**, *36*, 515-524.

49. Gabizon, A.; Shmeeda, H.; Zalipsky, S., Pros and cons of the liposome platform in cancer drug targeting. *J Lipos Res* **2006**, *16*, 175-183.

50. Chen, J.H.; Ling, R.; Yao, Q.; Li, Y.; Chen, T.; Wang, Z.; Li, K.Z., Effect of small-sized liposomal adriamycin administered by various routes on a metastatic breast cancer model. *Endocr Relat Cancer* **2005**, *12*, 93-100.

51. Harrington, K.J.; Rowlinson-Busza, G.; Syrigos, K.N.; Uster, P.S.; Vile, R.G.; Stewart, J.S., Pegylated liposomes have potential as vehicles for intratumoral and subcutaneous drug delivery. *Clin Cancer Res* **2000**, *6*, 2528-2537.

52. Tejada-Berges, T.; Granai, C.O.; Gordinier, M.; Gajewski, W., Caelyx/doxil for the treatment of metastatic ovarian and breast cancer. *Expert Rev Anticancer Ther* **2002**, *2*, 143-150.

53. Frenkel, V.; Etherington, A.; Greene, M.; Quijano, J.; Xie, J.; Hunter, F.; Dromi, S.; Li, K.C., Delivery of liposomal doxorubicin (doxil) in a breast cancer tumor model: Investigation of potential enhancement by pulsed-high intensity focused ultrasound exposure. *Acad Radiol* **2006**, *13*, 469-479.

54. O'Brien, M.E.; Wigler, N.; Inbar, M.; Rosso, R.; Grischke, E.; Santoro, A.; Catane, R.; Kieback, D.G.; Tomczak, P.; Ackland, S.P.*, et al.*, Reduced cardiotoxicity and comparable efficacy in a phase iii trial of pegylated liposomal doxorubicin hcl (caelyx/doxil) versus conventional doxorubicin for first-line treatment of metastatic breast cancer. *Ann Oncol* **2004**, *15*, 440-449.

55. Prescott, L.M., Doxil offers hope to ks sufferers. *J Int Assoc Physicians AIDS Care* **1995**, *1*, 43-44.

56. O'Shaughnessy, J.A., Pegylated liposomal doxorubicin in the treatment of breast cancer. *Clin Breast Cancer* **2003**, *4*, 318-328.

57. O'Brien, M.E.R.; Wigler, N.; Inbar, M.; Rosso, R.; Grischke, E.; Santoro, A.; Catane, R.; Kieback, D.G.; Tomczak, P.; Ackland, S.P.*, et al.*, Reduced cardiotoxicity and comparable efficacy in a phase iii trial of pegylated liposomal doxorubicin hcl (CAELYX™/Doxil®) versus conventional doxorubicin for first-line treatment of metastatic breast cancer. *Ann Oncol* **2004**, *15*, 440-449.

58. Keller, A.M.; Mennel, R.G.; Georgoulias, V.A.; Nabholtz, J.M.; Erazo, A.; Lluch, A.; Vogel, C.L.; Kaufmann, M.; von Minckwitz, G.; Henderson, I.C.*, et al.*, Randomized phase III trial of pegylated liposomal doxorubicin versus vinorelbine or mitomycin c plus vinblastine in women with taxane-refractory advanced breast cancer. *J Clin Oncol* **2004**, *22*, 3893-3901.

59. Kleiter, M.M.; Yu, D.; Mohammadian, L.A.; Niehaus, N.; Spasojevic, I.; Sanders, L.; Viglianti, B.L.; Yarmolenko, P.S.; Hauck, M.; Petry, N.A.*, et al.*, A tracer dose of technetium-99m-labeled liposomes can estimate the effect of hyperthermia on intratumoral doxil extravasation. *Clin Cancer Res* **2006**, *12*, 6800-6807.

60. Ling, R.; Li, Y.; Yao, Q.; Chen, T.; Zhu, D.; Jun, Y.; Chen, J., Lymphatic chemotherapy induces apoptosis in lymph node metastases in a rabbit breast carcinoma model. *J Drug Target* **2005**, *13*, 137-142.

61. Oussoren, C.; Storm, G., Lymphatic uptake and biodistribution of liposomes after subcutaneous injection: Iii. Influence of surface modification with poly(ethyleneglycol). *Pharm Res* **1997**, *14*, 1479-1484.

62. Khato, J.; Priester, E.R.; Sieber, S.M., Enhanced lymph node uptake of melphalan following liposomal entrapment and effects on lymph node metastasis in rats. *Cancer Treat Rep* **1982**, *66*, 517-527.

63. Khato, J.; del Campo, A.A.; Sieber, S.M., Carrier activity of sonicated small liposomes containing melphalan to regional lymph nodes of rats. *Pharmacology* **1983**, *26*, 230-240.

64. Phillips, W.T.; Klipper, R.; Goins, B., Novel method of greatly enhanced delivery of liposomes to lymph nodes. *J Pharmacol Exp Ther* **2000**, *295*, 309-313.

65. Kaminskas, L.M.; Porter, C.J., Targeting the lymphatics using dendritic polymers (dendrimers). *Adv Drug Deliv Rev* **2011**, *63*, 890-900.

66. Parveen, S.; Misra, R.; Sahoo, S.K., Nanoparticles: A boon to drug delivery, therapeutics, diagnostics and imaging. *Nanomedicine* **2011 [Epub ahead of print]**.

67. Roberts, J.C.; Bhalgat, M.K.; Zera, R.T., Preliminary biological evaluation of polyamidoamine (pamam) starburst dendrimers. *J Biomed Mater Res* **1996**, *30*, 53-65.

68. Kobayashi, H.; Brechbiel, M.W., Dendrimer-based nanosized mri contrast agents. *Curr Pharm Biotechnol* **2004**, *5*, 539-549.

69. McNerny, D.Q.; Leroueil, P.R.; Baker, J.R., Understanding specific and nonspecific toxicities: A requirement for the development of dendrimer-based pharmaceuticals. *Wiley Interdiscip Rev Nanomed Nanobiotechnol* **2010**, *2*, 249-259.

70. Jain, N.K.; Asthana, A., Dendritic systems in drug delivery applications. *Expert Opin Drug Deliv* **2007**, *4*, 495-512.

71. Jevprasesphant, R.; Penny, J.; Jalal, R.; Attwood, D.; McKeown, N.B.; D'Emanuele, A., The influence of surface modification on the cytotoxicity of pamam dendrimers. *Int J Pharm* **2003**, *252*, 263-266.

72. Wijagkanalan, W.; Kawakami, S.; Hashida, M., Designing dendrimers for drug delivery and imaging: Pharmacokinetic considerations. *Pharm Res* **2011**, *28*, 1500-1519.

73. Takada, M.; Hattori, S., Presence of fenestrated capillaries in skin. *Anat Rec* **1972**, *173*, 213-220.

74. Imayama, S., Scanning and transmission electron-microscope study on the terminal blood-vessels of the rat skin. *J Invest Dermatol* **1981**, *76*, 151-157.

75. Jain, K.; Kesharwani, P.; Gupta, U.; Jain, N.K., Dendrimer toxicity: Let's meet the challenge. *Int J Pharm* **2010**, *394*, 122-142.

76. Klostranec, J.M.; Chan, W.C.W., Quantum dots in biological and biomedical research: Recent progress and present challenges. *Adv Mater* **2006**, *18*, 1953-1964.

77. Lin, P.; Chen, J.W.; Chang, L.W.; Wu, J.P.; Redding, L.; Chang, H.; Yeh, T.K.; Yang, C.S.; Tsai, M.H.; Wang, H.J*., et al.*, Computational and ultrastructural toxicology of a nanoparticle, quantum dot 705, in mice. *Environ Sci Technol* **2008**, *42*, 6264-6270.

78. Ballou, B.; Lagerholm, B.C.; Ernst, L.A.; Bruchez, M.P.; Waggoner, A.S., Noninvasive imaging of quantum dots in mice. *Bioconjug Chem* **2004**, *15*, 79-86.

79. Pelley, J.L.; Daar, A.S.; Saner, M.A., State of academic knowledge on toxicity and biological fate of quantum dots. *Toxicol Sci* **2009**, *112*, 276-296.

80. Hilderbrand, S.A.; Weissleder, R., Near-infrared fluorescence: Application to in vivo molecular imaging. *Curr Opin Chem Biol* **2010**, *14*, 71-79.

81. Choi, H.S.; Liu, W.; Misra, P.; Tanaka, E.; Zimmer, J.P.; Itty Ipe, B.; Bawendi, M.G.; Frangioni, J.V., Renal clearance of quantum dots. *Nat Biotechnol* **2007**, *25*, 1165-1170.

82. Hawley, A.E.; Illum, L.; Davis, S.S., Preparation of biodegradable, surface engineered plga nanospheres with enhanced lymphatic drainage and lymph node uptake. *Pharm Res* **1997**, *14*, 657-661.

83. Takakura, Y.; Matsumoto, S.; Hashida, M.; Sezaki, H., Enhanced lymphatic delivery of mitomycin c conjugated with dextran. *Cancer Res* **1984**, *44*, 2505-2510.

84. Jeong, Y.I.; Kim, S.T.; Jin, S.G.; Ryu, H.H.; Jin, Y.H.; Jung, T.Y.; Kim, I.Y.; Jung, S., Cisplatin-incorporated hyaluronic acid nanoparticles based on ion-complex formation. *J Pharm Sci* **2008**, *97*, 1268-1276.

85. Cai, S.; Xie, Y.; Bagby, T.R.; Cohen, M.S.; Forrest, M.L., Intralymphatic chemotherapy using a hyaluronan-cisplatin conjugate. *J Surg Res* **2008**, *147*, 247-252.

Chapter 2. Development of Hyaluronan (HA)-Fluorescent Dye Conjugates and the Molecular Weight Optimization of HA for Intralymphatic Delivery Using *in vivo* Fluorescence Imaging

2.1 Introduction

Cancer cells can metastasize by either the lymphatic or vascular routes, but many cancers, including melanoma and breast cancer, metastasize preferentially via the lymphatics [1-3]. The sentinel lymph node (SLN) status is important for staging cancers and formulating the treatment plan. Therefore developing a multifunctional platform that can both identify the sentinel lymph node and treat the lymphatic metastases, would be pivotal in treating lymphatically metastatic cancers such as melanoma and breast cancer.

Drugs can enter the lymphatics from the vascular system or from the interstitial space after subcutaneous injection. Size is the predominant biophysical property that affects lymphatic uptake, but charge, chemistry, and hydrophobicity also affect the kinetics of both passive and macrophagal uptake [4,5]. Lymphatic capillaries consist of a single layer of non-fenestrated endothelial cells that lack a continuous basal lamina [6]. There is a considerable amount of overlapping and gapping within the intercellular junctions, leading to the formation of clefts and pores along the capillary. These gaps allow the preferential uptake of materials within a specific size range (ca. 10 to 100 nm) and are the basis of lymphatic recycling of extracellular proteins, fluids, and lipids, from the interstium to the systemic circulation [5,7,8]. Particles larger than 100 nm are diffusion limited and tend to form a depot at the injection site, and particles less than 10 nm are reabsorbed by the blood capillaries. Further, it has been shown that particulates carrying a net negative charge have enhanced lymphatic uptake and retention in draining lymph nodes [5,9-11].

For effective tissue penetration and enhanced signal to noise ratio for *in vivo* imaging, the utilized fluorophore must emit in the near infrared range (600-1000 nm) to minimize background fluorescence from hemoglobin, and the autofluorescence of elastin, collagen, chlorophyll (from food), and various other biological chromophores [12,13]. The two chromophores commonly used for *in vivo* imaging are quantum dots (QDs) and NIR organic fluorophores. In the last decade, QDs have been investigated extensively for *in vivo* imaging, due to their inherently bright fluorescence, narrow emission spectra, high quantum yields, and small size (5 to 20 nm) [14,15]. Further, their enhanced imaging depth, photostability, and broad absorption bands coupled with narrow emission spectra, are beneficial characteristics for *in vivo* imaging in the NIR range, which most conventional NIR dyes lack. However, the principal concern with the use of QDs is the toxicity associated with the use of heavy metals (e.g. Cd, Te, and Se) used in the construction of the QD cores. The size and charge of the QD dictate their clearance mechanism and residence time *in vivo*. Because of the considerable toxicity concerns, the size of the QDs is limited to less than 6 nm to ensure renal clearance and minimize tissue exposure [12,16]. Larger and negatively to neutrally charged (i.e. PEG coated) QDs have shown significantly prolonged liver and spleen retention, from 1 to 6 months [14,15]. Quantum dots are appealing nanodevices for lymphatic imaging and drug delivery given their photostability, optimum size range, and rich surface groups for the conjugation of drugs and ligands. However, their long bioresidence time and potential heavy metal toxicity preclude clinical development, therefore we developed a NIR organic fluorophore-polymer conjugate with low potential toxicity for *in vivo* imaging or drug delivery applications. One polymer well suited for delivery and imaging applications to the lymphatic system is hyaluronan.

Hyaluronan (HA) is a naturally occurring linear biopolymer consisting of repeating disaccharide units of β(1,4)-D glucuronic acid-β(1,3) N-acetyl-D-glucosamine, found in the extracellular matrix (ECM), synovial fluid, umbilical cord, and vitreous humor of the eye with a molecular weight ranging from 10^5 to 10^7 Da. Hyaluronan has multiple biological roles important to cancer including modulation of inflammation, angiogenesis, and cell proliferation, and the effects can be pro- or antagonistic depending on the molecular weight [17-20].

Hyaluronan is mainly found in the ECM, and approximately half of the total HA is found in the dermis and epidermis (ca. 7 to 8 g in the average adult) [21]. The turnover of HA is relatively short, with a half life of ca. 12 hours [22]. The turnover of HA is not from its degradation in the ECM, but from one of two mechanisms: 1) local cell-mediated catabolism or 2) drainage into the lymphatics where is it then catabolized by the lymph nodes, liver and spleen [23]. The concentration of HA in the lymph is 10 to 100 times higher than in the plasma, suggesting that the major route of HA entering the plasma is through its lymphatic uptake from the ECM [22]. In addition to HA meeting the requirements for lymphatic uptake, and its natural elimination route through the lymphatics, its primary receptors, CD44 and RHAMM (receptor for HA mediated motility), are overexpressed on most malignant cancer cells [19,20,24] including invasive breast cancer and melanoma [25]. Further, it has been shown that malignant cells with a high metastatic potential have enhanced HA binding and internalization [19,20], making HA an ideal candidate for a lymphatic carrier. In addition, HA is FDA approved and has multiple functional groups for conjugation of imaging agents or chemotherapeutics.

Our previous studies targeted lymphatic drug delivery of 35-kD HA-chemotherapeutic (cisplatin and doxorubicin) conjugates have shown its improved efficacy, decreased toxicity, and superior pharmacokinetics compared to their standard iv counterparts [26-31]. Herein, we describe the kinetics of lymphatic uptake of a series of different molecular weight (6.4 kD to 697 kD, radius of gyration (R_g) $\approx$ 7 to 100 nm, respectively) hyaluronan-NIR dye (IR820) conjugates after subcutaneous injection. Because lymphatic uptake is mainly dependent on the size of particles injected into the extracellular space, the molecular weights of hyaluronan that were chosen to fall around the optimal size range for lymphatic uptake, 10 to 100 nm. The molecular weights examined were 6.4, 35, 74, 132, 357, and 697 kD. Their corresponding sizes (Table 2.1) were calculated according to the equations derived from Takahashi et al. data for radius of gyration (R_g) and hydrodynamic radius (R_h) for different molecular weights of HA in 0.2 M NaCl at 25°C [32]. The following equations were developed after fitting the data reported:

$$R_g = 2.35\ [MW\ (kD)]^{0.57} \qquad R_h = 0.87\ [MW\ (kD)]^{0.63}$$

HA MW (kD)	**R_g (nm)**	**R_h (nm)**
6.4	6.77	2.80
35	17.8	8.17
74	27.3	13.1
132	38.1	18.9
357	67.0	35.3
697	98.1	53.8

Table 2.1. Radius of gyration (R_g) and hydrodynamic radius (R_h) calculated from the fitted equations from Takahashi et al. reported data for each MW of HA used in the *in vivo* imaging [32].

2.2 Experimental

2.2.1 Synthesis of HA-Texas Red using N-(3-Dimethylaminopropyl)-N'-ethylcarbodiimide hydrochloride (EDAC) (Scheme 2.1)

Sodium hyaluronate (100 mg, 35 kD, from bacterial fermentation, Lifecore Biomedical, Chaska, MN) was dissolved in 7 mL ddH$_2$O, and the pH was adjusted to 4.75 with 0.1 M HCl. N-hydroxysuccinimide (NHS, 200 mg, Sigma) was added and allowed to stir, and the pH was maintained. Texas Red® hydrazide (2 mg, Anaspec, San Jose, CA) was dissolved in 3 mL DMSO and was added to the HA solution. EDAC (100 mg, Sigma) was added to the stirring solution, the pH was rechecked and maintained at pH 4.75. The reaction mixture was allowed to react for 48 hours at ambient temperature (ca. 20 °C), protected from the light. The resulting HA-Texas Red conjugate was purified by dialysis against ddH$_2$O for 48 hr at ambient temperature followed by lyophilization under protection from the light.

2.2.2 Synthesis of HA-Texas Red using 2-chloro-1-methylpyridinium iodide (CMPI) (Scheme 2.1)

Sodium hyaluronate (100 mg, 35 kD, Lifecore Biomedical) was dissolved in 3 mL ddH$_2$O, followed by the addition of 7 mL EtOH and was activated by the addition of CMPI (33 mg, Sigma) and triethylamine (35 μL). Texas Red® hydrazide (2 mg, in 0.4 mL DMSO, Anaspec, San Jose, CA) was added to the HA activated solution. The reaction mixture was allowed to reflux for 48 hr, protected from the light. The resulting HA-Texas Red conjugate was purified by dialysis against ddH$_2$O for 48 hr at ambient temperature followed by lyophilization under protection from the light.

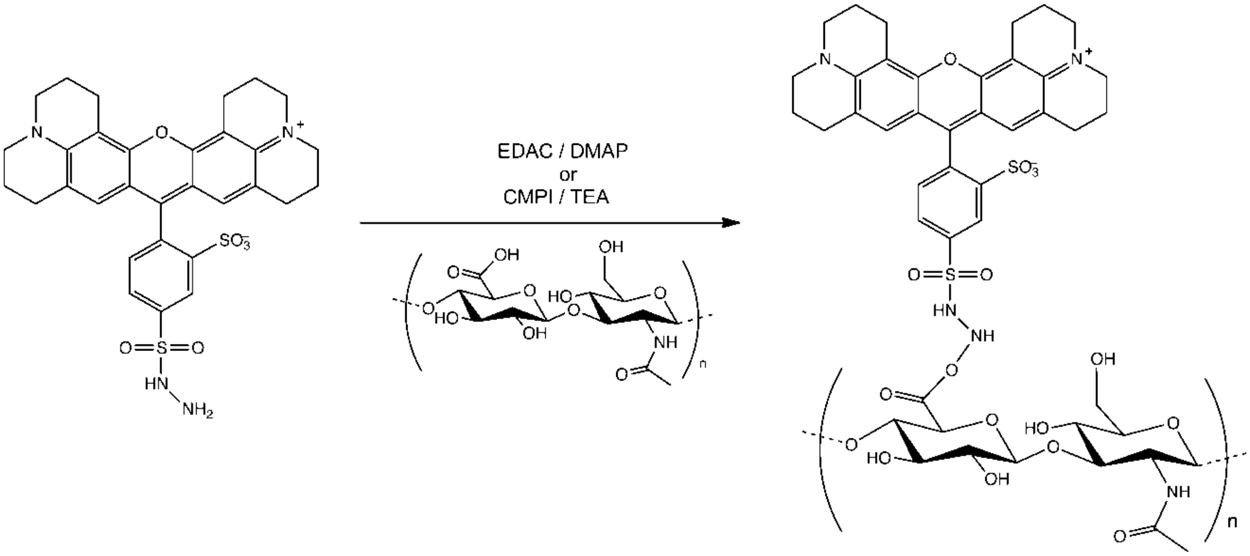

Scheme 2.1. Texas Red conjugation reaction to HA using either EDAC and DMAP (pH 4.75, 30:70 DMSO:ddH_2O, ambient temperature, ca. 20 °C) or CMPI and TEA (70:30 EtOH:ddH_2O, reflux).

2.2.3 Characterization of HA-Texas Red Conjugates

The loading degree of Texas Red for both the EDAC and CMPI conjugation methods was determined by UV spectroscopy at 588 nm using a calibration curve (0.25 to 5 μg/mL) in ddH_2O. A series of Texas Red hydrazide concentrations were prepared from a 5 mg/mL stock solution of Texas Red hydrazide in DMSO.

Conjugation of Texas Red to HA was verified by equivalent size exclusion chromatography (SEC) retention times using refractive index (Shimadzu RID-10A) and fluorescence detection (Shimadzu RF 535, $\lambda_{ex}/\lambda_{em}$ = 590/610 nm). All SECs were collected using a Shodex OHpak SB-806M HQ column thermostated at 35°C using ddH_2O at 0.75 mL/min as the mobile phase.

2.2.4 In Vivo Imaging with HA-Texas Red

A nude mouse bearing a 100- to 300-mm^3 MDA-MB-468LN breast tumor was anesthetized using isoflurane, and was injected s.c. over the left mammary fatpad with HA-Texas Red (20 μL, 10 mg/mL in saline). The injection area was massaged gently for 5 min and the mouse was fluorescently imaged after 5 and 18 h (CRI Maestro Flex; CRI Inc., Woburn, MA) using a 445-490-nm filtered halogen excitation light and a 515-nm longpass emission filter. Fluorescence was measured in 10-nm bandpass segments from 520 to 720 nm, using a cooled CCD camera with autoexposure. Images were spectrally unmixed by using the automatic deconvolution tools (Maestro version 2.4) to limit skin and intestinal autofluorescence resulting from chlorophyll in the food.

2.2.5 Synthesis of 5-carboxypentyl-amino-IR-820 (Scheme 2.2)

The 6-aminohexanoic acid (2 eq., Sigma) was dissolved in 20 mL dry DMF with 2 eq. of triethylamine, and the solution was stirred under argon for ca. 5 min. After the addition of 500 mg (0.47 mmol) of IR-820 (Sigma), the reaction mixture was refluxed at 85°C for 3 hrs in the dark. The solvent was removed under reduced pressure, and the 5-carboxypentyl-amino-IR-820 was purified by silica column chromatography using a gradient of 2:1 to 1:1 ethyl acetate:methanol. The blue 5-carboxypentyl-amino-IR-820 solid was confirmed by ^{1}H NMR (400 MHz, Bruker) in $CDCl_3$ (Cambridge Isotope Laboratories, Andover, MA); ^{1}H-NMR ($CDCl_3$, 400 MHz): δ = 8.13 (d, *J* = 8.4 Hz, 2H), 7.98-7.91 (m, 4H), 7.63 (d, *J* = 13.2 Hz, 2H), 7.56-7.52 (m, 4H), 7.35 (t, *J* = 8.0 Hz, 2H), 5.77 (d, *J* = 15.2 Hz, 2H), 4.06-4.00 (m, 4H), 3.05 (q, *J* = 12.4 Hz, 6.4 Hz, 1H), 2.57-2.51 (m 4H), 2.16 (t, *J* = 6.4 Hz, 2H), 2.07 (t, *J* = 7.2 Hz, 1H), 1.88 (bs, 11H), 1.82-1.68 (m, 14 H), 1.62-1.53 (m, 3H), 1.48-1.35 (m, 4 H), 1.28-1.22 (m, 1H).

2.2.6 Synthesis of HA-IR820 Conjugates (Scheme 2.2)

Typically 5-carboxypentyl-amino-IR-820 was dissolved in ddH_20 (<20 mL) with *N*-(3-dimethylaminopropyl)-*N*′-ethylcarbodiimide hydrochloride (EDAC, 1.2 eq., dye basis, Sigma) and 4-(dimethylamino)pyridine (DMAP, 0.5 eq., dye basis, Sigma), the pH was adjusted to 4.0 to 4.5, and the solution was stirred for approximately five minutes. Sodium hyaluronate (100 mg, Lifecore Biomedical) was dissolved in 10 mL of ddH_2O and added to the solution (see Table 2.2 for molar equivalents of reagents used). The mixture was stirred at ambient temperature (ca. 20°C) in the dark. The reaction was monitored by TLC, using 6:4:1 MeOH:EtOAc:DCM as the mobile phase; the total reaction time was typically 1 to 5 days and increased with HA molecular weight. The HA-IR820 conjugate was dialyzed once against 95% EtOH and twice against

ddH_2O. The purple HA-IR820 conjugate was lyophilized and stored at -20°C until further use. The ratio of ^{1}H NMR peaks the acetamide methyl of HA and the third methylene group on the 5-carboxypentyl-amino linker moiety, in D_2O were used to determine the dye content per HA polymer.

HA MW (kD)	**Dye Equivalents**	**EDAC Equivalents**	**DMAP Equivalents**
6.4	1.5	1.8	0.75
35	3	3.6	1.5
74	10	12	5
132	25	30	12.5
357	50	60	25
697	100	120	50

Table 2.2. Molar equivalents of each reagent used in the conjugation of 5-carboxypentyl-amino-IR-820 (dye) to each MW of HA to form the HA-IR820 conjugates.

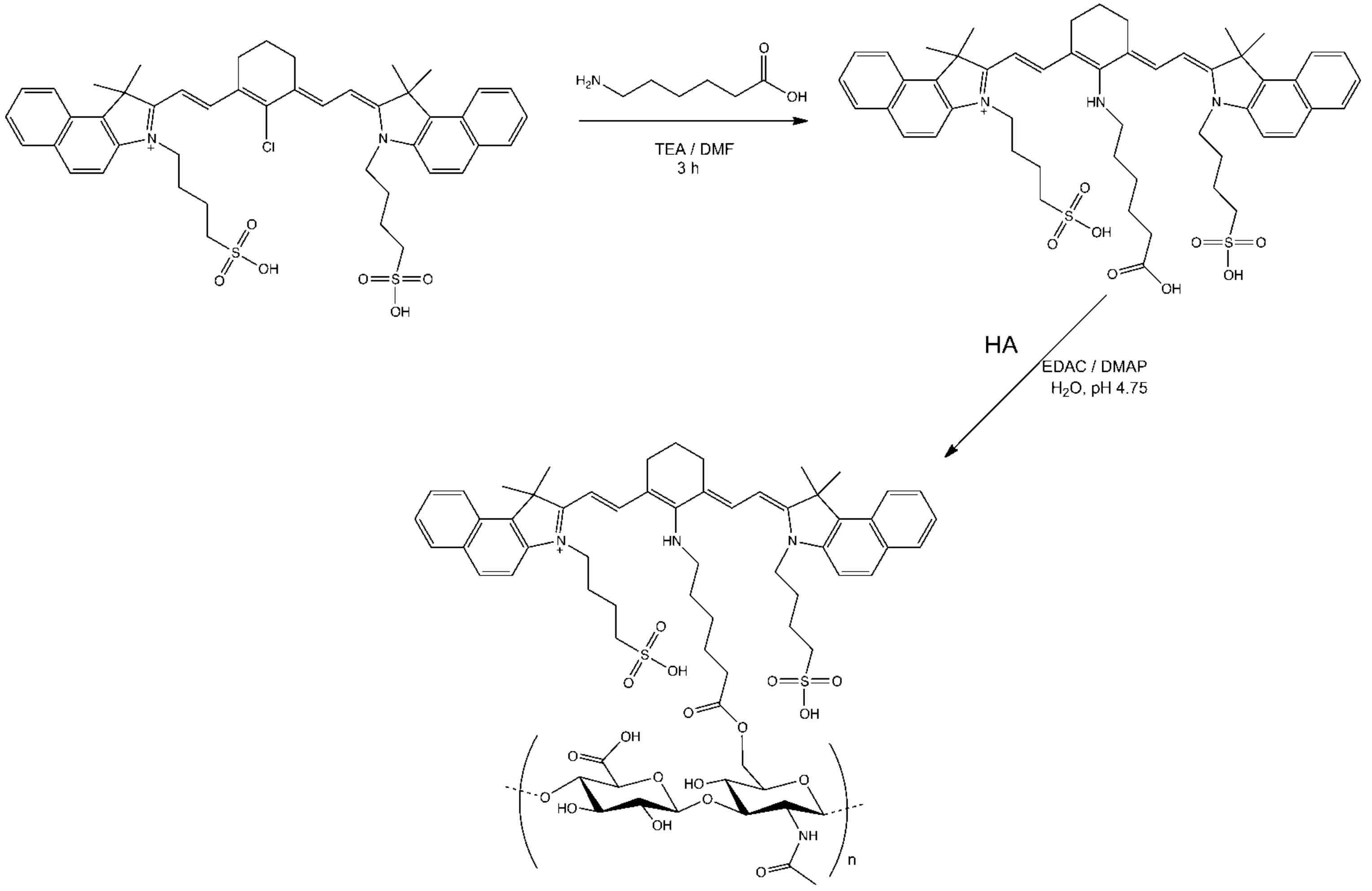

Scheme 2.2. Reaction scheme of IR-820 with 6-aminohexanoic acid to give the 5-carboxypentyl-amino-IR-820 intermediate, followed by the conjugation reaction of 5-carboxypentyl-amino-IR-820 with HA using EDAC/DMAP as the activating agent and catalyst, respectively.

2.2.7 Size Exclusion Chromatography (SEC) of HA-IR820

Conjugation of IR820 to HA was verified by equivalent SEC column retention times using evaporative light scattering (ELSD) and UV detection. HA (same MWs used in conjugation reactions) and PEG standard samples (1 mg/mL total concentration, Scientific Polymer Products, Ontario, NY) were used for a calibration curve, and the retention times of HA-IR820 were compared to that of HA and PEG to determine the molecular weight changes post conjugation reactions. All SECs were collected using a Shodex OHpak SB-806M HQ column thermostated at 35°C, with 0.8 mL/min mobile phase of 5-mM acetate buffer adjusted to pH 5. Detection was with a UV (Shimadzu LC2010CHT) (λ=520 nm) and an evaporative light scattering detector (Shimadzu ELSD-LT II, 70 °C and 3.6 bar purified air).

2.2.8 Fluorescence of HA-IR820 conjugates

The HA-IR820 samples were dissolved in ddH_2O at a concentration of 0.1 mg/mL IR820. The maximum excitation and emission wavelengths were determined using a fluorescent spectrophotometer (Shimadzu RF-5301 PC, Columbia MD; Panorama Fluorescence Software). The total fluorescence emission spectrum (λ_{ex}= 700 nm, λ_{em}=800-900 nm) was determined for the HA-IR820 samples, which was used for the normalization of the *in vivo* imaging data.

2.2.9 Zeta Potential of HA

HA samples (4.7, 6.4, 35, 74, 132, 357, and 697 kD) were dissolved at a concentration of 100 μg/mL in pH 7.25 1-mM phosphate buffer with the addition of 1 mM of KCl. After dilution, the pH was rechecked. Zeta potentials were measured on a ZetaPALS (Brookhaven Instruments Corporation, Holtsville, NY) at 20°C.

2.2.10 In Vivo Imaging of HA-IR820 Conjugates

All mice were fed a low chlorophyll diet at least one week prior to imaging to decrease food induced organ and skin autofluorescence (Harlan 2918 irradiated diet). The mouse's hair in the area of interest for imaging was removed 24 hours prior to imaging with clippers followed by depilatory cream. Female Balb/c mice (20-25 g, Charles River) (3 per group) were anesthetized under isoflurane, placed on a heating pad to help regulate body temperature, and were injected subcutaneously (s.c.) with 10 μL of a 1-mg/mL 5-carboxypentyl-amino-IR-820 or HA-IR820 (dye basis) in the center of the right hind footpad or on the inner-side of the right front forearm. The mice were imaged on both the dorsal and right sides (for footpad injections) or ventral and right sides (for front forearm injections), both with and without the injection site being covered, using whole body fluorescence imaging (Cambridge Research and Instrumentation Maestro multi-spectrum imager, Woburn, MA) using an excitation filter of 710-760 nm and broadpass emission filter of 800-950 nm. The animals were imaged for 7 days in the footpad studies and 14 days in the forearm studies. Images were acquired using the autoexposure function in the imaging software.

2.2.11 In Vivo Imaging Data Analysis of HA-IR820 Conjugates

Image analysis was performed using Maestro software (ver. 2.10). Regions of interest were placed over the popliteal and iliac lymph nodes or axillary lymph node package. The total signal (scaled counts/s) intensity values (arbitrary units, AU) were recorded for each region of interest (ROI), for all positions (dorsal, ventral, and right sides), and were plotted versus time in GraphPad Prism (ver. 4). The total emission fluorescence was determined by integrating the resultant emission spectrum (λ_{ex}= 700 nm, λ_{em}=800-900 nm) from each HA-IR820 sample (0.1

mg/mL IR820). The ROIs were normalized to their corresponding total emission fluorescence. The normalized ROI vs. time graphs were then integrated to give the cumulative fluorescence vs. time graphs. In addition, the area under the curve (AUC) was determined from the normalized ROI vs. time graphs.

$$\text{Scaled counts/s} = \text{counts/full scale} \times 1/\exp(s) \times 1/\text{bin}^2 \times 1/\text{gain}$$

2.3 Results

2.3.1 HA-Texas Red Characterization

The synthesis of Texas Red with HA using EDAC as a coupling agent was adapted from Gajewiak et al. [33]. The use of CMPI, previously used as a crosslinking agent in the preparation of covalently cross-linked HA films, was adapted as an alternative coupling reagent in the conjugation of Texas Red with HA [34,35] which we have previously reported [29].

The loading degree of Texas Red on HA for both the EDAC and CMPI conjugation reactions was determined by UV spectroscopy at 588 nm using a calibration curve (0.25-5 μg/mL) in ddH_2O. The concentrations used for the standard curve of Texas Red were 0.25, 0.375, 0.5, 0.625, 1.25, 2.5, and 5.0 μg/mL (R^2=0.994) in ddH_2O. The absorbance of the HA-Texas Red was measured at 588 nm was measured, and the resulting optical density measurements were due to the absorbance of Texas Red and not HA, as HA does not exhibit UV absorbance at 588 nm. The loading degree of Texas Red was calculated to be 2% and 4% for the EDAC and CMPI activated coupling reactions, respectively. The extinction coefficient at 588 nm of Texas Red on HA-Texas Red in ddH_2O was determined to be 81813 $M^{-1}cm^{-1}$, whereas it was reported from the manufacturer to be 100,500 $M^{-1}cm^{-1}$ in MeOH at 582 nm. The CMPI activation method for the conjugation of Texas Red to HA was used for further studies due to the higher loading degree obtained with this method.

Conjugation of Texas Red to HA was verified by equivalent retention times using size exclusion chromatography coupled with refractive index and fluorescence detection ($\lambda_{ex}/\lambda_{em}$ = 590/610 nm). Equivalent elution times for the fluorescence (from Texas Red) and refractive index (from HA-Texas Red) signals indicated that the Texas Red was bound to HA and was pure with no free Texas Red present in the sample.

2.3.2 In Vivo Imaging with HA-Texas Red

HA-Texas Red drained into the left lymphatic basins after a subcutaneous injection into the left mammary fatpad, with no observed bilateral drainage into the right basin. After 5 h, localization of HA-Texas Red in the nodes surrounding the tumor can be clearly observed (Figure 2.1 B). Most of the carrier has localized in the basin of the tumor at 18 h with a lesser amount remaining in the adjacent axillary node basins (Figure 2.1 C).

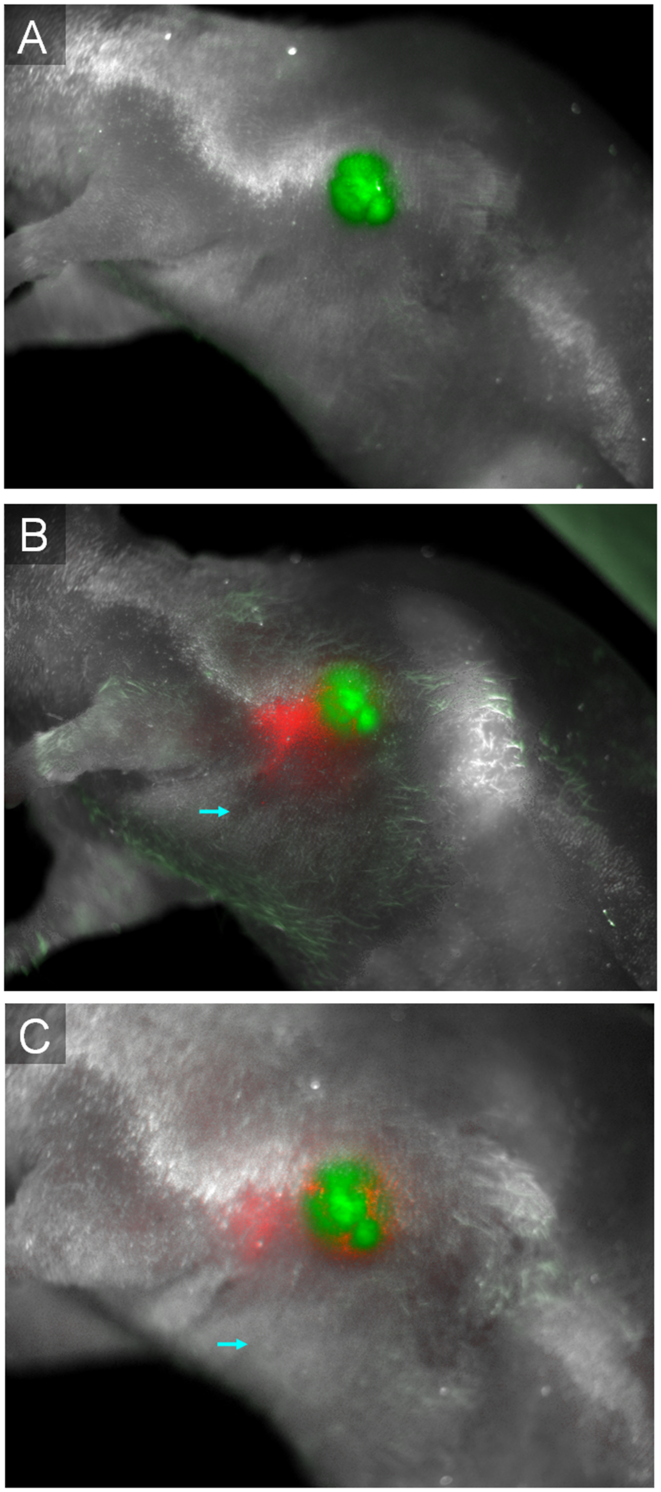

Figure 2.1. A nude mouse bearing a MDA-MB-468 breast lymphatic tumor (expressing green fluorescent protein [GFP], panel A) was subcutaneously injected with HA-Texas Red in the left mammary fat pad. After 5 hrs and 18 hrs (B and C, respectively), significant HA localization in the draining nodes, and it was co-localized with the tumor (GFP-channel in green, Texas Red channel in red, blue arrow denotes the injection site).

2.3.3 HA-IR820 Characterization

The synthesis of the HA-IR820 conjugate was adapted from Masotti et al. procedure for forming IR820 dye complexes with polyethylenimine [36]. The number of dyes per polymer (Table 2.3) were determined by the integration ratio from the ^{1}H NMR of the methyl on the acetamide of HA to the third methylene group on the linker between IR820 and HA (Scheme 2.2).

Conjugation of IR820 to HA was verified by equivalent elution times using size exclusion chromatography coupled with ELSD and UV detection (data not shown). Linear responses between molecular weight and elution time were observed for both PEG standards and HA samples (R^2=0.993 and 0.999, respectively). Both PEG and HA are linear polymers, but they exhibit drastically different characteristics in solution for the same given molecular weight. The MW of the conjugates were similar to that of the original HA used, with the exception of the highest MW of 697 kD, which exhibited a significantly lower MW than that of the original HA (Figure 2.2).

2.3.4 Spectral Properties of HA-IR820

The maximum excitation and emission wavelengths of HA-IR820 (all MWs) were determined to be 675 nm and 725 to 735 nm in H_2O, respectively, having a moderate Stokes shift of 50 to 60 nm. A blue shift in the UV absorbance was observed after each IR820 reaction (data not shown). The concentrations used for the determination of the maximum wavelengths and total emission spectra over the specified wavelengths (same as used in the imaging experiments), was a 1:10 dilution of that used for the imaging experiments. Larger concentrations caused self-quenching of the dyes.

HA MW (kD)	IR820 wt %	# dyes/HA polymer
6.4	2.12%	0.16
35	4.69%	1.93
74	3.21%	2.75
132	4.95%	7.72
357	4.44%	18.6
697	3.97%	32.3

Table 2.3. The IR820 loading degree, determined by ^{1}H NMR in D_2O, onto the different molecular weights of HA that were used for the *in vivo* imaging experiments.

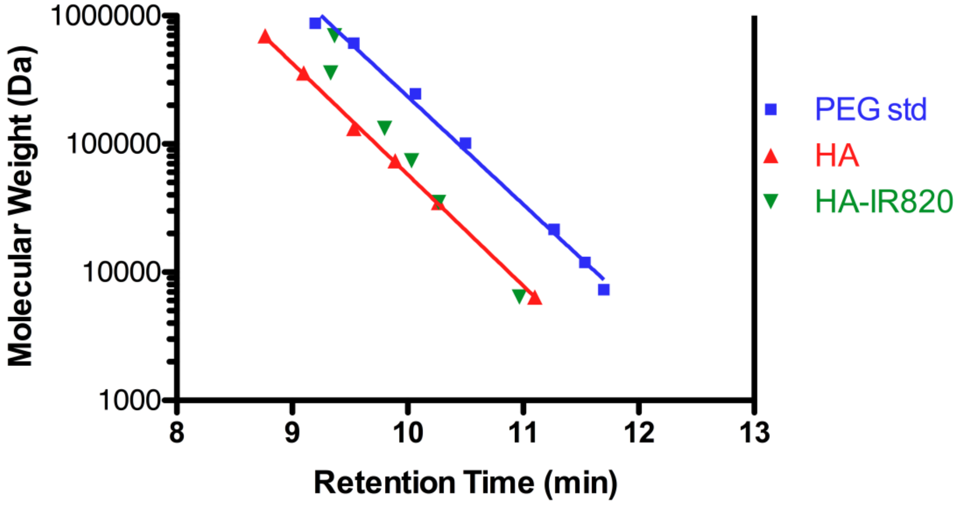

Figure 2.2. Retention time vs. molecular weight for PEG standards, HA samples, and HA-IR820 conjugates from SEC, using a Shodex OHpak SB-806M HQ column, 5 mM acetate buffer (acetic acid/ammonium acetate) at pH 5 (0.8 mL/min flow rate) coupled with UV detection (λ=520 nm) and evaporative light scattering detection (ELSD, 70 °C).

2.3.5 Zeta Potential of HA

The zeta potentials of the HA samples were determined at pH >> pK_a, to ensure that all of the carboxylic acid functional groups were fully ionized to minimize the effects of pH changes on measurements due to partial protonation of the carboxylic acids. Further, the pH studied would be indicative of the ionization state *in vivo*. The zeta potential was independent of the molecular weight of HA (R^2=0.75) (Table 2.5).

HA MW (kD)	Zeta Potential (mV)
4.7	-24.20 ± 2.44
6.4	-25.33 ± 4.19
35	-22.54 ± 2.57
74	-31.18 ± 2.26
132	-54.82 ± 2.49
357	-51.72 ± 3.06
697	-50.06 ± 3.63

Table 2.5. Zeta potentials of various different MW HAs in 1-mM phosphate buffer pH 7.25 with 1 mM KCl at HA concentration of 100 μg/mL and 25°C.

2.3.6 Optimization of In Vivo Lymphatic Imaging

The intense fluorescence signal from the injection site saturated the camera, so we covered the injection area with a piece of black tape allowing visualization of the draining lymphatic vessels and lymph nodes. The use of the autoexpose function resulted in different exposure times for each image. We corrected for this in the image analysis by using the scaled counts/s, which is normalized for the exposure time.

Mice in the footpad injection group were imaged from both their right and dorsal sides to detect drainage into the popliteal and iliac nodes. Mice in the forearm group were imaged from the right and ventral sides to capture the axillary node drainage. The same trends were observed for both imaging positions; but the right side was analyzed as it produced greater signal intensities and a higher signal to noise ratio compared to the dorsal or ventral positions. We found that the ventral position led to a decreased signal to noise ratio due to the increased fluorescence contributions of the organs in the abdomen, along with the inability to visualize the iliac node due to its increased depth in this position. With both injection sites, both the lymph nodes and draining lymphatic vessels were clearly visualized against the background tissues using fluorescence imaging (Figures 2.3 A and B).

The position of the injection site within the footpad is also of importance. We found that injections into the center of the hind footpad will drain solely into the popliteal node; however injections closer to outer edge of the footpad will drain partially into the inguinal node. This is contrary to reports by Ruddell et al. [37] stating that the inguinal node is the major draining lymph node from the hind leg. The non-central injections are not representative of the human lymph drainage since the human foot and leg drain to the popliteal node or the superficial inguinal nodes in the groin area, which correspond to the popliteal and iliac nodes on a mouse

[38]. The human lymph nodes corresponding to the mouse inguinal nodes are not the draining lymph nodes of the lower limbs in humans. Over the course of 50 injections into the rear hind footpad, the inguinal lymph node was visualized in less than 3% of mice. In addition, bilateral drainage was not observed for any of the subcutaneous injections. Due to limitations of *in vivo* fluorescence imaging, only shallow nodes were identified; we do not discount further drainage past the axillary lymph node package or iliac nodes.

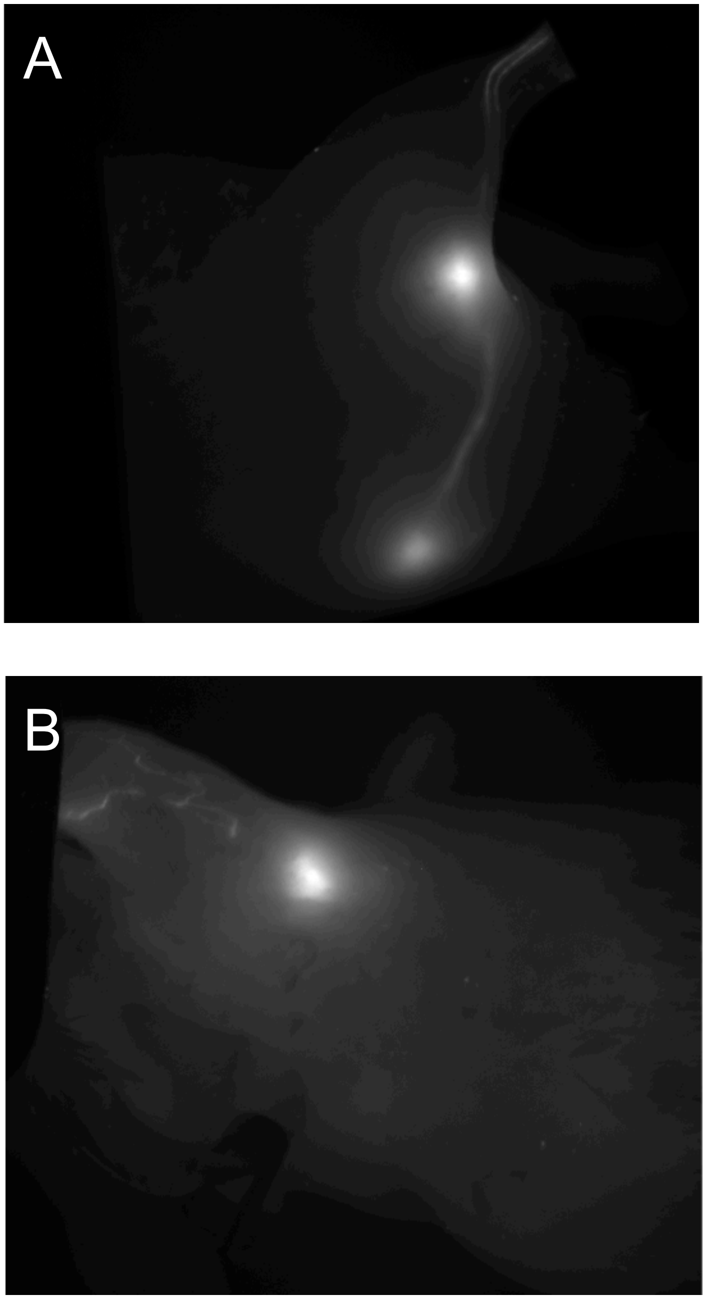

Figure 2.3. Representative images of whole body fluorescence imaging of mice imaged on their right sides after a s.c. injection of HA-IR820 into the A) right hind footpad or B) right front forearm. The A) popliteal (top lymph node), iliac (bottom lymph node), and B) axillary lymph nodes can be clearly visualized through the skin along with the draining lymphatics (lines connecting the lymph nodes). The injection sites are covered in the images in order to see the definition of the draining lymphatics.

2.3.7 In Vivo Imaging Control Experiments

An injection of free 5-carboxypentyl-amino-IR820 (free dye) was compared to HA-IR820 in both the right hind footpad and the right front forearm injections. The axillary lymph node was readily visualized through the skin less than five minutes after injection of the free dye. However with the HA-IR820 conjugates, the enhancement of the axillary node was only possible with fluorescence imaging. Drainage to the popliteal and iliac nodes was only visualized with fluorescence imaging for both the free dye and HA-IR820 conjugates. The free dye cleared rapidly from the nodes compared to the HA-IR820 conjugates. The free dye was observed in both the lymph and blood capillaries via *in vivo* imaging (data not shown), whereas the HA-IR820 conjugates were visualized only within the lymphatic capillaries. More than 75% of the free dye cleared from the lymph nodes within 20 hrs post injection, and it was completely cleared within 48 hrs (Figures 2.4 A-C).

Mice in the free dye footpad injection group exhibited significantly longer time to reach maximal fluorescence (t_{max}) compared to the HA-IR820 conjugates after the footpad injections, but for the forearm injections, the free dye and HA-IR820 groups had a similar t_{max} (Table 2.6). Because the *in vivo* fluorescence spectra of the free dye (λ_{em}=823 nm) and HA-IR820 (λ_{em}= 835 and 870 nm) are different, their individual contributions are easily identified after spectral unmixing. The nodal fluorescence signal can be attributed to the sole contribution of the intact HA-IR820 conjugate and not the free dye, after spectral unmixing. The free dye and the intact HA-IR820 were detected in the livers of mice after the injection of the HA-IR820 conjugates.

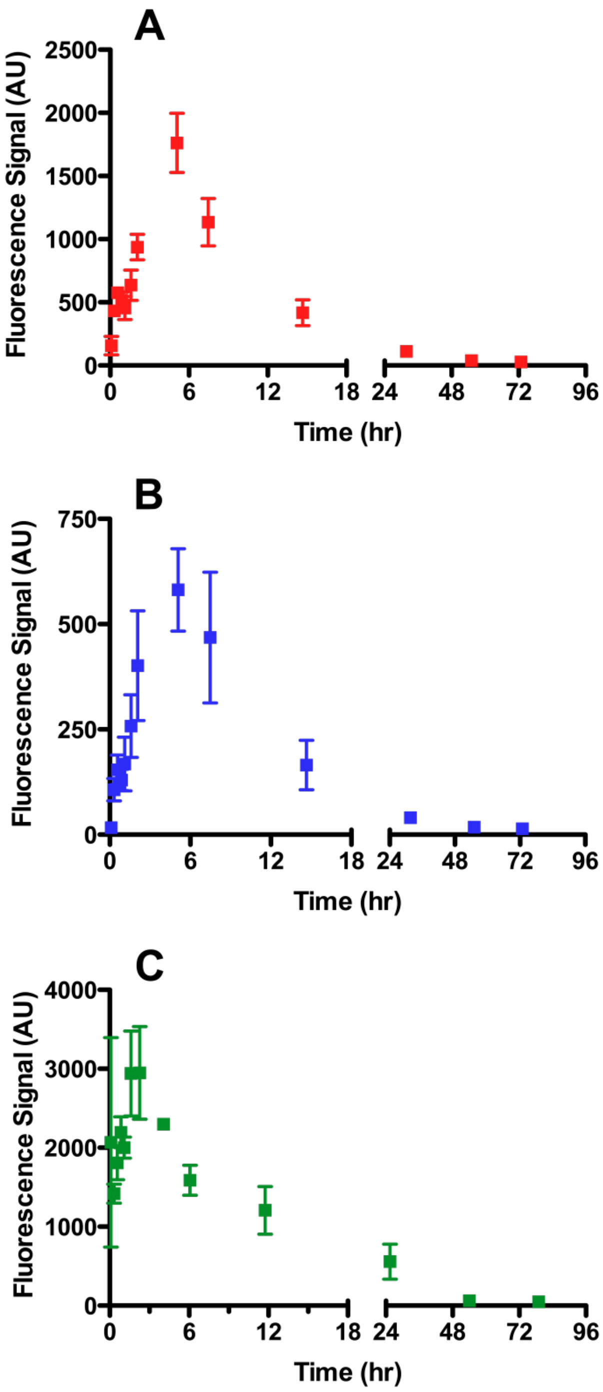

Figure 2.4. Drainage kinetics of the free dye (5-carboxypentyl-amino-IR820) into the A) popliteal (red), B) iliac (blue), and C) axillary (green) lymph nodes after a s.c. injection into the right hind footpad (corresponding to the popliteal and iliac nodes) or the right front forearm (corresponding to the axillary nodal package).

2.3.8 Molecular Weight Dependence on Lymphatic Uptake

The molecular weight dependence of lymphatic uptake was determined using six different HA-IR820 conjugates within the size range reported to have efficient lymph uptake, generally 10 to 100 nm [5,8]. Mice were injected subcutaneously in the center of the hind footpad or in the front forearm with the HA-IR820 conjugates and were imaged at predetermined time points for up to one week (footpad injections) or two weeks (forearm injections). The drainage kinetics of the HA-IR820 conjugates exhibited a similar trend for both injection sites and all three lymph nodes (Figures 2.5 A, 2.6 A, and 2.6 C). A clear trend in the MW dependence of lymphatic uptake of HA-IR820 conjugates is easily identified when looking at the total AUC of each MW conjugate (Figures 2.5 B, 2.5 C, 2.6 B, and 2.6 D). Both 6.4-kD and 74-kD HA-IR820 have greatly enhanced uptake (large AUC) compared to the other conjugates (Figure 2.5 C, 2.5 D, and 2.5 E); however, excluding the 6.4-kDa conjugate, there is a normal distribution curve over the HA molecular weight range (Figure 2.5 C), with a maximum at 74 kD. As the HA MW increased, significant retention in all three lymph nodes was observed compared to the lower molecular weight HA-IR820 conjugates, as indicated by the long $t_{50\%}$ values (time required for the fluorescence signal to reduce by 50%) (Table 2.6). Furthermore, the HA-IR820 conjugates were retained longer in the axillary lymph node package than the popliteal node for all molecular weights (Table 2.6).

	t_{max}, hrs			$t_{50\%}$, hrs		
Sample	Popliteal	Iliac	Axillary	Popliteal	Iliac	Axillary
Free IR820	5	5	1-1.5	8.4	12	6.5
6.4 kD HA-IR820	1.5	4	1	7.6	16	10
35 kD HA-IR820	1.5	2	1-2	5.7	4.6	17
74 kD HA-IR820	1.5-2	1.5-2	3	6.9	21	15
132 kD HA-IR820	1.5	2-4	4	49	30	62
357 kD HA-IR820	3	3	3-4	38	21	62
697 kD HA-IR820	3	2-3	3	47	62	72

Table 2.6. Calculated t_{max} and $t_{50\%}$ values for each of the free IR820 or HA-IR820 conjugates after image analysis and generating their corresponding time vs. fluorescence signal curves for injections into the footpad (popliteal and iliac nodes) or forearm (axillary node).

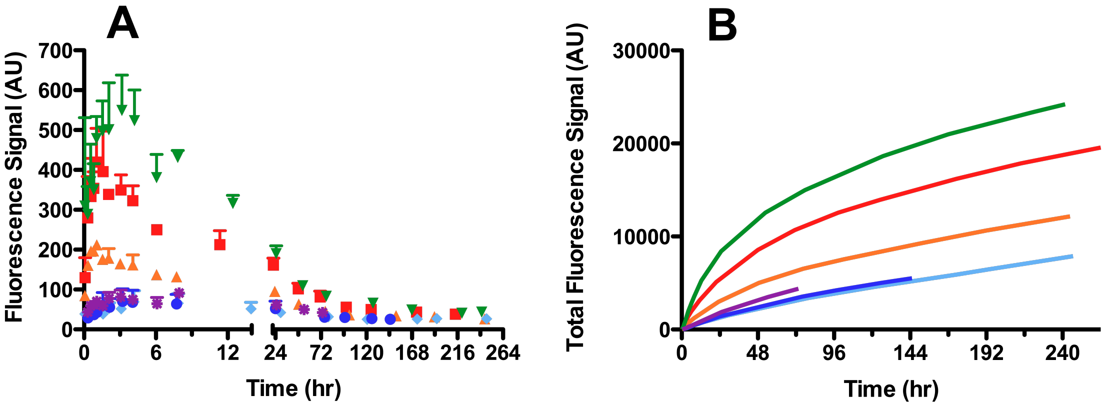

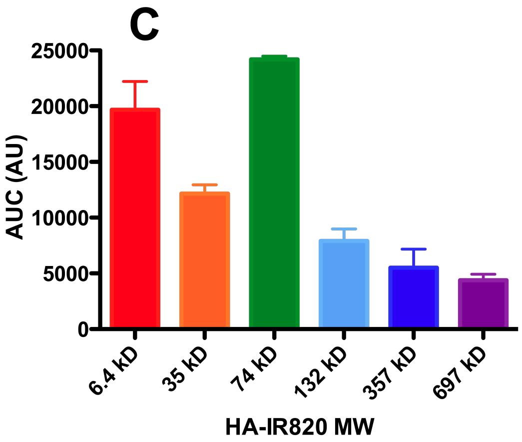

D

HA MW (kD)	AUC (AU)
6.4	19679 ± 2530
35	12155 ± 786
74	24190 ± 296
132	7897 ± 1101
357	5514 ±1669
697	4381 ± 545

Figure 2.5. Lymphatic drainage to the axillary lymph node package of different MW (6.4 kD-red squares; 35 kD-orange triangles; 74 kD-green inverted triangles; 132 kD-light blue diamonds; 357 kD-blue circles; 697 kD-purple stars) HA-IR820 conjugates after s.c. injection. Increased lymphatic uptake of the 74kD HA-IR820 conjugate into the axillary lymph node package is evident in the A) time vs. fluorescent signal and cumulative fluorescence signals seen in the B) time vs. total fluorescence signal. The MW distribution trends shown are representative of the trends seen in axillary nodal package visualized after imaging mice on their right sides post HA-IR820 administration. C) Graphical and D) Tabular AUC values for each MW HA-IR820 conjugate for drainage into the axillary lymph node package after an s.c. injection into the forearm. (AU ≡ Arbitrary Units)

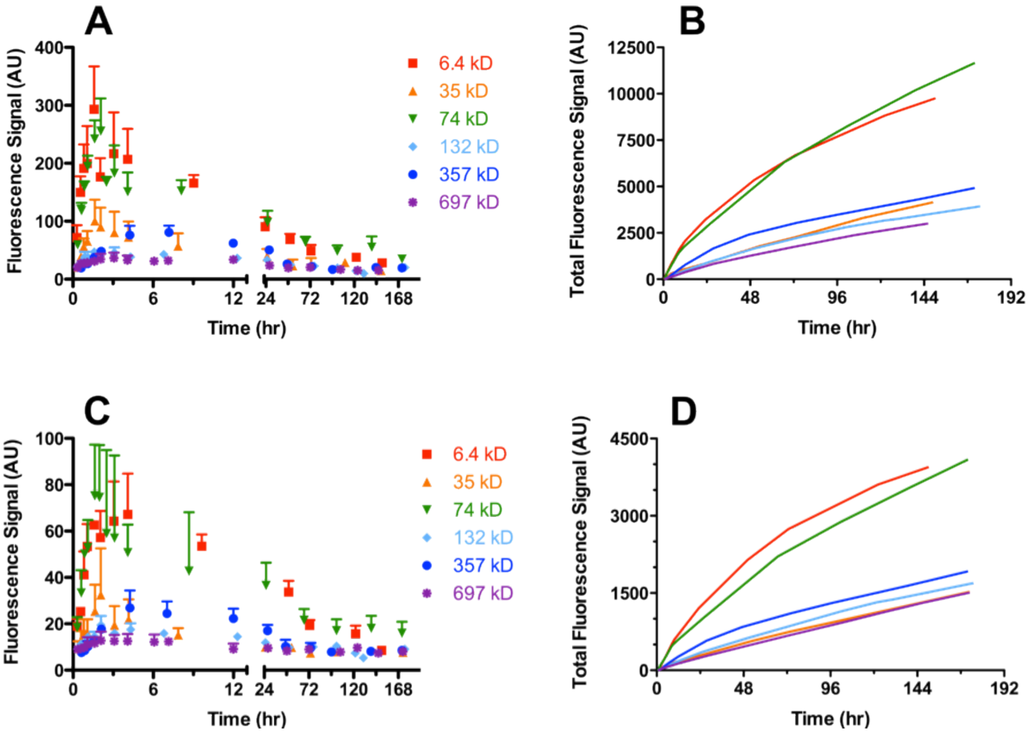

E

HA MW (kD)	Popliteal AUC (AU)	Iliac AUC (AU)
6.4	9734 ± 1821	3860 ± 466
35	3968 ± 1512	1019 ± 425
74	11464 ± 1916	4173 ± 1071
132	3589 ± 507	1505 ± 207
357	4887 ± 385	1901 ± 282
697	2867 ± 469	1088 ± 375

Figure 2.6. Lymphatic drainage to the popliteal (A, B) and iliac (C, D) lymph nodes of different MW (6.4 kD-red squares; 35 kD-orange triangles; 74 kD-green inverted triangles; 132 kD-light blue diamonds; 357 kD-blue circles; 697 kD-purple stars) HA-IR820 conjugates after s.c. injection. Increased lymphatic uptake of the 74kD HA-IR820 conjugate into the popliteal and iliac lymph nodes is evident in the A) time vs. fluorescent signal for the popliteal node, cumulative fluorescence signals in the B) time vs. total fluorescence signal for the popliteal node, C) time vs. fluorescent signal for the iliac node, and cumulative fluorescence signals in the D) time vs. total fluorescence signal for the iliac node graphs. The MW distribution trends shown are representative of the trends seen after imaging mice on their right sides post HA-IR820 administration. E) Tabular AUC values for each MW HA-IR820 conjugate for drainage into the popliteal and iliac lymph nodes after an s.c. injection into the forearm.

2.4 Discussion

2.4.1 In Vivo Imaging with HA-Texas Red

Conjugation of Texas Red to HA easily executed with using both EDAC and CMPI as activating agents. The use of CMPI yielded higher loading degrees than activation using EDAC, with 4% vs. 2% Texas Red loading on HA. In the initial imaging study investigating the lymphatic drainage of the HA-Texas red conjugate in tumor bearing mouse, the addition of a large hydrophobic fluorescent dye did not impede the lymphatic drainage of the s.c. injected HA conjugate into the tumor lymphatic basin. However, the signal to noise ratio of the HA-Texas Red conjugate *in vivo* could be improved by the use of a NIR dye, where the autofluorescence of the animal's skin and organs is minimized (preferably wavelengths >800 nm). In order to achieve deeper tissue penetration and increased signal to noise ratios of the fluorescent dye-HA conjugates, we chose to develop a HA-NIR dye conjugate utilizing an inexpensive NIR laser dye, IR820 for further optimization of the use of HA as a lymphatic carrier.

2.4.2 Characterization of HA

2.4.2.1 HA Polydispersities

In order to prevent significant overlap in the size of the HA polymers for the determination of the optimal MW for lymphatic uptake, we selectively chose HA samples with corresponding MWs falling within 10-100 nm range size by doubling the size with each increase in MW, thus allowing for the study of a wide variety of sizes. Once concern with using biopolymers, especially with HA, is their inherent polydisperse nature. The MW and polydispersities of the HAs purchased from Lifecore Biomedical were determined by multi-angle laser light scattering (MALLS) for the low MW HA polymers (≤ 357 kD), whereas intrinsic viscosity was used for MW determination of high MW HA polymers (≥ 697 kD) preventing their polydispersity index (PDI) determination. The manufacturer reported polydispersities are listed in Table 2.4. The PDI of the lower MW HAs (6.4 kD – 74 kD) are relatively narrow distributions for biopolymers, where the PDIs for the larger MW HAs (132 kD – 697 kD) are moderately dispersed.

MW (kD)	PDI (M_w/M_n)
6.4	1.075 ± 0.018
35	1.295 ± 0.004
74	1.293 ± 0.007
132	1.598 ± 0.012
357	1.663 ± 0.008
697	------

Table 2.4. Reported Polydispersity Indexes (PDI) from the HA manufacturer (Lifecore Biomedical). MW and PDIs were determined using MALLS for low MW HA, where the MW for high MW HA was determined by intrinsic viscosity, resulting in no PDI value.

2.4.2.2 Zeta Potential of HA

The zeta potentials of the HA samples were determined at pH >> pK_a, to ensure that all of the carboxylic acid functional groups were fully ionized to minimize effects of pH changes on the measurements due to partial protonation of the carboxylic acids. Partial protonation would lead to minor changes in the pH, and a reduction in the double layer thickness leading to zeta potentials of lower magnitude than for fully ionized polymers. Further, the pH studied would be indicative of the ionization state *in vivo*, thus a leading to biologically relevant zeta potentials for HA. There is no clear trend between the MW of HA and the zeta potential (Table 2.5). It would be expected that the zeta potential would remain constant over the entire MW range, or the magnitude of the zeta potential would become larger as the MW was increased. The expectation of a constant zeta potential is due to the fact that the number of carboxylic acids per disaccharide remains constant as the MW is increased, leading to the assumption of a constant zeta potential for all HA MWs. Further, for a linear decrease in the zeta potential with increasing HA MW would be a result of a proportional increase of the number of carboxylic acids with increasing polymer length. However, neither trend is evident in the HA samples. One possible explanation of the variation in the zeta potential is that for HA, it may indicate the stability of the polymer rather than the extent of negative charge on the polymer chain or a measure of anionic nature, as the number of carboxylic acid groups is proportional to the increase in HA MW.

In general a zeta potential of ± 30 mV is the cutoff for indicating the stability of a particle. If the $-30 <$ zeta potential <30, then it is thought that the particles are regarded as unstable or have the propensity to aggregate. Whereas if the zeta potential is above 30 or below -30, then the particles in solution are considered to be a stable suspension and are unlikely to form aggregates. As the MW of HA is increased in low ionic strength solutions pH 3-9, HA forms an extensively stable entangled network that is stabilized by hydrogen bonds and other non-covalent interactions even at low concentrations <1 μg/mL. Further, the longer the HA chain, the entangled network becomes more consistent and extensive. It has been reported that HA polymers of less than 7 disaccharides do not self-associate, 7-20 disaccharides (~2800-8000 Da) in length form monomer or dimers, and fragments of greater than 35 disaccharides (>14 kDa) can form intermolecular "hairpins"; and polymers of at least 60 disaccharides (~24 kDa) form stiffened segments [39]. These self-associations with HA polymer fragments are dependent on concentration, pH, ionic strength, and counterions. Dilute solutions of HA can aggregate in NaCl and $CaCl_2$; however, it does not do so in KCl.

As this study was conducted at a relatively high concentration (100 μg/mL), low ionic strength (1 mM), and in the presence of K^+ ions, it is likely that aggregates are not being formed at any MW. It is likely that the dramatic jump in the zeta potential is due to the formation of the stable stiffened sections along the HA polymer along with the formation of a stable interconnected long range network, which is reflected by the jump in the magnitude of the zeta potential as the MW is increased, suggesting a stable HA network in solution.

2.4.3 Characterization of HA-IR820

The conjugation efficiency of IR820 to HA is approximately 30%. This low efficiency could be in part due to the dialysis purification of HA-IR820 against water. The initial dye loading degree could be higher than the ca. 5% determined by NMR, however, a significant amount of dye could be lost due to hydrolysis of the ester bond between carboxyl group on the IR820 linker and the alcohol group on HA during the dialysis purification against water. Two possible ways to circumvent this possible loss in efficiency is by purification with a centrifugal filter device, or utilizing an amide bond between an amino terminated linker on IR820 with the carboxylic acid on HA.

Linear polymers, PEG and HA, of the same given molecular weight, can exhibit dramatically different solution characteristics. One example is HA has a larger excluded volume than that of PEG, as displayed by the shorter SEC retention time of HA. This is likely due to the conformation of the polymers in solution, where HA resides in an stiffened random coil with extensive intermolecular hydrogen bonding whose size is dependant on the solution water content, pH, ionic strength and composition [32,39]. Where PEG forms a more compact coiled-coil conformation that presents moderate swelling with the unique packing of water molecules within the coiled-coil [40]. The MW of the conjugates were similar or slightly lower to that of the original HA used, with the exception of the highest MW of 697-kD, which exhibited a significantly lower MW than that of the original HA (Figure 2.2). This is possibly due to the nature of the conjugation reaction between HA and IR820 as EDAC is commonly used as a HA crosslinking agent [35,41], in which it is possible for intramolecular cross linking between the carboxylic acid and alcohol groups on HA, thus leading to a lower apparent MW. The intramolecular crosslinking is likely more evident with the 697-kD conjugate due to the increased equivalents of EDAC and extended reaction time used in the conjugation reaction. With the 35-kD to 357-kD conjugates, there is some decrease in the apparent MW, as seen in the SEC longer retention times, compared to the original HA, but the change is minimal compared to that of the highest MW conjugate.

2.4.4 In Vivo Fluorescence Imaging Optimization and Data Analysis

Selective targeting of the sentinel lymph node is possible by s.c. injections into different anatomical regions in rodents [42]. The drainage pattern for a s.c. injection into the hind footpad results in drainage to the popliteal lymph node through the efferent popliteal trunk to iliac node. Likewise, the drainage pattern for a s.c. injection into the front forearm results in drainage to the axillary lymph node package. Because melanoma and breast cancer metastasize primarily via the lymphatics [2,43], identification of the sentinel lymph node is crucial staging and treatment of the disease. Drainage to the popliteal and axillary lymph nodes in rodents would serve as model for the SLN involved in melanoma and breast cancer. For localized limb melanoma in humans, the axillary nodal package is the SLN for the arms, while the popliteal or inguinal lymph nodes of the groin (popliteal and iliac are the corresponding nodes in rodents) are the sentinel lymph nodes for the legs [38]. Furthermore, the axillary lymph node package is the SLN in breast cancer [44,45]. Modeling the SLN drainage kinetics to the popliteal or axillary nodes instrumental in the development of lymphatically targeted carriers for imaging and drug delivery.

For the imaging studies, mice were injected with HA-IR820 on a dye basis, due to the different loading degrees of IR820 on HA. Failure to do so would have lead to artificial differences in the uptake due to differing concentrations of the fluorophore. Although the dye concentration was held constant, slight variations in the fluorescence intensities were observed. In order to normalize the imaging data for the slight variations, the total integrated fluorescence emission was determined using the *in vivo* imaging excitation and emission parameters (λ_{ex}= 700 nm, λ_{em}=800-900 nm) for each conjugate (0.1 mg/mL). The emission wavelengths of 800-900 nm were used due to the limitations of the spectrofluorometer, where the *in vivo* imager recorded the emission from 800 to 950 nm. After the fluorescence signal intensities were determined from the ROI placed over the lymph nodes, the intensities were normalized to the corresponding integrated fluorescence emission ratios. The MW distribution patterns for the lymphatic uptake remained unchanged after normalization.

2.4.5 In Vivo Imaging Control Experiments

After s.c. injection of the free dye, drainage via the lymphatic and vascular routes were observed using *in vivo* imaging. In contrast, the HA-IR820 conjugates exhibited only lymphatic drainage. This indicates that the free dye can diffuse into blood capillaries whereas HA is excluded from hematological uptake within the tissues. More than 75% of the free dye cleared from the lymph nodes within 20 hrs post injection, and it was completely cleared within 48 hrs. Similarly, in a study evaluating the lymphatic drainage of free indocyanine green (ICG) and ICG encapsulated liposomes (LP-ICG), both the ICG and LP-ICG cleared within 48 hr post injection [46]. Lymphatic imaging dyes such as isosulfan blue drains rapidly from the injection site, with 34%, 69%, and 100% absorption at 30 min, 1 hr, and 24 hr post s.c. injection [47]. IR820 has some lipid solubility and may accumulate in lipid membranes. It also may form conjugates with intracellular proteins that retain it.

After injection of the HA-IR820 conjugates, free dye was detected in the liver and not the lymph nodes. This suggests that the IR820 is not released until the conjugate progresses through the lymphatics and into the systemic circulation, where it is cleared and degraded by the liver [24]. However, it cannot be disregarded that the IR820 could release before emptying into the circulation but after the draining to the first two lymph nodes, due to the depth limitations of fluorescence imaging (ca. 1 cm) further lymph drainage to the echelon nodes cannot be detected with live animals. The intact HA-IR820 was also detected in the liver 4 to 8 h after administration; however, the fluorescence signal intensity was weak compared to that of the free dye.

2.4.6 Molecular Weight Dependence on Lymphatic Uptake

Although both 6.4-kD and 74-kD HA-IR820 had similar lymphatic uptake in all three lymph nodes studied, 74-kD HA-IR820 was chosen as the optimal MW. Low molecular weight HA (ca. 1-kDa to 10-kDa) stimulates angiogenesis [48] and inflammation [18,49], so there may be a different underlying mechanism for uptake of low molecular weight HA leading to the unexpectedly large AUC of 6.4-kD HA-IR820. Further investigation into the increased uptake of low molecular weight HA compared to larger HA is underway. It is worth noting, that no signs of toxicity were observed in any of the experimental groups (free dye and all HA-IR820 conjugates) for the entire length of the study (one week for the footpad group, and two weeks for the forearm group). The reported optimal liposomal size for lymphatic uptake after subcutaneous injection is 40 nm [50], which correlates well with our observation that 74-kD HA-IR820 is optimal for lymphatic uptake (30-50 nm in diameter, based on calculated R_g and R_h values, see Table 2.1).

A similar effect of molecular weight on lymphatic uptake has been observed with proteins; as the MW of s.c. injected proteins increases, the percent recovered dose also increases and approaches a plateau at 84-kD. There was a linear correlation with percent recovered to protein molecular weight up to 30-kD (83.9 % ± 3.3 %), which eventually approached 100% with an 84-kD protein (96.9 % ± 6.6 %) [51,52]. However, molecular weight was not the only factor governing the lymphatic uptake in the protein studies, as the charge of the different proteins also varied but was not considered in their analysis. With the various proteins reported in the studies, as increase the protein MW increases, the overall size doesn't differ dramatically, as they are all relatively small (< 10 -15 nm); however, with HA, as MW increases, the size also increases. The minimal changes in size of the proteins are due to the compact nature of globular proteins, whereas the large hydrated volume of HA in solution and its random coiled structure are ascribed to its large hydrodynamic volume. Ogston and Stainer best describe HA as it "behaves hydrodyamically like a large solvated sphere containing a thousand times more water than organic material [39]." Reddy et al. demonstrated that 71-kD FITC-labeled dextran has a faster solute velocity within the interstitium compared to a 3-kD, 40-kD, and 2-MD dextran-FITCs or 69-kD bovine serum albumin [53]. This agrees with our observation that the 74-kD HA has the greatest lymphatic uptake within the study's timeframe.

2.5 Conclusions

We optimized the molecular weight of HA for use as a multimodal carrier for lymphatic imaging and drug delivery, using a NIR-dye-HA conjugate with *in vivo* fluorescence imaging. Hyaluronan with a molecular weight of 74-kD was determined to be optimal for lymphatic imaging, due to its maximal lymphatic uptake and enhanced lymph node retention. This corresponds to a calculated size of ca. 30 to 50 nm, which is consistent with the reported optimal size of liposomes for lymphatic uptake [50]. Previous studies which optimized the particulate size for enhanced lymphatic uptake have focused either on several small dendrimers between 5 and 20 nm in size, which are near the point of capillary uptake [54,55], or two to three different liposomes or nanoparticles with differing compositions over an extremely wide size range (100-150 nm spread) [5,50]. In addition, the differently sized particles often have very different overall charges or hydrophobicities, such as different proteins. These new variables further complicate the investigation of the effect of size on lymphatic uptake. We utilized a single polymer, HA, so the resulting differences in the uptake kinetics were independent of charge or hydrophobicity. Since HA is a linear polymer, the molecular weight was directly proportional to the number of surface carboxylic acid groups, whereas with dendrimers, the number of surface groups increases exponentially with molecular weight and the exposure of the more hydrophobic core can change with size.

Hyaluronan is more favorable for clinical imaging than non-biodegradable imaging agents, such as PAMAM dendrimers and QDs, and no toxicities were observed over several weeks in these studies. Agents such as QDs must be limited to 5 nm or less in size for renal clearance, but still are susceptible to long bioretention and heavy metal leakage. In addition, most dendrimers currently under investigation contain multiple amino groups that have to be further functionalized with PEG or anionic or neutral ligands to reduce their cationic nature and minimize their toxicity [56].

Hyaluronan holds great promise as a natural biopolymer for drug delivery and lymphatic imaging. It is non-immunogenic, non-toxic, and it naturally degrades within the lymphatics, unlike most other drug delivery platforms. We have shown that the retention of HA can be tailored from periods of hours to days within the nodal tissues, making it suitable for both sustained drug delivery and long-term imaging of the lymphoid tissues.

One issue that has arisen in the development HA dye and chemotherapeutic conjugates, is that HA is extremely viscous thus limiting the MW < 74-kD (optimal MW) and dilute solutions, leading to large injection volumes in order to achieve therapeutic doses. Further, the loading degree is also limited due to the possible alterations in its biocompatibility and solubility. In order to overcome these challenges, we developed a new biodegradable star polymer with variable anionic charge as a new lymphatic delivery vehicle. The effect of the degree of negative charge on the lymphatic uptake utilizing the same techniques presented in this chapter with the use of the IR820 NIR dye and whole body fluorescence imaging is discussed in Chapter 3. The size optimization of the conjugate lays the foundation for further investigation into the effect of negative charge on the lymphatic uptake of star polymers (Chapter 3) and the differences in the drainage kinetics of HA in a murine melanoma tumor model (Chapter 4).

2.6 References

1. Landry, C.S.; McMasters, K.M.; Scoggins, C.R., The evolution of the management of regional lymph nodes in melanoma. *J Surg Oncol* **2007**, *96*, 316-321.

2. Hellman, S.; Harris, J.R., The appropriate breast cancer paradigm. *Cancer Res* **1987**, *47*, 339-342.

3. Eccles, S.A.; Welch, D.R., Metastasis: Recent discoveries and novel treatment strategies. *Lancet* **2007**, *369*, 1742-1757.

4. Porter, C.J., Drug delivery to the lymphatic system. *Crit Rev Ther Drug Carrier Syst* **1997**, *14*, 333-393.

5. Rao, D.A.; Forrest, M.L.; Alani, A.W.; Kwon, G.S.; Robinson, J.R., Biodegradable plga based nanoparticles for sustained regional lymphatic drug delivery. *J Pharm Sci* **2010**, *99*, 2018-2031.

6. O'Driscoll, C.M., Anatomy and physiology of the lymphatics. In *Lymphatic transport of drugs*, Charman, W.N.; Stella, V.J., Eds. CRC Press: Boca Raton, 1992; pp 1-35.

7. Casley-Smith, J.R., The fine structure and functioning of tissue channels and lymphatics. *Lymphology* **1980**, *13*, 177-183.

8. Oussoren, C.; Storm, G., Liposomes to target the lymphatics by subcutaneous administration. *Adv Drug Deliv Rev* **2001**, *50*, 143-156.

9. Patel, H.M., Fate of liposomes in the lymphatics. In *Liposomes as drug carriers*, Gregoriadis, G., Ed. John Wiley and Sons: New York, 1988; p 51.

10. Kaminskas, L.M.; Porter, C.J., Targeting the lymphatics using dendritic polymers (dendrimers). *Adv Drug Deliv Rev* **2011**, *63*, 890-900.

11. Patel, H.M.; Boodle, K.M.; Vaughan-Jones, R., Assessment of the potential uses of liposomes for lymphoscintigraphy and lymphatic drug delivery. Failure of 99m-technetium marker to represent intact liposomes in lymph nodes. *Biochim Biophys Acta* **1984**, *801*, 76-86.

12. Hilderbrand, S.A.; Weissleder, R., Near-infrared fluorescence: Application to in vivo molecular imaging. *Curr Opin Chem Biol* **2010**, *14*, 71-79.

13. Kobayashi, H.; Koyama, Y.; Barrett, T.; Hama, Y.; Regino, C.A.; Shin, I.S.; Jang, B.S.; Le, N.; Paik, C.H.; Choyke, P.L*., et al.*, Multimodal nanoprobes for radionuclide and five-color near-infrared optical lymphatic imaging. *ACS Nano* **2007**, *1*, 258-264.

14. Lin, P.; Chen, J.W.; Chang, L.W.; Wu, J.P.; Redding, L.; Chang, H.; Yeh, T.K.; Yang, C.S.; Tsai, M.H.; Wang, H.J., *et al.*, Computational and ultrastructural toxicology of a nanoparticle, quantum dot 705, in mice. *Environ Sci Technol* **2008**, *42*, 6264-6270.

15. Ballou, B.; Lagerholm, B.C.; Ernst, L.A.; Bruchez, M.P.; Waggoner, A.S., Noninvasive imaging of quantum dots in mice. *Bioconjug Chem* **2004**, *15*, 79-86.

16. Choi, H.S.; Liu, W.; Misra, P.; Tanaka, E.; Zimmer, J.P.; Itty Ipe, B.; Bawendi, M.G.; Frangioni, J.V., Renal clearance of quantum dots. *Nat Biotechnol* **2007**, *25*, 1165-1170.

17. Matou-Nasri, S.; Gaffney, J.; Kumar, S.; Slevin, M., Oligosaccharides of hyaluronan induce angiogenesis through distinct cd44 and rhamm-mediated signalling pathways involving Cdc2 and gamma-adducin. *Int J Oncol* **2009**, *35*, 761-773.

18. Wolny, P.M.; Banerji, S.; Gounou, C.; Brisson, A.R.; Day, A.J.; Jackson, D.G.; Richter, R.P., Analysis of CD44-hyaluronan interactions in an artificial membrane system: Insights into the distinct binding properties of high and low molecular weight hyaluronan. *J Biol Chem* **2010**, *285*, 30170-30180.

19. Ossipov, D.A., Nanostructured hyaluronic acid-based materials for active delivery to cancer. *Expert Opin Drug Deliv* **2010**, *7*, 681-703.

20. Luo, Y.; Ziebell, M.R.; Prestwich, G.D., A hyaluronic acid-taxol antitumor bioconjugate targeted to cancer cells. *Biomacromolecules* **2000**, *1*, 208-218.

21. Liu, N.F., Trafficking of hyaluronan in the interstitium and its possible implications. *Lymphology* **2004**, *37*, 6-14.

22. Rossler, A.; Fink, M.; Goswami, N.; Batzel, J.J., Modeling of hyaluronan clearance with application to estimation of lymph flow. *Physiol Meas* **2011**, *32*, 1213-1238.

23. Knudson, W.; Peterson, R.S., The hyaluronan receptor: CD44. In *Chemistry and biology of hyaluronan*, 1st ed.; Garg, H.G.; Hales, C.A., Eds. Elsevier: Amsterdam ; Boston, 2004; pp 83-123.

24. Platt, V.M.; Szoka, F.C., Jr., Anticancer therapeutics: Targeting macromolecules and nanocarriers to hyaluronan or CD44, a hyaluronan receptor. *Mol Pharm* **2008**, *5*, 474-486.

25. Gaffney, J.; Matou-Nasri, S.; Grau-Olivares, M.; Slevin, M., Therapeutic applications of hyaluronan. *Mol Biosyst* **2010**, *6*, 437-443.

26. Cai, S.; Xie, Y.; Davies, N.M.; Cohen, M.S.; Forrest, M.L., Pharmacokinetics and disposition of a localized lymphatic polymeric hyaluronan conjugate of cisplatin in rodents. *J Pharm Sci* **2010**, *99*, 2664-2671.

27. Cai, S.; Xie, Y.; Davies, N.M.; Cohen, M.S.; Forrest, M.L., Carrier-based intralymphatic cisplatin chemotherapy for the treatment of metastatic squamous cell carcinoma of the head & neck. *Ther Deliv 1*, 237-245.

28. Cai, S.; Thati, S.; Bagby, T.R.; Diab, H.M.; Davies, N.M.; Cohen, M.S.; Forrest, M.L., Localized doxorubicin chemotherapy with a biopolymeric nanocarrier improves survival and reduces toxicity in xenografts of human breast cancer. *J Control Release* **2010**, *146*, 212-218.

29. Cai, S.; Xie, Y.; Bagby, T.R.; Cohen, M.S.; Forrest, M.L., Intralymphatic chemotherapy using a hyaluronan-cisplatin conjugate. *J Surg Res* **2008**, *147*, 247-252.

30. Cohen, M.S.; Cai, S.; Xie, Y.; Forrest, M.L., A novel intralymphatic nanocarrier delivery system for cisplatin therapy in breast cancer with improved tumor efficacy and lower systemic toxicity in vivo. *Am J Surg* **2009**, *198*, 781-786.

31. Xie, Y.; Aillon, K.L.; Cai, S.; Christian, J.M.; Davies, N.M.; Berkland, C.J.; Forrest, M.L., Pulmonary delivery of cisplatin-hyaluronan conjugates via endotracheal instillation for the treatment of lung cancer. *Int J Pharm* **2010**, *392*, 156-163.

32. Takahashi, R.; Kubota, K.; Kawada, M.; Okamoto, A., Effect of molecular weight distribution on the solution properties of sodium hyaluronate in 0.2m nacl solution. *Biopolymers* **1999**, *50*, 87-98.

33. Gajewiak, J.; Cai, S.; Shu, X.Z.; Prestwich, G.D., Aminooxy pluronics: Synthesis and preparation of glycosaminoglycan adducts. *Biomacromolecules* **2006**, *7*, 1781-1789.

34. Shibanuma, T.; Shiono, M.; Mukaiyama, T., A convenient method for the preparation of carbodiiimides using 2-chloropyridinium salt. *Chemistry Letters* **1977**, *6*, 575-576.

35. Young, J.J.; Cheng, K.M.; Tsou, T.L.; Liu, H.W.; Wang, H.J., Preparation of cross-linked hyaluronic acid film using 2-chloro-1-methylpyridinium iodide or water-soluble 1-ethyl-(3,3-dimethylaminopropyl)carbodiimide. *J Biomater Sci Polym Ed* **2004**, *15*, 767-780.

36. Masotti, A.; Vicennati, P.; Boschi, F.; Calderan, L.; Sbarbati, A.; Ortaggi, G., A novel near-infrared indocyanine dye-polyethylenimine conjugate allows DNA delivery imaging in vivo. *Bioconjug Chem* **2008**, *19*, 983-987.

37. Ruddell, A.; Harrell, M.I.; Minoshima, S.; Maravilla, K.R.; Iritani, B.M.; White, S.W.; Partridge, S.C., Dynamic contrast-enhanced magnetic resonance imaging of tumor-induced lymph flow. *Neoplasia* **2008**, *10*, 706-713, 701 p following 713.

38. Uren, R.F.; Howman-Giles, R.; Thompson, J.F., Patterns of lymphatic drainage from the skin in patients with melanoma. *J Nucl Med* **2003**, *44*, 570-582.

39. Lapcik, L.J.; Lapcik, L.; De Smedt, S.; Demeester, J.; Chabrecek, P., Hyaluronan: Preparation, structure, properties, and applications. *Chem Rev* **1998**, *98*, 2663-2684.

40. Devanand, K.; Selser, J.C., Asymptotic behavior and long-range interactions in aqueous solutions of poly(ethylene oxide). *Macromolecules* **1991**, *24*, 5943-5947.

41. Birkinshaw, C.; Collins, M.N., Comparison of the effectiveness of four different crosslinking agents with hyaluronic acid hydrogel films for tisslue-culture applications. *J Appl Polym Sci* **2007**, *104*, 3183-3191.

42. Tilney, N.L., Patterns of lymphatic drainage in the adult laboratory rat. *J Anat* **1971**, *109*, 369-383.

43. Nathanson, S.D., Insights into the mechanisms of lymph node metastasis. *Cancer* **2003**, *98*, 413-423.

44. Hindie, E.; Groheux, D.; Brenot-Rossi, I.; Rubello, D.; Moretti, J.L.; Espie, M., The sentinel node procedure in breast cancer: Nuclear medicine as the starting point. *J Nucl Med* **2011**, *52*, 405-414.

45. Shimazu, K.; Noguchi, S., Sentinel lymph node biopsy before versus after neoadjuvant chemotherapy for breast cancer. *Surg Today* **2011**, *41*, 311-316.

46. Proulx, S.T.; Luciani, P.; Derzsi, S.; Rinderknecht, M.; Mumprecht, V.; Leroux, J.C.; Detmar, M., Quantitative imaging of lymphatic function with liposomal indocyanine green. *Cancer Res* **2010**, *70*, 7053-7062.

47. Lymphazurin (isosulfan blue) information from drugs.com. http://www.drugs.com/pro/lymphazurin.html (September 4, 2011),

48. West, D.C.; Hampson, I.N.; Arnold, F.; Kumar, S., Angiogenesis induced by degradation products of hyaluronic acid. *Science* **1985**, *228*, 1324-1326.

49. Bot, P.T.; Pasterkamp, G.; Goumans, M.J.; Strijder, C.; Moll, F.L.; de Vries, J.P.; Pals, S.T.; de Kleijn, D.P.; Piek, J.J.; Hoefer, I.E., Hyaluronic acid metabolism is increased in unstable plaques. *Eur J Clin Invest* **2010**, *40*, 818-827.

50. Oussoren, C.; Zuidema, J.; Crommelin, D.J.; Storm, G., Lymphatic uptake and biodistribution of liposomes after subcutaneous injection. Ii. Influence of liposomal size, lipid compostion and lipid dose. *Biochim Biophys Acta* **1997**, *1328*, 261-272.

51. McLennan, D.N.; Porter, C.J.H.; Charman, S.A., Subcutaneous drug delivery and the role of the lymphatics. *Drug Discov Today: Technol* **2005**, *2*, 89-96.

52. McLennan, D.N.; Porter, C.J.; Edwards, G.A.; Martin, S.W.; Charman, S.A., Molecular weight is a primary determinant for lymphatic absorption of proteins following subcutaneous administration to sheep. *AAPS PharmSci* **2002**, *4*.

53. Reddy, S.T.; Berk, D.A.; Jain, R.K.; Swartz, M.A., A sensitive in vivo model for quantifying interstitial convective transport of injected macromolecules and nanoparticles. *J Appl Physiol* **2006**, *101*, 1162-1169.

54. Kobayashi, H.; Kawamoto, S.; Bernardo, M.; Brechbiel, M.W.; Knopp, M.V.; Choyke, P.L., Delivery of gadolinium-labeled nanoparticles to the sentinel lymph node: Comparison of the sentinel node visualization and estimations of intra-nodal gadolinium concentration by the magnetic resonance imaging. *J Control Release* **2006**, *111*, 343-351.

55. Kaminskas, L.M.; Kota, J.; McLeod, V.M.; Kelly, B.D.; Karellas, P.; Porter, C.J., Pegylation of polylysine dendrimers improves absorption and lymphatic targeting following sc administration in rats. *J Control Release* **2009**, *140*, 108-116.

56. Wijagkanalan, W.; Kawakami, S.; Hashida, M., Designing dendrimers for drug delivery and imaging: Pharmacokinetic considerations. *Pharm Res* **2011**, *28*, 1500-1519.

Chapter 3. Development and Optimization of Polyanionic Star Polymer-Fluorescent Dye Conjugates for Intralymphatic Delivery Using *in vivo* Fluorescence Imaging

3.1 Introduction

In addition to the effects of size on lymphatic uptake that we investigated in the previous chapter, the charge, hydrophobicity, injection site, and dose also play an important role [1-3]. A number of different delivery vehicles have been employed for lymphatic imaging and drug delivery, including: liposomes, dendrimers, quantum dots, synthetic polymers, and natural polymers. In Chapter 2, I discussed our previous studies using a natural biopolymer, hyaluronan (HA), for targeted lymphatic drug delivery [4-8] and its dependence on size for optimal lymphatic uptake and nodal retention. Using a series of HA-near infrared (NIR) fluorescent dye conjugates developed for *in vivo* fluorescence imaging, we determined that the optimal particulate size for lymphatic uptake was 30-50 nm.

Reports have demonstrated that negatively charged particles have increased lymphatic uptake compared to neutral to positively charged particles [9-11], in part due to the electrostatic repulsions between the negatively charged particles and the extracellular matrix [1], which is primarily negatively charged [1-3]. Also, negatively charged particles are retained longer by lymph nodes [1,10,12]. However, little research has been conducted into the extent of negative charge required for enhanced lymphatic uptake. To date, only one report on the effects of varying the degree of negative charge of particles on the lymphatic uptake, in which Rao and coworkers varied the ratio of carboxylic acid terminated poly(D,L-lactic-co-glycolic) with non-terminated PLGA to give nanoparticles with various degrees of anionic charge. The lymphatic uptake of the three of different negatively charged nanoparticles was investigated in rats after a subcutaneous (s.c.) injection into the hind footpad [1]. An increase in the negative charge of the nanoparticles resulted increased lymphatic uptake.

In this study, we sought to determine the optimal degree of anionic character needed for lymphatic uptake of a drug delivery system. However, additional surface modification to our previous lymphatic delivery platform HA was not a viable option as it is already highly charged. These high degrees of modification are synthetically difficult, may alter the solubility profile, or could change its biological behavior *in vivo*, such as loss of receptor recognition or initiation of immune responses, essentially defeating the purpose of using a biopolymer as the carrier. Liposomes and dendrimers are the most commonly used platforms for lymphatic delivery, both of which can be modified to have polyanionic surface charges. Dendrimers are appealing due to their low polydispersities, compact size (nm in size), multi-valent surface groups, and high water solubility. Dendrimers are more attractive, due to their compact structure which resembles globular structure of endogenous proteins, rather than linear polymers that form random coils in solution [13]. Further, dendrimers exhibit low solution viscosities [14]. However, issues with their clearance, toxicity, and biodegradability have limited the use of dendrimers as delivery vehicles. Polyamidoamine (PAMAM) and diaminobutane (DAB) dendrimers are the most commonly used dendrimers, in part due to their commercial availability, compact size, and the polyamido core assists in increasing the water solubility and reducing the immunogenicity [13]. Both PAMAM and DAB dendrimers are highly cationic; however, fictionalization of the terminal amino groups with neutral or negatively charged ligands, is desirable for optimizing the lymphatic uptake [15,16]. However, PAMAMs are not biodegradable, thus limiting the size for lymphatic drug delivery and imaging to particles less than 5 to 6 nm for renal clearance [17,18]. Particles of this size are not selective for lymphatic uptake, and can also be absorbed by the blood capillaries. Further, dendrimer based imaging agents optimized for lymphatic uptake and renal clearance, migrate readily through the lymphatics with little to no nodal retention, thus limiting their use as a localized sustained release drug delivery platform. In addition, high conjugation of hydrophobic chemotherapeutics and fluorescent dyes limits the dendrimer solubility. Although biodegradable dendrimers have been developed using amino acids as their building blocks, they are unlikely to exhibit significant accumulation, and the degradation products have shown toxicity [13]. There is a great need to develop biodegradable drug delivery system for lymphatic delivery that have both the optimal size and charge for enhanced lymphatic uptake.

For these reasons, we developed a new water soluble, degradable star polymer as a lymphatic delivery platform with various degrees of anionic charge. Star polymers are three-dimensional with linear polymeric arms emanating from a branched central core [19,20]. Like dendrimers, star polymers are branched polymers that have a compact structure, are globular in shape, and have large surface areas, which make them optimal platforms for lymphatic delivery. Further, hyperbranched polymers and multi-arm star polymers exhibit low intrinsic viscosities and increased solubilities compared to their linear counterparts [21,22]. Star polymers can be synthesized using a living radical polymerization techniques, including reversible addition-fragmentation chain transfer (RAFT) and macromolecular design via the interchange of xanthates (MADIX) with a broad range of reaction conditions and functional groups [23]. With the use of RAFT polymerization, it is possible to construct star polymers while accurately controlling the molecular weight [23,24], resulting in low polydispersities.

A series of 4-armed star-polymers with varying degrees of negative charge were developed for the investigation of the extent of anionic character required for optimal lymphatic uptake. A near infrared dye, IR820, was conjugated to the polymers to utilize the capabilities of whole body fluorescent imaging to detect the effects of negative charge on the lymphatic uptake of star polymers.

3.2 Experimental

3.2.1 Star Polymer Synthesis

A series of 4-arm star polymers with various degrees of anionic charge, were previously synthesized by Dr. Duan in our laboratory using the MADIX/RAFT polymerization method (macromolecular design by interchange of xanthates/reversible addition-fragmentation chain transfer). For the detailed synthetic procedure of the star polymer synthesis and the ^{1}H NMR assignments, see Appendix 1. Briefly, the synthetic procedure for the MADIX agent was the same as previously reported by Stenzel et al. [25]. The MADIX agent was formed by the addition of a xanthate group to pentaerythritol to form the 4-armed core for the star polymer (Scheme 3.1). The RAFT agent and the MADIX/RAFT polymerization were synthesized according to Ting et al [26]. Briefly, a 6-O-methacryloyl-D-galactose was used as the repeating unit in the polymerization reaction initiated by AIBN to give the sugar-star polymer (Scheme 3.2). After deprotection, the sugar-star polymer was conjugated with various amounts of succinic anhydride to vary the degree of anionic charge on the star polymer. Briefly, 20, 40, 60, and 90 wt% succinic anhydride was reacted with the sugar-star polymer in DMF/pyridine to yield the sugar-acid star polymers with 20, 40, 60, and 90 wt% acid (Scheme 3.3). All of the synthesized compounds were verified by ^{1}H-NMR.

The molecular weights and polydispersity index (PDI) of the protected (star poly-(1,2:3,4-*Di*-*O*-isopropylidene-6-*O*-methacryloyl-α-*D*-galactopyranose)) and deprotected (star poly-(6-*O*-methacryloyl-*D*-galactose)) sugar-star polymers were determined by size exclusion chromatography (SEC) (Shimadzu 2010CHT) using a TSK gel multipore Hx-M column coupled with a refractive index detector (Shimadzu RID-10A), and using 0.8 mL/min of DMF containing 10-mM LiCl as the mobile phase. Calibration curves were generated with polystyrene standards (1,180 to 339,500 g/mol) or polyethylene glycol (PEG) standards (3070 to 66,100 g/mol) for the protected and deprotected sugar-star polymers, respectively.

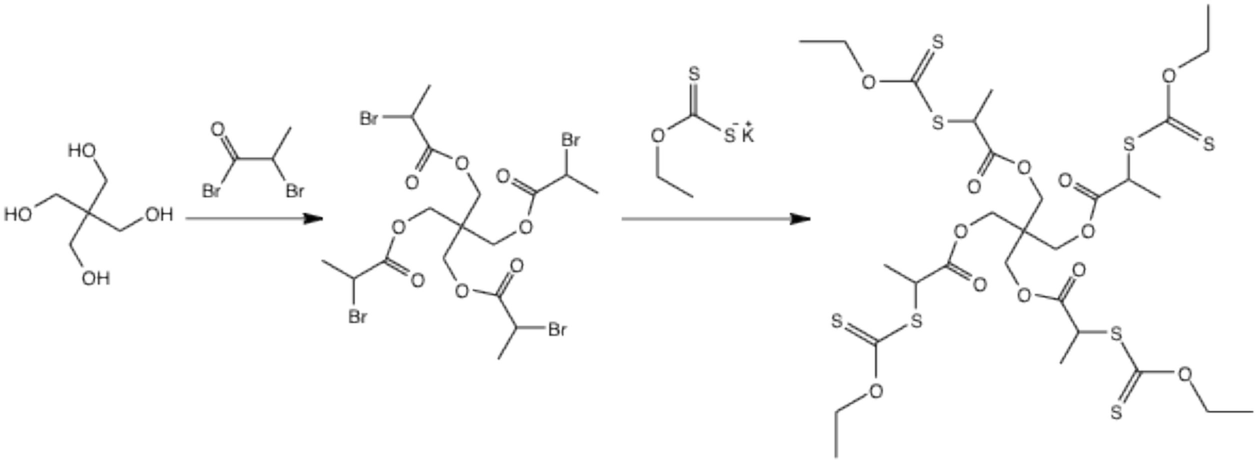

Scheme 3.1. Synthesis of a MADIX agent.

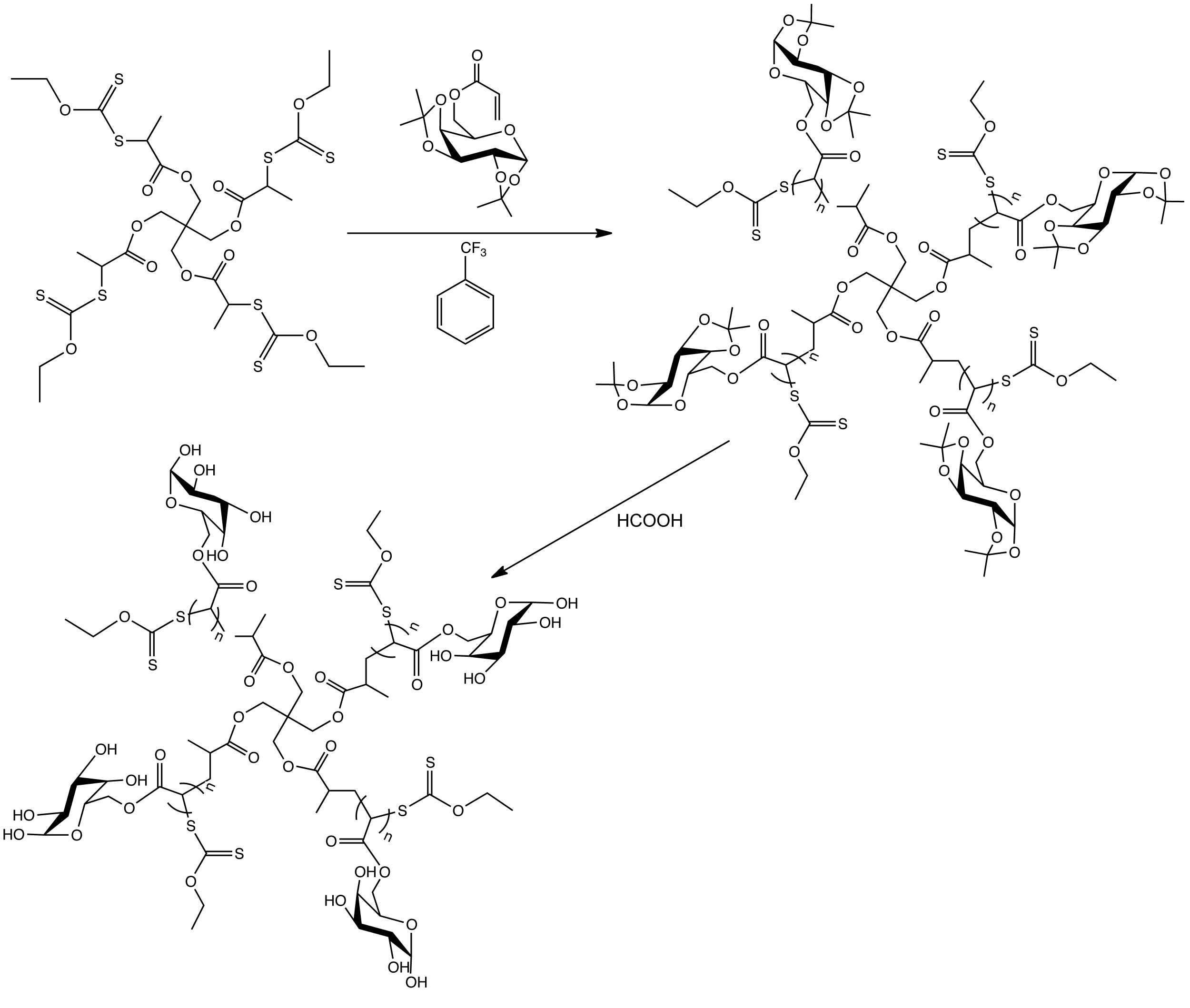

Scheme 3.2. Synthesis of the 4-arm sugar star polymers by MADIX/RAFT polymerization.

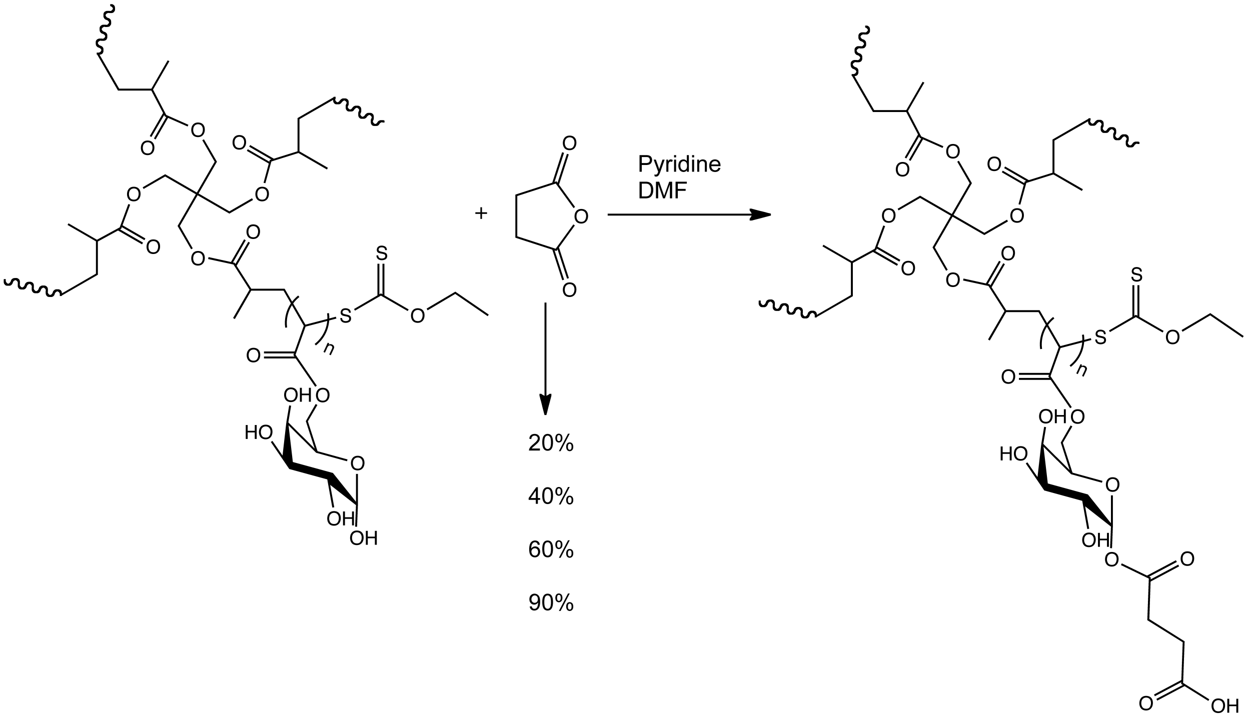

Scheme 3.3. Modification of the star poly-(6-*O*-methacryloyl-*D*-galactose) with succinic anhydride to give the 20, 40, 60, and 90% wt/wt star-polymer.

3.2.2 Star-IR820 Synthesis

To the series of various wt% acid star polymers synthesized in our laboratory, IR-820 was added to yield a series of star-IR820 conjugates with various degrees of anionic charge for *in vivo* imaging. First, to a solution of IR-820 (100 mg, 0.094 mmol) in 20 mL dry DMF, 1,3-diaminopropane (40 μL, 0.47 mmol) was added dropwise. The solution was gradually heated to 60 °C, and was allowed to react for four hours protected from light. The solvent was evaporated under reduced pressure followed purification by column chromatography (1:1 EtOAC:MeOH). The fractions were combined and the solvent was removed under reduced pressure, yielding a dark blue solid (65 mg, 78%) (Scheme 3.4). The 3-aminopropyl-amino-IR820 derivative was then conjugated to the sugar-acid star polymer in dry DMF with EDAC activation and $HOBt \cdot H_2O$ as the catalyst (Scheme 3.5). Briefly, to a cooled solution (0 °C) of the sugar-acid-star polymer (60% acid) (75 mg) in 20 mL dry DMF, then EDAC (28.1 mg, 0.147 mmol) and $HOBt \cdot H_2O$ (22.5 mg, 0.147 mmol) were added. After five minutes, the 3-aminopropyl-amino-IR820 derivative (65 mg, 0.073 mmol) in DMF (5 mL) was added dropwise. The reaction was allowed to proceed at ambient temperature overnight, protected from light. The resulting sugar-acid-star-polymer-IR820 (star-IR820) was purified by dialysis against $EtOH:H_2O$ (1:1) followed by 100% EtOH. The resulting series of acid-star-IR820 conjugates were bluish-purple in color, and the loading degree of IR820 on the star polymers was determined by ^1H NMR in MeOD. The 3-aminopropyl-amino-IR820 derivative conjugation reactions with the 20, 40, and 90% wt/wt acid-star polymers along with the ^1H NMR assignments can be found in Appendix 1.

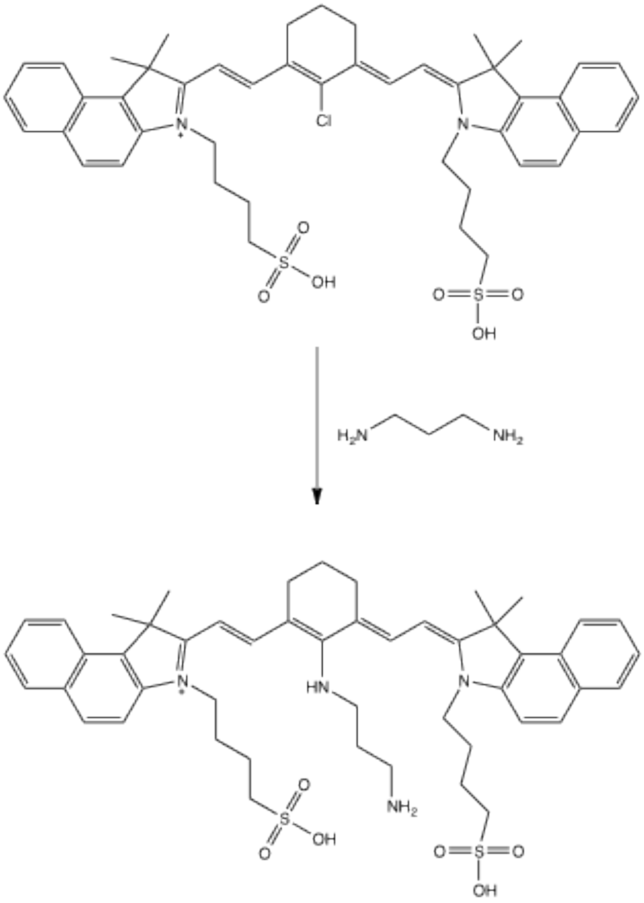

Scheme 3.4. Synthesis of the 3-aminopropyl-amino-IR820 derivative.

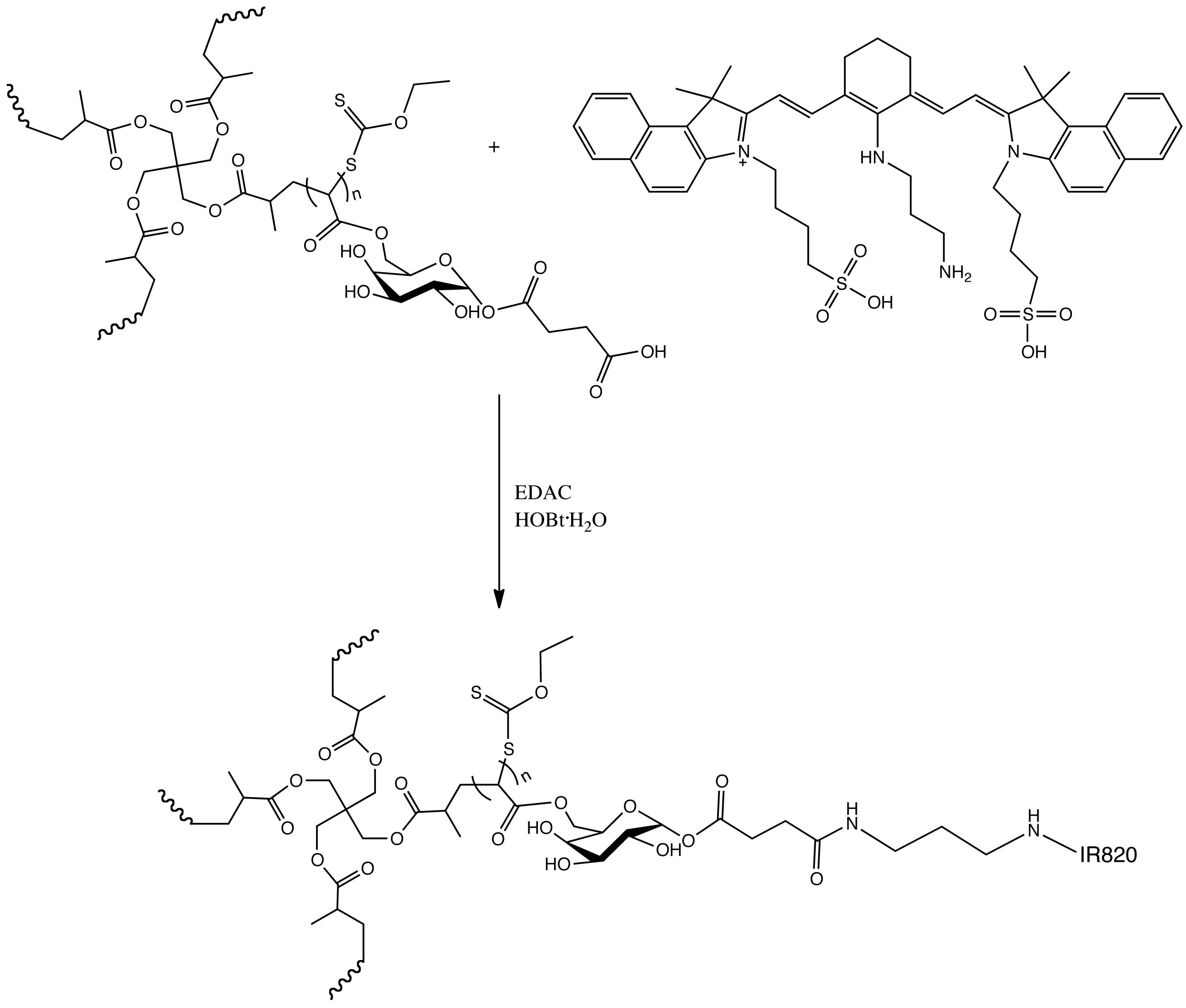

Scheme 3.5. Conjugation of 3-aminopropyl-amino-IR820 to a sugar-acid-star polymer to give the star-IR820 conjugate.

3.2.3 Rheological Properties

The viscosities of the different molecular weight HA samples used for lymphatic imaging in Chapter 2, along with the different acid star polymers were determined in PBS at pH 7.4. Sugar star polymer and sugar acid star polymer samples were dissolved in PBS (at ca.100 mg/mL conc.) and dialyzed against PBS (pH 7.4) for 48 hours at ambient temperature using a 3.5-kD MWCO dialysis tubing (regenerated cellulose, Fisherbrand) to adjust the pH. The HA samples were dissolved in PBS pH 7.4 and were used without any further adjustment in pH. The polymers (star and HA) were then diluted to 1, 5, and 10 mg/mL with PBS (pH 7.4). The rheological properties were measured in triplicate using an Advanced Rheometer 2000 (TA Instruments, New Castle, DE), at 25°C using a 40 mm 2° aluminum cone geometry and a 49 μm gap distance. The shear rate was increased using a steady state flow step, from 10 to 100 s^{-1} with 10 points per decade using a log scale and a sample period of 10 s. The steady state parameters were set to 5% deviation for three consecutive points within a maximum time of 1 minute per shear rate.

3.2.4 Zeta Potential of the Star Polymers

Sugar-star and sugar-acid-star polymer samples were dissolved in ddH_2O to a concentration of ca. 1 mg/mL, the pH was then adjusted to 7.2 ± 0.1 with sodium hydroxide, and the final concentration was noted. The samples were then diluted to 1, 10, and 100 μg/mL with pH 7.25 1-mM phosphate buffer with the addition of 1mM of KCl. After dilution, the pH was rechecked. Zeta potentials were measured on a ZetaPALS (Brookhaven Instruments Corporation, Holtsville, NY) at 20°C and the sample measurements were repeated six times.

3.2.5 In Vitro Toxicity of the Star Polymers

B16F10 (lymphatically metastatic murine melanoma, ATCC), MDA-MB-231 (human breast cancer), MDA-1986 (lymphatically metastatic human head and neck cancer), and HUVEC (normal human endothelial) cell lines, were maintained in Dulbecco's modified Eagle's medium (DMEM) supplemented with 1% L-Glutamine and 10% bovine growth serum in 5% CO_2 atmosphere. The HER2 expressing murine breast cancer cell line, 4T1.2 Neu, was a gift from Dr. Zhaoyang You, from the University of Pittsburg, and was maintained in DMEM supplemented with 1% L-Glutamine, 10 % bovine growth serum, and 500 μg/mL of G418 (geneticin) in 5% CO_2 atmosphere. The lymphatically metastatic human melanoma cell line, A2058, was purchased from ATCC, and was maintained in low sodium bicarbonate DMEM supplemented with 1% L-Glutamine, and 10% bovine growth serum in 5% CO_2 atmosphere.

The sugar-acid star polymer samples (20, 40, 60, and 90 wt% acid) were dialyzed against PBS (as described in rheometry section) for 48 hours to adjust the pH to 7.4. The solutions were concentrated to ca. 100 mg/mL using a Speedvac concentrator (Labconoco) and then diluted in sterile 1× PBS (Fisher BioReagents, pH 7.4) to eight concentrations between 10^{-4} to 10^{-9} M. Prior to cell growth inhibition studies, cells were trypsinized and seeded at 3000 cells/well 96-well tissue culture treated plates. After 24 hours, the 20%, 40%, 60%, and 90% acid-sugar star polymers in PBS were added to the HUVEC, A2058, and 4T1.2 Neu cells (n=8, 10 μL/well, 8 concentrations). Only the 60% acid-sugar star polymer sample was added to the B16F10, MDA-MB-231, and MDA-1986 cells 24 hours after seeding (n=8, 10 μL/well, 8 concentrations). A solution of 10% trichloracetic acid was used as a negative control, and media was used as a positive control (n=8, 10 μL/well). At 72 hours post addition, 10 μL of resazurin blue in PBS was added (5 μM final concentration) to each well and the well fluorescence was measured after

3 hours ($\lambda_{ex}/\lambda_{em}$ = 560/590 nm) (SpectraMax Gemini, Molecular Devices). IC_{50}s were determined using the nonlinear regression curve fit for a one-site competition (GraphPad Prism 10).

3.2.6 In Vivo Imaging of Star-IR820

In vivo imaging with the star-IR820 conjugates was performed as previously discussed for the HA-IR820 conjugates in the hind footpad. As in chapter 2, all mice were fed a low chlorophyll diet (Harlan 2918 irradiated diet) for at least one week prior to imaging to decrease food induced organ and skin autofluorescence. The mouse's hair in the area of interest for imaging was removed 24 hours prior to imaging with clippers followed by depilatory cream. Female Balb/c mice (20-25 g, Charles River) (3 per group) were anesthetized under isoflurane, placed on a heating pad to help regulate body temperature, and were injected subcutaneously (s.c.) with 10 μL of a 0.1 mg/mL (IR820 dye conc.) of star-IR820 conjugates (20%, 40%, 60%, and 90% acid-star-IR820) in the center of the right hind footpad. The mice were imaged from both the dorsal and right sides, both with and without the injection site being covered, using whole body fluorescence imaging (Cambridge Research and Instrumentation Maestro multi-spectrum imager, Woburn, MA) using an excitation filter of 710-760 nm and broadpass emission filter of 800-950 nm. The animals were imaged, under isoflurane anesthesia, for a maximum of 7 days.

Due to the intense fluorescence signal from the injection site saturating the camera, the injection area was covered with a piece of black tape allowing the visualization of the draining lymphatic vessels and lymph nodes. Images were acquired using the autoexposure function in the imaging software. The use of the autoexpose function resulted in different exposure times for each image, which were corrected for using the scaled counts/s in the image analysis.

3.2.7 In Vivo Imaging Data Analysis

Image analysis was performed using Maestro software (ver. 2.10). Regions of interest (ROI) were placed over the popliteal and iliac lymph nodes. The total signal (scaled counts/s, see equation below as described by the Maestro software) intensity values (arbitrary units, AU) were recorded for each ROI, for both positions (prone and right), and were graphed versus time in GraphPad Prism (ver. 4). The total fluorescence intensity vs. time graphs were integrated to give the cumulative fluorescence vs. time graphs. In addition, the area under the curve (AUC) was determined from the total fluorescence intensity vs. time graphs. Comparisons between multiple groups were made with one-way ANOVA analysis with a Turkey Multiple Comparisons post-test.

$$\text{Scaled counts/s} = \text{counts/full scale} \times 1/\exp(\text{s}) \times 1/\text{bin}^2 \times 1/\text{gain}$$

3.3 Results

3.3.1 Characterization of the Star Polymer and Star-IR820 Conjugates

The sugar-star polymers synthesis was verified by mass spectroscopy and NMR (data not shown). From the SEC calibration curves with polystyrene (1,180 to 339,500 g/mol) and PEG (3070 to 66,100 g/mol) standards, the molecular weights and PDI were calculated to be 75,000 and 1.132, for the protected sugar-star polymer and 45,000 and 1.15 for the deprotected sugar-star polymer, respectively. Following the conjugation of IR820 to the acid-star polymers, the acid-star-IR820 conjugates were bluish-purple in color. The IR820 loading degree was determined by ^1H NMR in MeOD, by the ratio of the aromatic ring protons of IR820 with the proton on the repeating unit of the star-polymer. The calculated MWs and the IR820 loading degrees are presented in Table 3.1.

% Acid	Theoretical Polymer MW (Da)	$M_{n,\ SEC*}$ (Da)	wt% IR820	# dyes/HA polymer
20	54, 000	45,890	7.8%	5.3
40	63, 000	54,390	6.8%	5.3
60	72,000	60,110	5.2%	4.6
90	85,500	75,100	8.6%	9.3

Table 3.1. IR820 loading degree on the various wt% acid-sugar star polymers.

$^*M_n$ obtained from PEG standards, DMF (10mM LiCl) as the mobile phase at a flow rate of 1 ml/min.

3.3.2 Rheological Properties

The trends between the two polymer systems (sugar star polymers and HA) with respect to increasing the concentration and MW on the apparent viscosity were determined by rheology. The viscosities of the star polymer and HA samples in Figures 3.1 A and B represent the apparent viscosities of the polymers at a shear rate of 100 s^{-1}. The data obtained for the other shear rates exhibited the same trends as presented in Figures 3.1 A and B for a shear rate of 100 s^{-1}; however, the apparent viscosities observed for the lower shear rates were observed to be slightly lower than for that at the shear rate reported du to the shear thinning of the polymers. As the concentration increases in Figure 3.1 A, for each individual sugar or sugar-acid star polymer, the apparent viscosity also increases. However, as the MW is increased (sugar < 20% < 40% < 60% < 90%) at a given concentration, the apparent viscosity remains relatively constant. In contrast, as the concentration of HA is increased, the viscosity also increases; the same trend is also observed with MW (Figure 3.1 B).

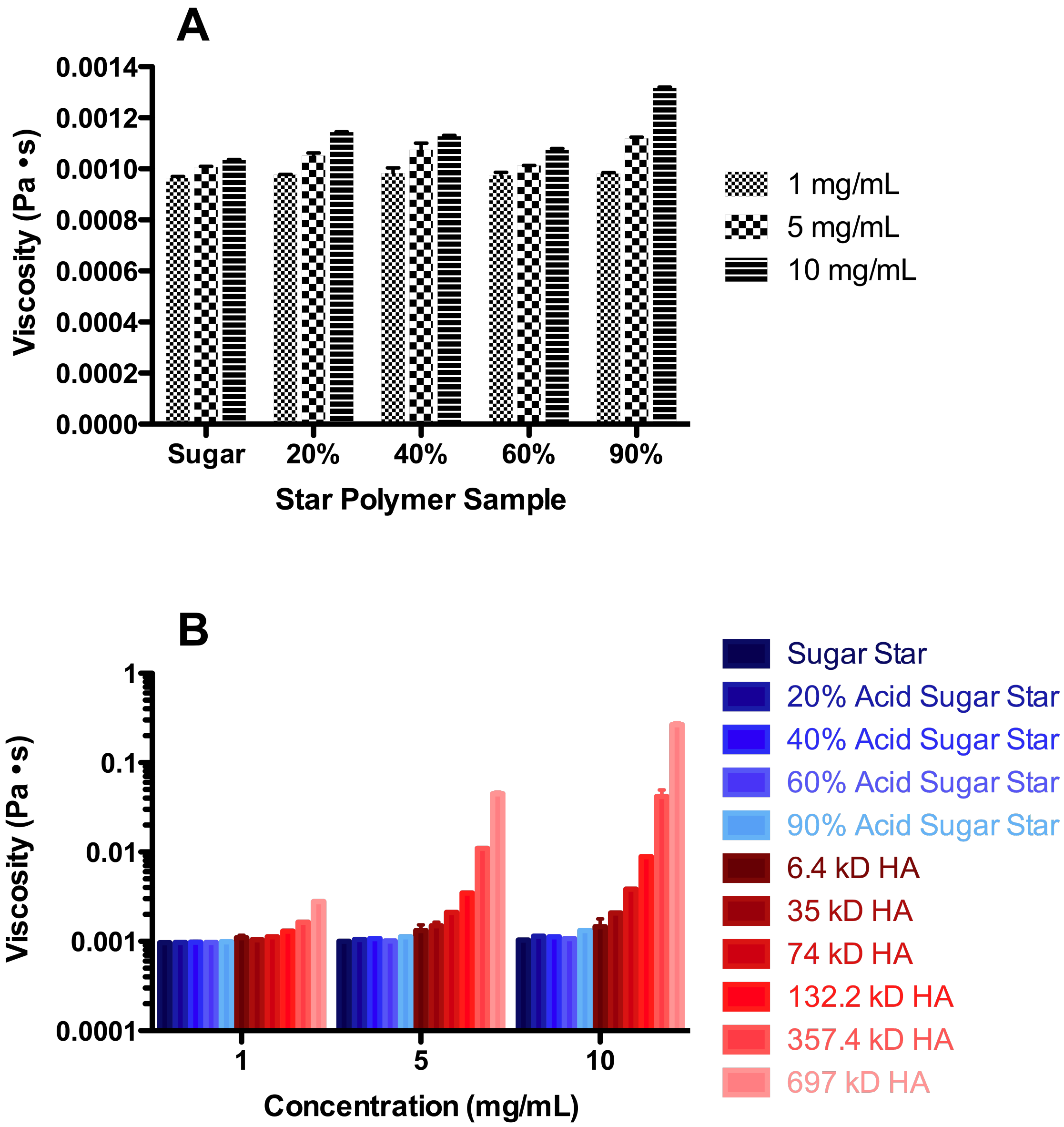

Figure 3.1. A) Viscosity of the sugar-star polymers in pH 7.4 PBS at a shear rate of 100 s^{-1}. B) Viscosity of HA and star polymers at 1, 5, and 10 mg/mL in PBS pH 7.4 at a shear rate of 100 s^{-1}. (n=3)

3.3.3 Zeta Potential of the Star Polymers

A linear response between the wt% acid and zeta potential was observed ($R^2 = 0.9831$). The zeta potentials in Figure 3.2 were for the 100 µg/mL concentration. The zeta potentials of the star polymer samples were determined at pH >> pK_a, to ensure that all of the carboxylic acid functional groups were fully ionized to minimize effects of pH changes on the measurements due to partial protonation of the carboxylic acids. Partial protonation would lead to minor changes in the pH, and a reduction in the double layer thickness leading to zeta potentials of lower magnitude than for fully ionized polymers. Further, the pH studied would be indicative of the ionization state *in vivo*, thus a leading to biologically relevant zeta potentials for the star polymers. The zeta potential readings for the other concentrations (1 and 10 µg/mL) resulted in erratic readings, suggesting that the concentration was too dilute in order to achieve an adequate signal to noise ratio obtain quantitative data. Further, in a previous zeta potential study, the pH was not controlled and the samples were 5× more concentrated, which also lead to erratic zeta potential readings with no real correlation (data not shown).

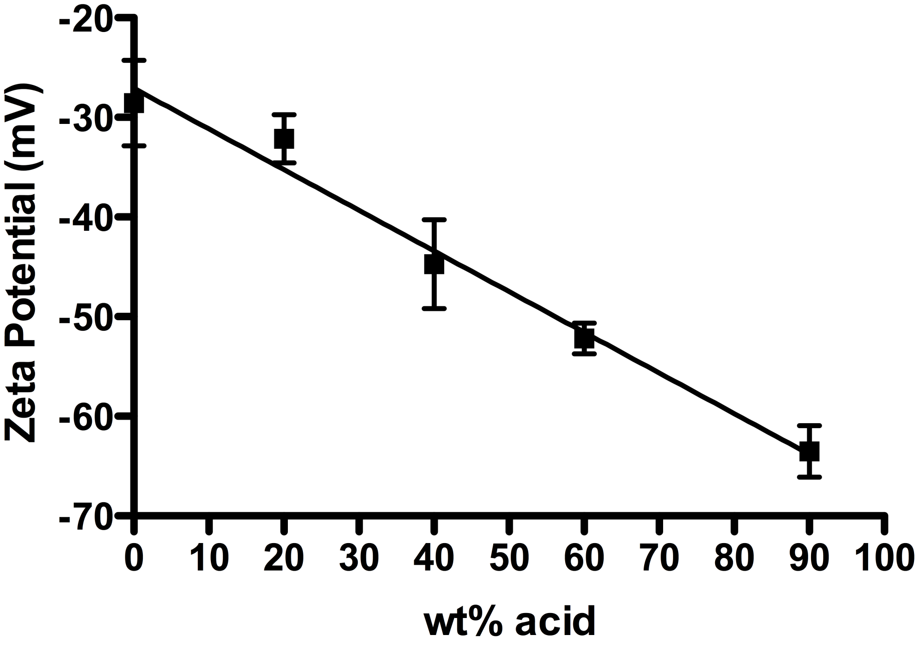

Figure 3.2. Zeta potentials of the different wt% acid sugar star polymers at 20 °C, 100 μg/mL, and a 1-mM phosphate buffer (pH 7.25) with 1-mM KCl.

3.3.4 In Vitro Toxicity of the Star Polymers

All four of the sugar-acid star polymers had similar anti-proliferative activity in all of the cell lines examined, with the exception of the 60% acid sugar star polymer in the MDA-1986 cells, which exhibited a 10-fold increase in toxicity compared to the other cell lines (Table 3.2).

	Cell Line					
wt % Acid	HUVEC	A2058	4T1.2 Neu	B16F10	MDA1986	MDA-MB-231
20	~50 µM (2.7 mg/mL)	~50 µM (2.7 mg/mL)	~50 µM (2.7 mg/mL)	------	------	------
40	~55 µM (3.5 mg/mL)	~40 µM (2.5 mg/mL)	~50 µM (3.2 mg/mL)	------	------	------
60	~100 µM (7.2 mg/mL)	~60 µM (4.3 mg/mL)	~100 µM (7.2 mg/mL)	>100 µM (7.2 mg/mL)	10 µM (0.72 mg/mL)	≥100 µM (7.2 mg/mL)
90	~55 µM (4.7 mg/mL)	~50 µM (4.3 mg/mL)	~55 µM (4.7 mg/mL)	------	------	------

Table 3.2. IC_{50} values of the sugar-acid star polymers in various cell lines.

3.3.5 In Vivo Imaging of Star-IR820

In this study, the four sugar-acid-star-IR820 conjugates are approximately the same molecular weight but have various degrees of anionic charges and a wide zeta potential distribution. The differences in the lymphatic uptake of the star polymers after s.c. administration are governed by the effect of charge rather than size. Drainage from the injection site occurs at similar rates for all four of the sugar-acid-star-IR820 conjugates, as indicated by the same t_{max} (time to reach maximal fluorescence signal) of 45 min (Table 3.3). As described in Chapter 2, with a series of six different MW HA-IR820 conjugates with the same charge, the t_{max} increased with the polymer MW.

The drainage kinetics to the popliteal and iliac nodes of the acid-star-IR820 conjugates post s.c. administration are presented in Figures 3.3 A and 3.4 B, respectively. The kinetic profile for the lymphatic drainage of the 20% acid-star-IR820 conjugate to both the popliteal and iliac nodes indicates that the 20% acid-star-IR820 conjugate has statistically lower lymphatic uptake and increased retention in the popliteal and iliac lymph nodes over the length of the study compared to the 40, 60 and 90% acid-star-IR820 conjugates (popliteal node, $p<0.05$, <0.0001, and <0.001, for the 40, 60 and 90% acid, respectively; iliac node, $p<0.0001$ for all three conjugates). The 20% acid conjugate is highly retained at the injection site and the popliteal node, as indicated by the lower maximum fluorescence signal and longer $t_{50\%}$ (time required for the fluorescence signal to reduce by 50%) (Table 3.3 and Figure 3.3A).

Over the first 24 and 6 hr, the kinetic profile for the lymphatic drainage to the popliteal node of the 40 and 90% acid-star-IR820 conjugates were significantly different than that of the 60% acid-star conjugate ($p<0.05$), as indicated by its significantly shorter $t_{50\%}$ (Figure 3.3A and Table 3.3). Whereas, the 40 and 90% acid-star-IR820 conjugates did not exhibit any significant differences in their lymphatic uptake to the popliteal node, which both have similar $t_{50\%}$ values (Figure 3.3A and Table 3.3). The kinetic profiles for the lymphatic uptake to the iliac node revealed slightly different trends than that for the popliteal node. The 90% acid-star-IR820 conjugate profile was statistically different than the 40 and 60% acid-star-IR820 conjugates over the first 24 and 50 hrs, respectively ($p<0.05$), in that the 90% acid-star-IR820 conjugate exhibited the shortest t_{max} and a longer $t_{50\%}$ than for the 40 and 60% conjugates which had similar $t_{50\%}$ and t_{max} values Figure 3.4A and Table 3.3).

The 40-90% acid-star-IR820 conjugates exhibit remarkably different nodal retentions in the popliteal and iliac lymph nodes. The 60% acid-star-IR820 cleared rapidly from the popliteal node compared to the other conjugates (indicated by the short $t_{50\%}$)(Table 3.3), but was retained in the iliac node for almost a day. In contrast, the 40% and 90% acid-star-IR820 conjugates have similar popliteal $t_{50\%}$ values of ca. 7 hrs, but the 90% acid-star-IR820 was retained two times longer in the iliac node in comparison with 40% and 60% acid-star-IR820 conjugates (Table 3.3). Further, the 20% acid-star-IR820 conjugate was highly retained in both the popliteal and iliac nodes compared to its more anionic counterparts as demonstrated by its long $t_{50\%}$ values. However, the distribution of the AUC for the different degrees of anionic charge were similar for both the popliteal and iliac nodes (Figures 3.3 C and 3.4C). The 40-90% acid-star-IR820 conjugates exhibited a 2.5- to 3.5-fold increase in the lymphatic uptake compared to the 20% acid-star-IR820 conjugate for both the popliteal and iliac nodes. For both the popliteal and iliac nodes, the cumulative drainage and AUCs of the 40, 60, and 90% acid-star-IR820 conjugates are similar, with no statistical differences between the three conjugates (Figures 3.3 B, 3.3 C, 3.4 B, and 3.4C).

	Popliteal		Iliac	
wt% Acid	t_{max} (min)	$t_{50\%}$ (hr)	t_{max} (hr)	$t_{50\%}$ (hr)
20	45-50	19.5	1	113.6
40	45-50	6.9	2	18.6
60	45-50	1.9	1	19
90	45-50	7.7	0.5	40

Table 3.3. t_{max} and $t_{50\%}$ values for the popliteal and iliac lymph nodes after s.c. administration of the 20%, 40%, 60%, and 90%-acid-star-IR820 conjugates in the right hind footpad of mice.

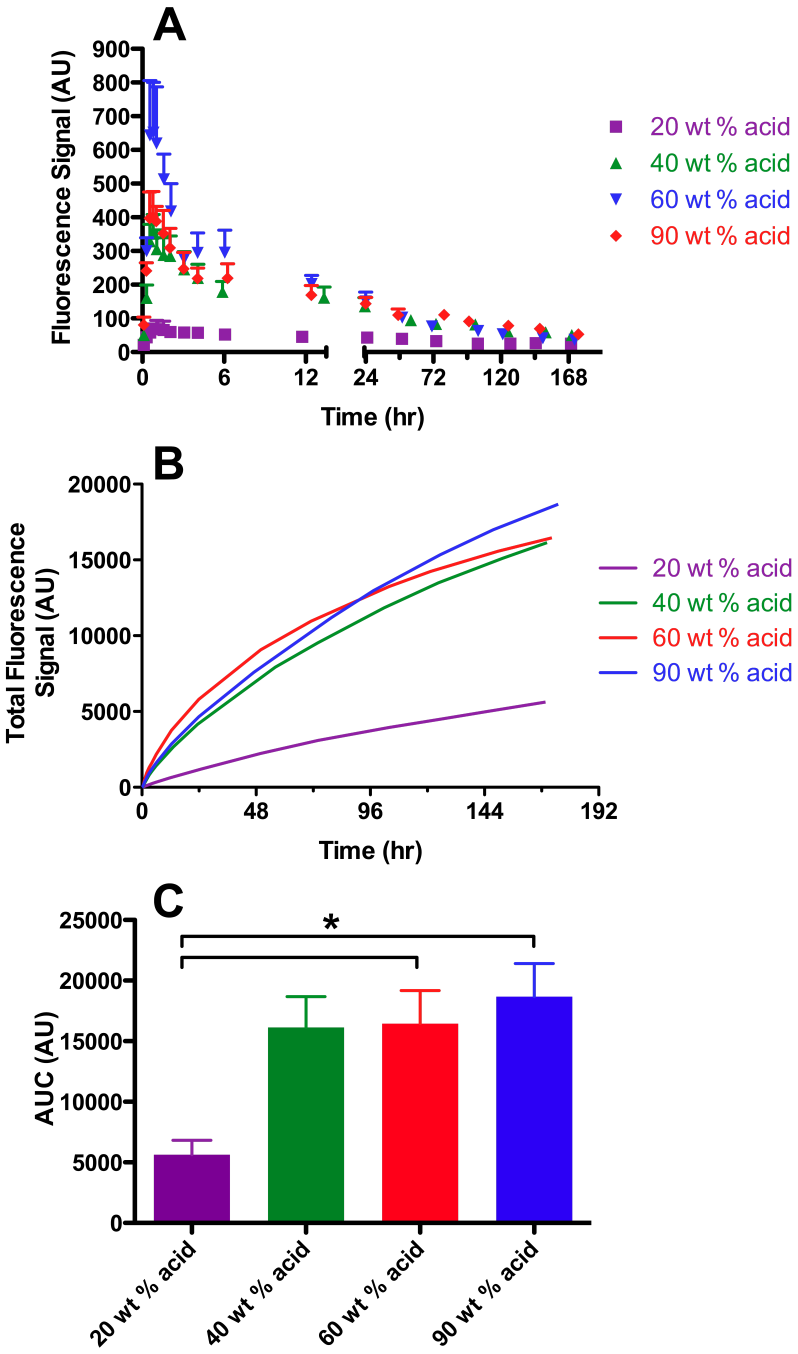

Figure 3.3. Star-IR820 drainage to the popliteal lymph node. A) Drainage kinetics to the popliteal lymph node after s.c. administration into the right hind footpad. B) Cumulative drainage of the star-IR820 conjugates to the popliteal node. C) AUCs in the popliteal node of the various wt% acid star-IR820 conjugates. (AU ≡ Arbitrary Units) (* $p = 0.0194$)

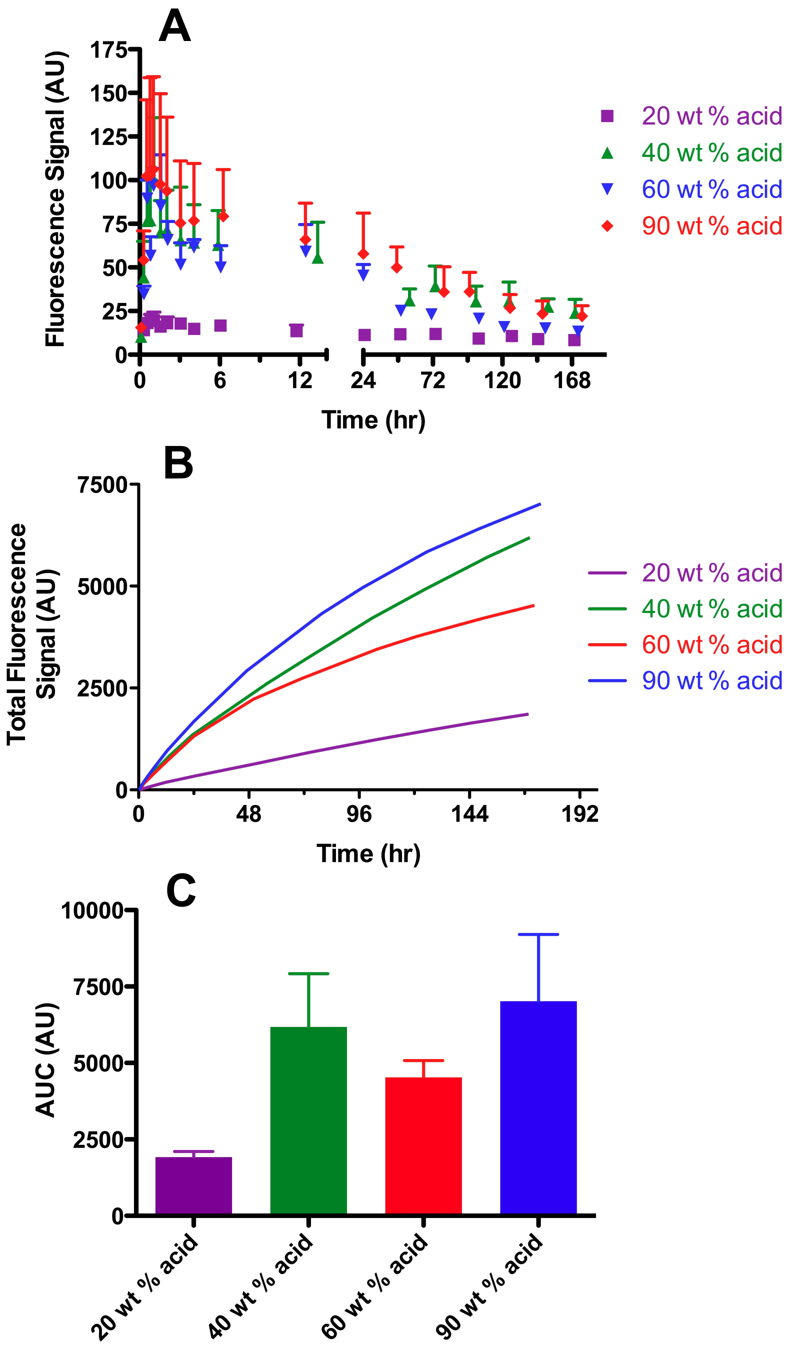

Figure 3.4. Star-IR820 drainage to the iliac lymph node. A) Drainage kinetics to the iliac lymph node after s.c. administration into the right hind footpad. B) Cumulative drainage of the star-IR820 conjugates to the iliac node. C) AUCs in the iliac node of the various wt% acid star-IR820 conjugates.

3.4 Discussion

The use of star polymers for the carrier optimization for lymphatic imaging and drug delivery rather than a linear polymers was due to the inherent low viscosities, increased solubility, decreased solution entanglement, and enhanced thermodynamic properties of star polymers [20,21,27]. The apparent viscosities of the star polymer were virtually independent of increases in the concentration and MW; while there were observed differences in the apparent viscosities, when compared to water and HA, these differences are negligible. Further, the viscosity of water at 20°C is 0.001 Pa·s, and the apparent viscosities of the star polymers is ca. 0.001 to 0.0012 Pa·s, which is statistically insignificant compared to viscosity of water. Conversely, HA is a viscoelastic, non-Newtonian behaving polymer that exhibits shear thinning in the presence of shear stress. Further, the viscosity of HA is concentration, pH, and ionic strength dependent [28]. Even at low shear rates and concentrations, HA exhibits shear thinning behavior. Figure 3.1 B clearly demonstrates the MW and concentration dependence of HA on the apparent viscosity, which are not factors with the star polymer samples.

In addition to size, the charge plays a critical role in the lymphatic uptake, retention, and disposition of intralymphatic carriers [1,9-11]. The extracellular matrix, consisting of polyanionic glycosaminoglycans (GAGs), carries a net negative charge at physiological pH due to the ionization of the carboxylic acids of the GAGs [3,29]. Negatively charged particles are readily drained from the interstitium after subcutaneous administration due to the electrostatic repulsions between the negatively charged particles and the extracellular space [1]. Conversely positively charged particles drain more slowly from the injection site due to the attractive forces between the particles and the negatively charged matrix. Zeta Potential can be used to measure the ionic nature of nanoparticles; where a zeta potential greater than 30 mV is indicative of a strongly cationic particle, between +10 and -10 mV is considered to be a neutral particle, and less than -30 mV is indicative of a strongly anionic particle [30].

The correlation between the zeta potential and the percent substitution of succinic anhydride on the star polymer, allows for potential comparisons of the lymphatic uptake of the star polymer with other polymeric systems. As observed for the star-polymers, an increase in the anionic character resulted in an increase in lymphatic uptake until the zeta potential (ζ) approached -40 mV ($\zeta = -44.72 \pm 4.45$ mV for the 40% acid-star polymer, Figure 3.2); once the zeta potential falls below ca. -40 mV, no significant increases in the total lymphatic uptake is expected for the star polymers. A similar trend with an increase in the anionic character resulting in an increase in the lymphatic uptake was observed by Rao and coworkers [1]. In which the authors developed a series of PLGA-PMA:PLGA-COOH nanoparticles with an increasing ratio of PLGA-COOH to PLGA-PMA to increase the anionic character, resulting in a decrease in zeta potential (from -44.6 ± 11.3 mV to -57.1 ± 11.1 mV). As the zeta potential decreased, an increase in the lymphatic uptake was observed. A 4.7-fold increase in the nanoparticle concentration in the popliteal node and a 10.1-fold increase in the cumulative nodal uptake (combination of the popliteal, internal inguinal, iliac, and renal lymph nodes) was observed for the -57.1 mV (20:80 PLGA-PMA:PLGA-COOH) nanoparticles.

Optimization of intralymphatic drug delivery vehicles for rapid lymphatic uptake and enhanced nodal retention requires modifying the particle's charge in addition to its size, which can determine the ultimate fate of subcutaneously injected particles. Cationic particles drain the slowest from the injection site after a s.c. injection, are poorly retained by the lymph nodes, have increased toxicity, liver accumulation, and have a high propensity to be engulfed by macrophages [9,10,13,31,32]. Whereas negatively charged particles exhibit enhanced lymphatic uptake, increased nodal retention, and decreased toxicity.

Toxicity both *in vitro* and *in vivo* are of great concern in the development of synthetic polymers for enhanced lymph node retention for localized sustained delivery. Cationic dendrimers exert their toxicity by interacting with the negatively charged lipid bilayer, resulting in destabilization of the cellular membrane [13,32]. The star polymers do not exhibit significant toxicity *in vitro* when compared to similar poly-ionic polymers currently used for drug and gene delivery (IC_{50} ca. 5 mg/mL). For example, Malik et al. demonstrated that G3 and G4 PAMAM, G3 and G4 DAB, and G1-G3 DAE dendrimers exhibited similar toxicity to that of 56-kD poly-L-lysine (ca. 50 μg/mL) in B16F10 cells after a 72 hr incubation [33]. Further, Roberts et al. demonstrated that PAMAM toxicity is concentration and generation dependent in V79 Chinese hamster lung fibroblast cells, where as the PAMAM generation was increased, the toxicity also increased (G3, G5 and G7; 100 nM, 10 μM, and 1 mM). For a G7 PAMAM (MW 116,493 Da), incubation with only 100 nM (ca. 11 μg/mL) PAMAM, for 24 hr, resulted in 90% cell death in the V79 cells [34]. Additionally, polyethylenimine (PEI) which is commonly used in gene transfection, also exhibits a relatively high IC_{50} value (19 μg/mL for a 25 kD branched PEI) in HR5-CL11 (human cervical cancer) cells after a 48 hr incubation [35]. In comparison, the sugar-acid star polymers are 100-fold less toxic than most cationic dendrimers and PEI used for drug and gene delivery. Peng et al. demonstrated that chlorin-core star block m-PEG-bPCL copolymer micelles exhibited no observable toxicity against MCF-7 breast cancer cells after 24 hr incubation at the highest concentration of 500 μM [36], which is similar to our star polymers (IC_{50} ca. 50 to 100 μM).

To assess the effect of increasing negative charge on the lymphatic drainage and nodal retention of the series of anionic star polymers, we employed whole body fluorescence imaging. Mice were imaged from both their right and dorsal sides to detect drainage into the popliteal and iliac nodes. The same trends were observed for both imaging positions; but the right side was analyzed as it produced greater signal intensities and a higher signal to noise ratio compared to the dorsal or ventral positions. The ventral position resulted in a decrease in the signal to noise ratio, due to the increased fluorescence contributions of the organs in the abdomen. In addition, the iliac node was not visualized due to its increased depth in this position. Both the lymph nodes and draining lymphatic vessels were clearly visualized against the background tissues using fluorescence imaging (Figure 2.3 A found in Chapter 2). Due to limitations of *in vivo* fluorescence imaging, only shallow nodes were identified; we do not discount further drainage past the iliac node of these star-IR820 conjugates.

Reports on the effects of charge on the lymphatic uptake have demonstrated that negatively charged particles have increased lymphatic uptake compared to neutral to positively charged particles [9-11], along with increased nodal retention [1,12]. Therefore, the effect of varying the negative charge on the cumulative lymphatic uptake and nodal retention of a series of star polymers was investigated. Increasing the anionic charge from 20% to 40% wt-acid star polymer resulted in approximately a 3-fold increase in the lymphatic uptake for both the popliteal and iliac lymph nodes. Similar trends were observed for the 40-90 % acid star polymers for the cumulative fluorescence signals and AUCs over the course of the one-week study (Figures 3.3 B, 3.3 C, 3.4 B, and 3.4 C), suggesting that there is a threshold for the lymphatic uptake with regards to the degree of anionic charge required. The threshold for the sugar-acid star polymer system this is 40 wt% acid substitution ($\zeta \leq -40$ mV); additional increases in the anionic character did not lead to an increase in the lymphatic uptake, as seen with the similar AUCs for the 60 and 90% acid-star-IR820.

In a similar study, Rao and coworkers investigated the effect of increasing anionic charge on the lymphatic uptake of PLGA nanoparticles [1]. Rao et al. observed a 10-fold increase in the cumulative lymphatic drainage as the amount of carboxylic acid terminated PLGA (PLGA-COOH) was increased from 20% to 80%, thus decreasing the zeta potential from -44.6 ± 11.3 to -57.1 ± 11.1 mV. In contrast to Rao's observations of increasing the negative charge of the nanoparticles resulting in a continuous increase in the lymphatic uptake, for the star polymers described herein, increased lymphatic uptake was observed with increasing the negative charge until a zeta potential of -40 mV (40% acid-star polymer); whereas further increases in the negative charge did not effect the lymphatic uptake. Even though the 40-90% acid-star polymers exhibited similar cumulative lymphatic uptake, the 60% acid-star polymer conjugate was selected as the optimal star polymer platform for further lymphatic imaging and drug delivery development, in part due to the rapid drainage observed from the popliteal lymph node coupled with the long retention in the iliac node. The sugar moiety in the repeating unit of the star polymer was included for its increased solubility, but also for enhanced lymphatic uptake and nodal retention as previously demonstrated by the addition of saccharides to liposomes [37]. Additionally, no signs of toxicity or adverse effects were observed for the duration of the study with the concentrations of star polymers injected (ca. 0.4 to 0.7 mg/kg star-IR820 conjugate).

3.5 Conclusions

A new star-polymer with various degrees of anionic charge for lymphatic imaging and drug delivery was developed. The star-polymer platform displays similar characteristics to dendrimers, but entails more straightforward synthesis and cost effectiveness. In addition, this platform exhibited significantly reduced toxicities compared to conventional dendrimers such as PAMAM. Star polymers are advantageous, with the addition of the sugar moieties and the polyanionic nature, they exhibit similar characteristics to endogenous polysaccharide, such as HA, but are significantly less viscous. The sugar-star polymers exhibited viscosities similar to that of water and were independent of increases in both the molecular weight and concentration, unlike molecular weight and concentration dependence on the HA viscosity. Further, the star polymer platform provides a compact, low polydispersity carrier with numerous functional groups for conjugation.

The effect of negative charge on the lymphatic uptake was successfully determined using *in vivo* fluorescence imaging. The 40%-90% acid-star polymers did not exhibit significant differences in the cumulative drainage to both the popliteal and iliac lymph nodes; however, the retention in the popliteal node for the 60% acid was significantly shorter than for the other wt% acid-star polymers. The 60% acid-star polymer was selected as the optimal degree of succinic acid modification, due to the rapid drainage from the popliteal lymph node and enhanced retention in the iliac node.

The star polymers were highly retained within the iliac node compared to the popliteal node, suggesting that the star polymer platform may be beneficial for treatment of the deep lymphatics where metastases in the echelon nodes are present. The star polymers have the potential to be used for the treatment of locally advanced lymphatically metastatic cancers with the involvement of two or more lymph nodes, due to the enhanced retention in the iliac lymph nodes for all of the conjugates. Further, the rapid drainage of the 40-90% acid-star polymer could aid in minimizing the local release of chemotherapeutics at the injection site due to their rapid drainage from the injection site and enhanced lymphatic uptake relative to the 20% acid star polymer. Additionally, the acid-star polymers would be ideal carriers for a drug conjugate with a rapid release half-life, such as the star-GA conjugate discussed in Chapter 4, in order to minimize the potential toxicities related to a slow draining carrier with a fast releasing drug. The local release of chemotherapeutics at the injection site can lead to undesirable local toxicities, such as inflammation and tissue necrosis, or toxicities associated with the systemic uptake of the free drug. After selection of the 60% acid-star polymer as the optimal new delivery platform, we developed a chemotherapeutic-, such as a geldanamycin analogue, star polymer conjugate for intralymphatic drug delivery to the lymphatics of metastatic cancers such as melanoma and breast cancer, which is discussed in Chapter 4.

3.6 References

1. Rao, D.A.; Forrest, M.L.; Alani, A.W.; Kwon, G.S.; Robinson, J.R., Biodegradable plga based nanoparticles for sustained regional lymphatic drug delivery. *J Pharm Sci* **2010**, *99*, 2018-2031.

2. Porter, C.J., Drug delivery to the lymphatic system. *Crit Rev Ther Drug Carrier Syst* **1997**, *14*, 333-393.

3. Hawley, A.E.; Davis, S.S.; Illum, L., Targeting of colloids to lymph-nodes - influence of lymphatic physiology and colloidal characteristics. *Adv Drug Deliver Rev* **1995**, *17*, 129-148.

4. Cai, S.; Thati, S.; Bagby, T.R.; Diab, H.M.; Davies, N.M.; Cohen, M.S.; Forrest, M.L., Localized doxorubicin chemotherapy with a biopolymeric nanocarrier improves survival and reduces toxicity in xenografts of human breast cancer. *J Control Release* **2010**, *146*, 212-218.

5. Cai, S.; Xie, Y.; Bagby, T.R.; Cohen, M.S.; Forrest, M.L., Intralymphatic chemotherapy using a hyaluronan-cisplatin conjugate. *J Surg Res* **2008**, *147*, 247-252.

6. Cai, S.; Xie, Y.; Davies, N.M.; Cohen, M.S.; Forrest, M.L., Carrier-based intralymphatic cisplatin chemotherapy for the treatment of metastatic squamous cell carcinoma of the head & neck. *Ther Deliv* **2010**, *1*, 237-245.

7. Cai, S.; Xie, Y.; Davies, N.M.; Cohen, M.S.; Forrest, M.L., Pharmacokinetics and disposition of a localized lymphatic polymeric hyaluronan conjugate of cisplatin in rodents. *J Pharm Sci* **2010**, *99*, 2664-2671.

8. Cohen, M.S.; Cai, S.; Xie, Y.; Forrest, M.L., A novel intralymphatic nanocarrier delivery system for cisplatin therapy in breast cancer with improved tumor efficacy and lower systemic toxicity in vivo. *Am J Surg* **2009**, *198*, 781-786.

9. Takakura, Y.; Hashida, M.; Sezaki, H., Lymphatic transport after parenteral drug administration. In *Lymphatic transport of drugs*, Charman, W.N.; Stella, V.J., Eds. CRC Press: Boca Raton, 1992; pp 255-278.

10. Patel, H.M.; Boodle, K.M.; Vaughan-Jones, R., Assessment of the potential uses of liposomes for lymphoscintigraphy and lymphatic drug delivery. Failure of 99m-technetium marker to represent intact liposomes in lymph nodes. *Biochim Biophys Acta* **1984**, *801*, 76-86.

11. Takakura, Y.; Atsumi, R.; Hashida, M.; Sezaki, H., Development of a novel polymeric prodrug of mitomycin c, mitomycin c-dextran conjugate with anionic charge. II. Disposition and pharmacokinetics following intravenous and intramuscular administration. *Int J Pharm* **1987**, *37*, 145-154.

12. Kaminskas, L.M.; Porter, C.J., Targeting the lymphatics using dendritic polymers (dendrimers). *Adv Drug Deliv Rev* **2011**, *63*, 890-900.

13. McNerny, D.Q.; Leroueil, P.R.; Baker, J.R., Understanding specific and nonspecific toxicities: A requirement for the development of dendrimer-based pharmaceuticals. *Wiley Interdiscip Rev Nanomed Nanobiotechnol* **2010**, *2*, 249-259.

14. Parveen, S.; Misra, R.; Sahoo, S.K., Nanoparticles: A boon to drug delivery, therapeutics, diagnostics and imaging. *Nanomedicine* **2011 [Epub ahead of print]**.

15. Jain, N.K.; Asthana, A., Dendritic systems in drug delivery applications. *Expert Opin Drug Deliv* **2007**, *4*, 495-512.

16. Jevprasesphant, R.; Penny, J.; Jalal, R.; Attwood, D.; McKeown, N.B.; D'Emanuele, A., The influence of surface modification on the cytotoxicity of PAMAM dendrimers. *Int J Pharm* **2003**, *252*, 263-266.

17. Kobayashi, H.; Brechbiel, M.W., Nano-sized MRI contrast agents with dendrimer cores. *Adv Drug Deliv Rev* **2005**, *57*, 2271-2286.

18. Wijagkanalan, W.; Kawakami, S.; Hashida, M., Designing dendrimers for drug delivery and imaging: Pharmacokinetic considerations. *Pharm Res* **2011**, *28*, 1500-1519.

19. Mendrek, B.; Trzebicka, B., Synthesis and characterization of well-defined poly(tert-butyl acrylate) star polymers. *Eur Polym J* **2009**, *45*, 1979-1993.

20. Cameron, D.J.A.; Shaver, M.P., Aliphatic polyester polymer stars: Synthesis, properties and applications in biomedicine and nanotechnology. *Chem Soc Rev* **2010**, *40*, 1761-1776.

21. Hult, A.; Johansson, M.; Malmström, E., Hyperbranched polymers. In *Branched polymers II*, Roovers, J., Ed. Springer Berlin / Heidelberg: 1999; Vol. 143, pp 1-34.

22. Chen, Y.; Shen, Z.; Barriau, E.; Kautz, H.; Frey, H., Synthesis of multiarm star poly(glycerol)-block-poly(2-hydroxyethyl methacrylate). *Biomacromolecules* **2006**, *7*, 919-926.

23. Boyer, C.; Bulmus, V.; Davis, T.P.; Ladmiral, V.; Liu, J.; Perrier, S., Bioapplications of RAFT polymerization. *Chem Rev* **2009**, *109*, 5402-5436.

24. Gregory, A.; Stenzel, M.H., The use of reversible addition fragmentation chain transfer polymerization for drug delivery systems. *Expert Opin Drug Deliv* **2011**, *8*, 237-269.

25. Stenzel, M.H.; Davis, T.P.; Barner-Kowollik, C., Poly(vinyl alcohol) star polymers prepared via MADIX/RAFT polymerisation. *Chem Commun (Camb)* **2004**, 1546-1547.

26. Ting, S.R.; Gregory, A.M.; Stenzel, M.H., Polygalactose containing nanocages: The RAFT process for the synthesis of hollow sugar balls. *Biomacromolecules* **2009**, *10*, 342-352.

27. Qiu, L.Y.; Bae, Y.H., Polymer architecture and drug delivery. *Pharm Res* **2006**, *23*, 1-30.

28. Lapcik, L.J.; Lapcik, L.; De Smedt, S.; Demeester, J.; Chabrecek, P., Hyaluronan: Preparation, structure, properties, and applications. *Chem Rev* **1998**, *98*, 2663-2684.

29. Aukland, K.; Reed, R.K., Interstitial-lymphatic mechanisms in the control of extracellular fluid volume. *Physiol Rev* **1993**, *73*, 1-78.

30. Clogston, J.D.; Patri, A.K., Zeta potential measurement. *Methods Mol Biol* **2011**, *697*, 63-70.

31. Hawley, A.E.; Illum, L.; Davis, S.S., Lymph node localisation of biodegradable nanospheres surface modified with poloxamer and poloxamine block co-polymers. *FEBS Lett* **1997**, *400*, 319-323.

32. Jain, K.; Kesharwani, P.; Gupta, U.; Jain, N.K., Dendrimer toxicity: Let's meet the challenge. *Int J Pharm* **2010**, *394*, 122-142.

33. Malik, N.; Wiwattanapatapee, R.; Klopsch, R.; Lorenz, K.; Frey, H.; Weener, J.W.; Meijer, E.W.; Paulus, W.; Duncan, R., Dendrimers: Relationship between structure and biocompatibility in vitro, and preliminary studies on the biodistribution of 125I-labelled polyamidoamine dendrimers in vivo. *J Control Release* **2000**, *65*, 133-148.

34. Roberts, J.C.; Bhalgat, M.K.; Zera, R.T., Preliminary biological evaluation of polyamidoamine (PAMAM) starburst dendrimers. *J Biomed Mater Res* **1996**, *30*, 53-65.

35. Grayson, A.C.; Doody, A.M.; Putnam, D., Biophysical and structural characterization of polyethylenimine-mediated siRNA delivery in vitro. *Pharm Res* **2006**, *23*, 1868-1876.

36. Peng, C.-L.; Shieh, M.-J.; Tsai, M.-H.; Chang, C.-C.; Lai, P.-S., Self-assembled star-shaped chlorin-core poly(ε-caprolactone)-poly(ethylene glycol) diblock copolymer micelles for dual chemo-photodynamic therapies. *Biomaterials* **2008**, *29*, 3599-3608.

37. Wu, M.S.; Robbins, J.C.; Bugianesi, R.L.; Ponpipom, M.M.; Shen, T.Y., Modified in vivo behavior of liposomes containing synthetic glycolipids. *Biochim Biophys Acta* **1981**, *674*, 19-29.

Chapter 4. Development of a Star Polymer-Geldanamycin (GA) Conjugate and the Intralymphatic Delivery of Star-GA for the Treatment of Three Orthotopic Tumor Models

4.1 Introduction

Many cancers metastasize via the lymphatic system, including melanoma, breast, colon, lung, and ovarian cancers [1,2]. Accurate determination of the lymph nodes involved in the early lymphatic spread of the primary tumor and adequate treatment is paramount for survival of the patient. The first non-hematologic metastatic site is usually the regional lymph node basin in both melanoma and breast cancer [3,4]. For melanoma and breast cancer, the 5-year survival rates drop dramatically when the primary tumor has metastasized; the 5-year survival for melanoma and breast cancer, respectively, are >90% and 98% for localized disease with no lymphatic involvement, 40 to 60% and 84% if 1 to 3 local nodes are involved, and 15 to 20% and 23% when distant nodes and sites are involved [5,6]. Further, lymphatic vessel growth within the tumor has been shown to have a positive correlation with the metastatic spread of melanoma, breast, and head and neck cancers [7], as metastasizing cancer cells will follow cytokine gradients into the draining lymphatics [1]. Lymph node biopsies have been used since the 1950s, in the diagnosis of breast cancer, and sentinel lymph node biopsies, reviewed in chapter 1, have been used for the clinical staging of melanoma and breast cancer since the early 1990s [8]. Lymph nodes that test positive for micrometastases by pathology are identified and removed, potentially saving the patient from a complete lymphadenectomy of unaffected nodes or a radical mastectomy.

The current therapies for regional lymph node involvement in melanoma are wide local excision of the primary tumor and removal of the regional lymph nodes [9,10]; frequently surgery is followed by chemotherapy. It has been reported that 40-50% of primary melanomas are present on the limbs. Furthermore, melanoma is considered to be relatively resistant to chemotherapeutics along with radiation [9], with response rates of only 20% with systemic treatment of the extremities [11]. Therefore to improve the response rates to chemotherapeutics, isolated limb perfusion (ILP) was introduced, which allows 15-20 times the maximum tolerated dose (MTD) of the chemotherapeutic, melphalan, to be delivered locally [11,12], resulting in a 10-fold increase in the limb drug concentrations and minimized toxicities [11-13]. In addition to its toxicity, melphalan is poorly water solubility and extremely unstable in solution (plasma half life is ca. 1 hr) [14,15]. Patients treated with melphalan at local doses far above the MTD, using ILP, achieve complete response rates of 55% and partial responses of 26% [16], although the perfusate can leak into the systemic circulation in up to 12% of patients which causes systemic toxicities [17]. However, with melanoma metastases past the extremities, the most common and effective treatment is dacarbazine, which offers response rates of only 10-13%, and complete response rates less than 5% [18]. Although, after 30 years of the use of dacarbazine alone, it has not been shown to significantly improve survival time in a large trial. A recent randomized Phase III trial of the immunotherapeutic ipilimumab plus dacarbazine has demonstrated the first improvement in patient survival and a possible improvement over dacarbazine, with an overall survival of 11.2 months vs. 9.1 months, respectively [19].

Since the introduction of sentinel lymph node biopsy (SLNB) for breast cancer staging, treatments have become more specialized leading to a decrease in the number of radical mastectomies with complete axillary lymph node dissections [20,21] and an increase in the detection of micrometastases [22,23]. However, in a 700 patient study, it was reported that there is a high risk for relapse due to the presence of undetected nanometastases (<0.2 mm in diameter) upon initial staging [24]. In order to prevent these relapses, lymph node dissection is often followed by radiation, chemotherapy, or immunotherapy (for HER2 positive breast cancer). But these “preventative” measures also come at the high cost of side effects, including cardiotoxicity, associated with radiation [25], or chemotherapy using doxorubicin [26], and trastuzumab treatment alone and in combination with doxorubicin [27]. Additionally, about 25% of all breast cancers are HER2 positive, which represents an aggressive type of breast cancer that leads to poor prognosis and an increased potential for relapse [28-30]. Despite the improved outcome with the treatment of HER2 positive breast cancers with trastuzumab, a HER2 targeted humanized murine monoclonal antibody; almost all of the patients will experience relapse and metastatic progression due to the acquired resistance to treatment [31,32]. Although the prognosis is promising for those diagnosed with early breast cancer, treatment options are limited for those with undetected micro or nanometastases, locally advanced, or trastuzumab-resistant breast cancer. There is a critical need for the development of localized treatments for patients with micro-, nano- and in-transit lymphatic metastases for both localized and metastatic melanoma and breast cancer that are less radical than surgical dissection, radiation, or systemic chemotherapy, which carry their own associated risks and side effects.

Localized chemotherapy, such as ILP used for the treatment of limb melanomas, avoids systemic toxicities associated with intravenous therapy by restricting the toxic chemotherapy agents to the diseased tissue and minimizing the exposure to the normal unaffected tissues. However, current localized therapies, such as ILP and isolated hepatic perfusion, utilize isolation of the blood flow to the affected organ or tissue while perfusing high doses of chemotherapeutics above the MTD through the local arteries and veins. However, these techniques for localized delivery are not viable options for melanoma metastases beyond the limbs, melanomas of the head and neck or trunk, or breast cancer. Further, systemic chemotherapy offers limited penetration into lymphatics to treat lymphatic metastases [33]. Targeting polymeric-anticancer drug conjugates to the lymphatics will have improved efficacy and reduced toxicity compared to conventional systemic therapy, while treating lymph node metastases associated with lymphatically metastatic cancers, such as melanoma and breast cancer. Targeting particulates for lymphatic delivery is governed by the size and charge of the nanoparticles, with 10 to 100 nm anionic nanoparticles having the ideal characteristics for lymphatic uptake. We previously determined the optimal size and charge for the lymphatic delivery of nanoparticles to be 30-50 nm (Chapter 2) and polyanionic, with a zeta potential less than -40 mV (Chapter 3). With the previous experiences in our laboratory of the localized delivery of a hyaluronan-doxorubicin conjugate for the treatment of breast cancer [34], and the challenges arising from the highly viscous hyaluronan polymer and limited drug loading due to solubility issues, we sought to develop a multifunctional drug conjugate with low viscosity and improved carrier solubility utilizing star polymers. Star polymers have compact structure (like dendrimers), narrow polydispersities, large surface areas, low toxicity (Chapter 3), and low intrinsic viscosity [35-37].

Geldanamycin (GA), an ansamycin benzoquinone antibiotic, is HSP90 inhibitors that exhibits both antimicrobial activity and anticancer activity [38]. The anti-cancer activity of GA was first determined in the 1970s against L1210 murine leukemia and KB cells [39]; despite its encouraging in vitro and in vivo activity in early preclinical studies, its development was limited due to its significant hepatotoxicity in vivo [40]. Nevertheless, two of its C-17 analogues, 17-AAG and 17-DMAG, have been pursued in the clinic due to their enhanced activity, decreased liver toxicity, and increased water solubility (17-DMAG) [41]. Further, 17-AAG was found to have efficacy in both HER2 positive (SKBr3) and negative (MCF7) breast cancer cell lines, and deplete the HER2 oncoprotein in the SKBr3 cell line [42]. Due to its increased water solubility and equivalent activity, the development of 17-DMAG over 17-AAG has grown in interest. With the combined reports of HSP90 overexpression in melanoma [43], its function in the metastasis of melanoma [44], and activity against HER2 positive breast cancer [42], we developed a lymphatically targeted geldanamycin derivative-star polymer conjugate for the localized delivery to both locally advanced melanoma and breast cancers.

4.2 Experimental

4.2.1 Synthesis and Characterization of the Star-Geldanamycin Conjugate

The GA analogue, star polymer (described in Chapter 3 and Appendix 1), and star-GA conjugate were synthesized in our laboratory by Dr. Duan. Briefly, to a solution of geldanamycin (100 mg, 0.178 mmol, LC Laboratories) in dry chloroform (20 mL), ethanolamine (30 eq, Sigma) was added dropwise. The reaction was protected from light and was allowed to proceed at ambient temperature (ca. 20 °C) under argon protection for 4 h until the TLC showed complete consumption of the starting materials. The reaction mixture was then washed with 1-M HCl (100 mL) and dried over Na_2SO_4. The solvent was removed under reduced pressure, and the compound was used without further purification. ^{1}H-NMR in $CDCl_3$ was used to confirm the structure, and the NMR spectrum was consistent with the reported data and showed the compound was determined to be pure. The desired 17-((2-hydroxyethyl)amino)-17-demethoxygeldanamycin analogue (17-HEAG) was obtained as a purple solid (101 mg, 96%) (Scheme 4.1). ^{1}H-NMR ($CDCl_3$, 400 MHz): δ = 9.16 (s, 1H), 7.29 (s, 1H), 6.96 (d, J = 11.4 Hz, 1H), 6.61 (t, J = 11.7 Hz, 1H), 5.92 (d, J = 9.9 Hz, 1H), 5.87 (d, J = 10.6 Hz, 1H), 5.21(s, 1H), 4.79 (bs, 1H), 4.33 (d, J = 9.8 Hz, 1H), 3.93 (t, J = 5.2 Hz, 2H), 3.81-3.76 (m, 1H), 3.72-3.66 (m, 1H), 3.60 (d, J = 8.5 Hz, 1H), 3.49-3.45 (m, 1H), 3.38 (s, 3H), 3.29 (s, 3h), 2.81-2.74 (m, 1H), 2.70 (d, *J* = 13.6 Hz, 1H), 2.42 (dd, *J* = 10.5 Hz, 2.8 Hz), 2.06 (s, 3H), 1.83-1.85 (m, 5H), 1.78-1.54 (m, 3H), 1.02 (d, *J* = 7.0 Hz, 3H), 1.02 (d, *J* = 6.9 Hz, 3H).

Sugar-acid-star polymer (60% acid) (72 mg) was dissolved in dry DMF (20 mL) and was cooled to 0 °C. EDAC (65.2 mg, 0.34 mmol, Sigma) and HOBt·H_2O (52.3 mg, 0.34 mmol, Sigma) were added to the polymer solution. After five minutes, the 17-HEAG analogue (100 mg, 0.17 mmol) was added in one portion. The reaction was protected from light and allowed to proceed at room temperature (ca. 20 °C) overnight. The resulting solution was dialyzed (MWCO 10 kD, SpecraPor 7, Spectrum Laboratories) against EtOH: H_2O (1:1) for 12 hours with solvent exchanges every 3 hours followed by dialysis against 100% EtOH for 6 hours with solvent exchanges every 3 hours. The solvent was removed under reduced pressure yielding the pure star-GA conjugate (Scheme 4.1).

The conjugation degree of 17-HEAG to the star polymer was determined by ^{1}H-NMR (Bruker, 400MHz) in MeOD (Cambridge Isotope Laboratories) and UV spectroscopy (SPECTRA MAX PLUS, Molecular Devices) at 330 nm using a standard calibration curve (1-30 μg/mL) in MeOH. The conjugation degree was determined by comparing the ratio of the proton on the C19 position on the benzoquinone ring with the proton of the repeating unit of the star polymer from the ^{1}H-NMR spectra.

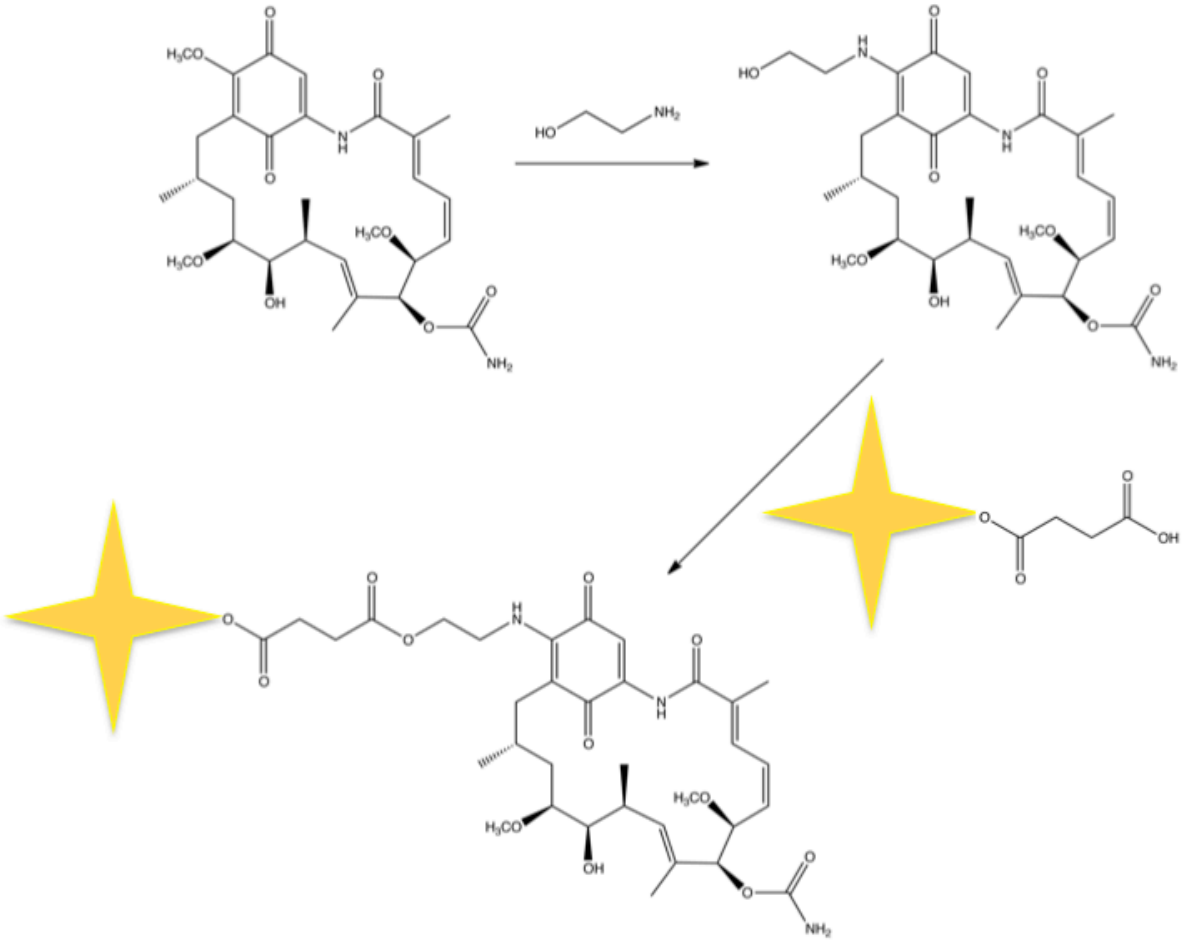

Scheme 4.1. Pictorial reaction scheme of the geldanamycin reaction with ethanolamine to give the 17-HEAG analogue, followed by the reaction of 17-HEAG with the 60% acid-star polymer resulting in the Star-GA conjugate.

4.2.2 In Vitro Cytotoxicity

B16F10 (lymphatically metastatic murine melanoma, ATCC), MDA-MB-231 (human breast cancer), and HUVEC (normal human endothelial) cell lines, were maintained in Dulbecco's modified Eagle's medium (DMEM) supplemented with 1% L-Glutamine and 10% bovine growth serum in 5% CO_2 atmosphere. The HER2-expressing murine breast cancer cell line, 4T1.2 Neu, was a gift from Dr. You, from the University of Pittsburg, and was maintained in DMEM supplemented with 1% L-Glutamine, 10 % bovine growth serum, and 500 μg/mL of G418 (geneticin) in 5% CO_2 atmosphere. The lymphatically metastatic human melanoma cell line, A2058, was purchased from ATCC, and was maintained in low sodium bicarbonate containing DMEM supplemented with 1% L-Glutamine, 10% bovine growth serum in 5% CO_2 atmosphere.

Prior to cell growth inhibition studies, cells were trypsinized and seeded at 3000 cells/well into 96-well tissue culture plates. After 24 hours, geldanamycin, 17-DMAG, 17-AAG, 17-HEAG, Star-GA (GA basis), or melphalan hydrochloride dilutions in 1× PBS (Fisher BioReagents, pH 7.4) with up to 3% DMSO (final well concentration, for the highest drug concentration) were added to the B16F10, A2058, HUVEC, 4T1.2 Neu, or MDA-MB-231 cells (n=8 or 12, 10 μL/well, 8 or 6 concentrations 10^{-10} to 10^{-3} M, respectively). Solutions of 10% trichloracetic acid was used as a negative control, media was used as a positive control, and 3% DMSO was used as an additional control (n=8 or 12, 10 μL/well). At 72 h post addition, 10 μL of resazurin blue in PBS was added (5 μM final concentration) to each well. After 3 hours, well fluorescence was measured ($\lambda_{ex}/\lambda_{em}$ = 560/590 nm) (SpectraMax Gemini, Molecular Devices). IC_{50}s were determined using the nonlinear regression curve fit of a one-site competition (GraphPad Prism 10).

4.2.3 In Vitro Release

Star-GA was dissolved in PBS at a GA concentration of 0.075 mg/mL (0.5 mg/mL total conc.) and was sealed in a dialysis bag (3500 MWCO, n=3, Pierce). The dialysis bags were placed in a temperature controlled bath set to 37 °C containing PBS under sink conditions; the bath was protected from light for the experiment duration. At predetermined time intervals, 150 μL aliquots were taken from the bags for 50 hr and were placed at -20 °C until analysis. The release samples were analyzed using a UV absorbance detector with a 17-HEAG standard curve (0.8 to 80 μg/mL, 11 concentrations). The release samples were diluted to 200 μL with PBS (3:4 dilution), the 17-HEAG standard curve dilutions (n=2), PBS (n=2), and the release samples (n=3) were added to a 96-well plate, and the UV absorbance of the plate was measured at 330 nm on a UV plate reader (SPECTRA MAX PLUS, Molecular Devices).

4.2.4 B16F10 Murine Melanoma Tumor Model

4.2.4.1 B16F10 Tumor Model Optimization

B16F10 cells were maintained in DMEM supplemented with 10% bovine growth serum and 1% L-Glutamine in 5% CO_2 atmosphere. Cells were trypsinized (0.25% w/v trypsin), and five different cell dilutions were made in 1×PBS (5×10^5, 5×10^6, 5×10^7, 1.1×10^8, and 2×10^8 cells/mL). Fifty microliters of each B16F10 suspension in PBS were injected (2.5×10^4, 2.5×10^5, 2.5×10^6, 5.5×10^6, and 1×10^7 cells/animal) s.c. into the right hind thigh of female Balb/c mice (20-25 g, Charles River) under isoflurane anesthesia. The tumors were measured and recorded, the volumes were calculated using the equation: Tumor Volume (mm^3) = $0.52\times(\text{width})^2\times\text{length}$.

4.2.4.2 In Vivo Imaging with 74-kD HA-IR820 Conjugate in B16F10 Tumor Bearing Mice

Fifty microliters of a 1.1 × 10^8 cells/mL suspension of B16F10 cells were injected (5.5 × 10^6 cells) s.c. into the right hind thigh of female Balb/c mice (20-25 g, Charles River, n=5) under isoflurane anesthesia (Day 1). All mice were fed a low chlorophyll diet at least one week prior to imaging to decrease food-induced organ and skin autofluorescence (Harlan 2918 irradiated diet). The mouse's hair in the area of interest for imaging was removed 24 h prior to imaging (Day 3) with clippers followed by depilatory cream. On Day 4, mice with similar tumor volumes, shape, and location, were chosen for the imaging study. Three mice were anesthetized under isoflurane, placed on a heating pad to help regulate body temperature, and were injected subcutaneously (s.c.) with 10 μL of a 1.0 mg/mL solution (IR820 dye basis) of 74-kD HA-IR820 (described in Chapter 2) in the center of the right hind footpad. The mice were imaged on both the dorsal and right sides, both with and without the injection site being covered at predetermined time intervals, using whole body fluorescent imaging (Cambridge Research and Instrumentation Maestro multi-spectrum imager, Woburn, MA) using an excitation filter of 710-760 nm and broadpass emission filter of 800-950 nm. The animals were imaged for a maximum of seven days. Images were acquired using the autoexposure function in the imaging software.

Image analysis was performed using Maestro software (ver. 2.10). Regions of interest were placed over the popliteal and iliac lymph nodes. The total signal (scaled counts/s) intensity values (arbitrary units, AU) were recorded for each region of interest (ROI), for both positions (dorsal and right sides), and were plotted versus time in GraphPad Prism (ver. 4). The total fluorescence intensity vs. time graphs were integrated to give the cumulative fluorescence vs. time graphs. In addition, the area under the curve (AUC) was determined from the total fluorescence intensity vs. time graphs.

$$\text{Scaled counts/s} = \text{counts/full scale} \times 1/\exp(s) \times 1/\text{bin}^2 \times 1/\text{gain}$$

4.2.4.3 Anticancer Efficacy in B16F10 Tumor Bearing Mice

Fifty microliters of a 1.1×10^8 cells/mL suspension of B16F10 cells were injected (5.5×10^6 cells) s.c. into the right hind thigh of female Balb/c mice (20-25 g, Charles River) under isoflurane anesthesia.

In the first study, when the B16F10 tumors reached 200-300 mm^3 in size (ca. Days 7-9, n=5), the mice were injected once with melphalan (5 mg/kg) intravenously via the tail veil under isoflurane anesthesia. The formulation used to treat mice bearing B16F10 tumors was modified slightly from the product insert for ALKERAN® (melphalan hydrochloride) for injections into humans. Melphalan (Bosche Scientific) was dissolved in concentrated hydrochloric acid (35-38%) to give a 15 mg/mL solution. The melphalan solution was then aliquoted into vials to give 0.75 mg melphalan/vial, and was dried using a speedvac concentrator (Labconoco) for 1.5 hr at 35°C followed by 1 hr at ambient temperature. The vials containing dry melphalan hydrochloride were sealed and placed at -20°C until further use. The reconstituted solution was prepared by first pre-sterilizing propylene glycol, 95% ethanol, and 0.02 g/mL sodium citrate solution, using a sterile syringe fitted with a 0.22 μm sterile filter (Millex GP PES membrane sterile filter, Millipore) into a sterile falcon tube. Then the reconstituted solution was prepared by combining 6 mL sterile propylene glycol, 0.52 mL sterile ethanol (95%), and 3.48 mL sodium citrate solution, and the solution was mixed well and filtered a second time with at 0.22 μm sterile filter. Immediately prior to injection, the 150 μL of the sterile reconstituted solution was rapidly added to the melphalan hydrochloride, the vial was immediately shaken vigorously until dissolved, followed by the rapid addition of 150 μL of sterile saline yielding a 2.5 mg/mL melphalan solution. The melphalan was dosed within 10 to 15 min after reconstitution to minimize degradation.

In the second study, when tumors reached 200-350 mm^3 (Days 6-9), mice were randomly divided into four groups and injected with 17-DMAG (i.v., n=4), Star-GA (s.c., n=7), 60% acid-star polymer (s.c., n=6), or no treatment (n=4). The 17-DMAG was dissolved in sterile DMSO and administered i.v. via the tail vein at a dose of 15 mg/kg (MTD). Star-GA was dissolved in a 1:1 mixture of DMSO:PBS, and the pH was adjusted to ca. 5.7 with NaOH, giving a Star-GA solution in 30% sterile DMSO and 70% sterile PBS, the Star-GA solution was administered at an equivalent dose to the 15 mg/kg 17-DMAG (13.64 mg/kg 17-HEAG, 15 wt% loading, i.e. 90.93 mg/kg total conjugate) with one peritumoral injection. Finally, the 60% acid-star polymer was dissolved in sterile PBS and the pH was adjusted to 5.4 with 2-M sterile NaOH, the 60% acid-star polymer was then administered at an equivalent polymer dose to the Star-GA (i.e. 77.29 mg/kg star polymer) with one peritumoral injection.

4.2.5 4T1.2 Neu Murine Breast Cancer Tumor Model

The 4T1.2 Neu, was maintained in DMEM supplemented with 1% L-Glutamine, 10 % bovine growth serum, and 500 μg/mL of G418 (geneticin) in 5% CO_2 atmosphere. During cell preparation of the 4T1.2 Neu cells for implantation, G418 free media was used. Dr. Cai previously optimized the in vivo tumor growth of the 4T1.2 Neu cell line in Balb/c mice. Prior to tumor implantation, the hair surrounding the right upper portion of the mouse's chest was removed with depilatory cream. Female Balb/c mice (20-25 g, Charles River) were injected in the first mammary fat pad on the right side with 50 μL of a 2×10^7 cell/mL suspension in 1× PBS (1×10^6 4T1.2 Neu cells/animal) under isoflurane anesthesia (Day 1).

4.2.5.1 Anticancer Efficacy Pilot Study in 4T1.2 Neu Tumor Bearing Mice

Seven 4T1.2 Neu tumor-bearing mice were randomly divided into three treatment groups, once the tumors reached ca. 200 mm^3 (Day 9-10), including 17-DMAG (n=2), Star-GA (n=3), and no treatment (n=2). The 17-DMAG was dissolved in sterile DMSO and administered via the tail vein at a dose of 10 mg/kg (MTD is 15 mg/kg). Star-GA was dissolved in a 1:1 mixture of DMSO:PBS, and the pH was adjusted to 6.8 with NaOH, giving a Star-GA solution in 30% sterile DMSO and 70% sterile PBS, the Star-GA solution was administered at an equivalent dose to the 10 mg/kg 17-DMAG (9.56 mg/kg 17-HEAG, 15 wt% loading, i.e. 63.74 mg/kg total conjugate) divided into two peritumoral injections on either side of the mammary tumor.

4.2.5.2 Increased Maximum Tolerable Dose (MTD) of Star-GA

Four healthy female Balb/c mice (20-25 g, Charles River) were randomly divided into two groups and were dosed with two s.c. injections on either side of the first nipple on the right side with either 30 or 50 mg/kg Star-GA (17-HEAG basis, 31 wt% loading) in 30% DMSO and 70% PBS. Mice were monitored for at least one week for signs of toxicity, including losses in body weight, rough coat, fecal/urine soiling of the coat, diarrhea or dehydration, abnormal breathing patterns, or self-isolation.

4.2.5.3 Anticancer Efficacy in 4T1.2 Neu Tumor Bearing Mice

Seven week old (18-22 g) female Balb/c mice purchased from Jackson Laboratory (Bar Harbor, Maine) were used in this study. On Day 7, when tumors reached 100-250 mm^3, mice were randomly divided into four treatment groups, consisting of no treatment (n=7), 60% acid-star polymer (n=5), 17-DMAG (n=7), and Star-GA (n=8). The 17-DMAG was dosed at 10 mg/kg i.v. as a 1:1 sterile DMSO:PBS solution. Star-GA was dosed at 45 mg/kg (17-HEAG basis, 15% loading, 300 mg/kg Star-GA conjugate), in sterile 35% DMSO and 65% PBS, which was divided into two peritumoral injections on either side of the mammary tumor. Finally, the 60% acid-star polymer was dosed at an equivalent star polymer concentration used for the 45 mg/kg Star-GA (255 mg/kg 60% acid-star polymer), which was divided into two peritumoral injections onto either side of the mammary tumor. Tumor volumes were monitored and reported every two days.

4.2.5.4 Metastatic Analysis of Axillary Lymph Nodes by Nodal Volume and Real Time Polymerase Chain Reaction (rtPCR)

The metastatic state of the 4T1.2 Neu tumor model post treatment was assessed by axillary lymph node volume and the nodal HER 2 expression. The visible axillary lymph nodes on the right side were harvested from mice in each treatment group (17-DMAG, 60% acid-star polymer, Star-GA, and no treatment, dosing for each treatment group described in *Section 4.2.5.3*) once the mice reached a humane endpoint, i.e., tumor volume > 2000 mm^3, body score index of 1, or signs of necrosis or toxicity. The mice were euthanized and the nodes were flash frozen and stored at -80°C until real-time PCR (rtPCR) analysis. The lymph nodes were measured with digital calipers and the axillary lymph node volumes were calculated using the same equation used to calculate tumor volume, i.e. volume = $0.52 \times (\text{width})^2 \times (\text{length})$.

The rtPCR analysis was conducted by our collaborator, Dr. Li, at the University of Kansas Medical Center. Briefly, the total RNAs from the frozen lymph node samples were extracted using TriZol reagent (Invitrogen). The first-strand cDNA was synthesized using the Omniscript-RT Kit (QIAGEN, Valencia, CA). Primers for the Erbb2 (HER2 RT^2 qpCR primer assay, proprietary primer sequence, QIAGEN) and 18S housekeeping gene (forward: 5'-GGGAGGTAGCGAAAAATAACAA-3' reverse: 5'-CCCTCCAATGGATCCTCGTT -3') (IDT Inc, Coralville, IA) were used. The real-time PCR, in a reaction volume of 25 μL, was performed using the SYBR Green Supermix kit with the Bio-Rad iQ5 system (Hercules, CA). Denaturation at 95 °C for 15 s and annealing/extension (temperature varied due to different primer sequence and composition) for 1 min was performed for 40 cycles.

4.2.6 A2058 Human Melanoma Tumor Model

The lymphatically metastatic human melanoma cell line, A2058, was purchased from ATCC, and was maintained in low sodium bicarbonate containing DMEM supplemented with 1% L-Glutamine, 10% bovine growth serum in 5% CO_2 atmosphere. Female nude mice (20-25g, Charles River) were implanted s.c. in the right hind thigh with 50 μL of 4×10^7 cells/mL (n=2, 2×10^6 cells/animal), 1×10^8 cells/mL (n=1, 5×10^6 cells/animal), 1.5×10^8 cells/mL (n=1, 7.5×10^6 cells/animal), or 2×10^8 cells/mL (n=1, 1×10^7 cells/animal) of A2058 cells in sterile PBS under isoflurane anesthesia in this pilot study. Tumors were monitored at least twice weekly using digital calipers in a laminar flow hood.

Of the three mice with palpable tumors, once the tumors reached 200-300 mm^3, the mice were divided into three treatment groups: no treatment (2×10^6 cell/animal mouse), i.v. 10 mg/kg 17-DMAG (1:1 DMSO:PBS, 2×10^6 cell/animal mouse), and peritumorally 20 mg/kg Star-GA (17-HEAG basis, 30:70 DMSO:PBS, 1×10^7 cell/animal mouse).

4.3 Results

4.3.1 Synthesis and Characterization of the Star-Geldanamycin Conjugate

The degree of conjugation of 17-HEAG to the star polymer was determined to be 15 wt% by ^{1}H-NMR (Bruker, 400MHz) in MeOD and 14.8 wt% by UV spectroscopy (SPECTRA MAX PLUS, Molecular Devices) at 330 nm using a standard calibration curve (1-30 µg/mL). The conjugation degree was determined by comparing the ratio of the proton on the C19 position of the benzoquinone ring with repeating unit proton of the star polymer from the ^{1}H-NMR spectra. A series of 17-HEAG concentrations were prepared from a stock solution of 17-HEAG in MeOH. The concentrations used for the standard curve of 17-HEAG were 1, 2, 5, 8, 10, 20, and 30 µg/mL (R^2=0.997) in MeOH. The absorbance of the star-GA was measured at 330 nm, and the resulting absorbance measurements were due to 17-HEAG and not the star polymer (Figure 4.1), as the star polymer does not exhibit UV absorbance at 330 nm. The loading degree of 17-HEAG was calculated to be 14.8 % (wt/wt); and the same star-GA batch was used for all experiments unless otherwise noted.

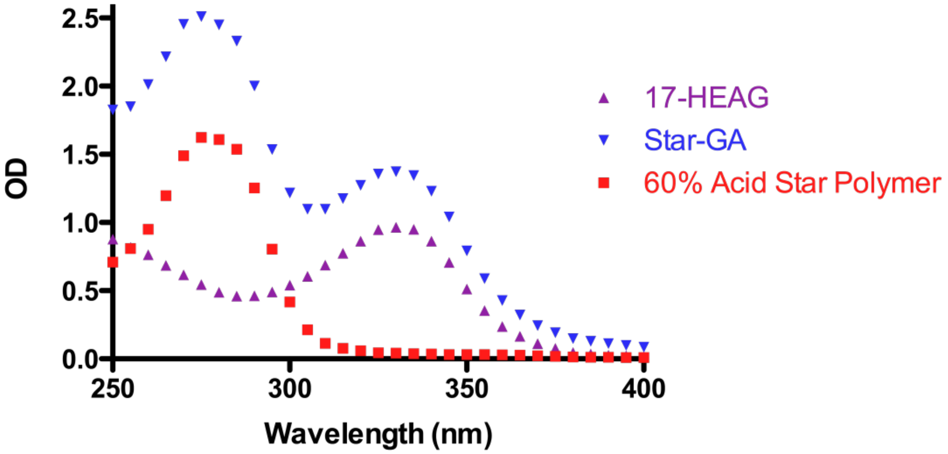

Figure 4.1. UV absorbance spectra of 17-HEAG, 60% acid-star-polymer, and star-GA conjugate in methanol. (Note: sample concentrations were not held constant, thus the relative intensities cannot be compared).

4.3.2 In Vitro Cytotoxicity

The calculated IC_{50} values for geldanamycin, 17-DMAG, 17-AAG, 17-HEAG, star-GA, 60% acid-star polymer, and melphalan, in the B16F10, A2058, HUVEC, 4T1.2 Neu, and MDA-MB-231 cell lines are presented in Table 4.1. Melphalan was compared to the geldanamycin analogues in melanoma cell lines, as it is used clinically with ILP treatment for melanoma. Geldanamycin and its derivatives exhibited similar cytotoxicity in the B16F10 and 4T1.2 Neu murine cell lines. The HUVEC and MDA-MB-231 cell lines were investigated to compare the cytotoxicities observed in the B16F10, A2058, and 4T1.2 Neu cell lines to human cell lines for normal cells and human breast cancer, respectively. In the B16F10 cell line, the 17-HEAG analogue exhibited similar cytotoxic effects as the parent drug GA. Similarly, in the A2058 human melanoma cell line the star-GA conjugate exhibited less *in vitro* toxicity than GA, 17-DMAG, and 17-AAG; however, it was two orders of magnitude more toxic than melphalan. All of the GA analogues and the star-GA exhibited similar toxicities in the 4T1.2 Neu HER2 expressing murine breast cancer cell line.

IC_{50} values (μM)

	B16F10	A2058	HUVEC	4T1.2 Neu	MDA-MB-231
Geldanamycin	0.035	0.044	0.440	0.260	0.960
17-DMAG	0.250	0.044	29	0.296	0.200
17-AAG	0.450	0.053	64	0.315	------
17-HEAG	0.038	49	0.550	0.422	------
Star-GA	4.2	0.700	1.4	0.335	0.580
60% acid-star	>100	~60	~100	~100	≥100
Melphalan	103	30	209	------	------

Table 4.1. Corresponding IC_{50} values (μM) for geldanamycin, 17-DMAG, 17-AAG, 17-HEAG, star-GA, 60% acid-star polymer, and melphalan in B16F10, A2058, HUVEC, 4T1.2 Neu, and MDA-MB-231 cell lines (n=8-12). The data for the 60% acid-star polymer is reprinted from Table 3.2 from Chapter 3 for data completion.

4.3.3. In Vitro Release

The star-GA conjugate was synthesized utilizing an ester linkage, the release of 17-HEAG from the star polymer platform is achieved by the hydrolysis of the ester bond. The release samples were analyzed on a UV plate reader with the 17-HEAG standard curve. A series of 17-HEAG concentrations in PBS were prepared from a stock solution of 17-HEAG. The concentrations used for the establishment of the 17-HEAG standard curve were 0.8, 1, 2, 4, 6, 8, 10, 20, 40, 60, and 80 μg/mL (R^2=0.999). The 17-HEAG concentrations for the release samples at each time point were calculated from the standard curve and were normalized to account for the change in concentration due to sampling and osmosis, and were reported as the fraction of bound GA remaining in the dialysis bag. The fraction of GA bound to the star polymer as a function of time is illustrated in Figure 4.2; the data was then fitted to a one-phase exponential decay function (GraphPad Prism 10) with a release half-life of 4.12 ± 0.35 hr (R^2=0.99).

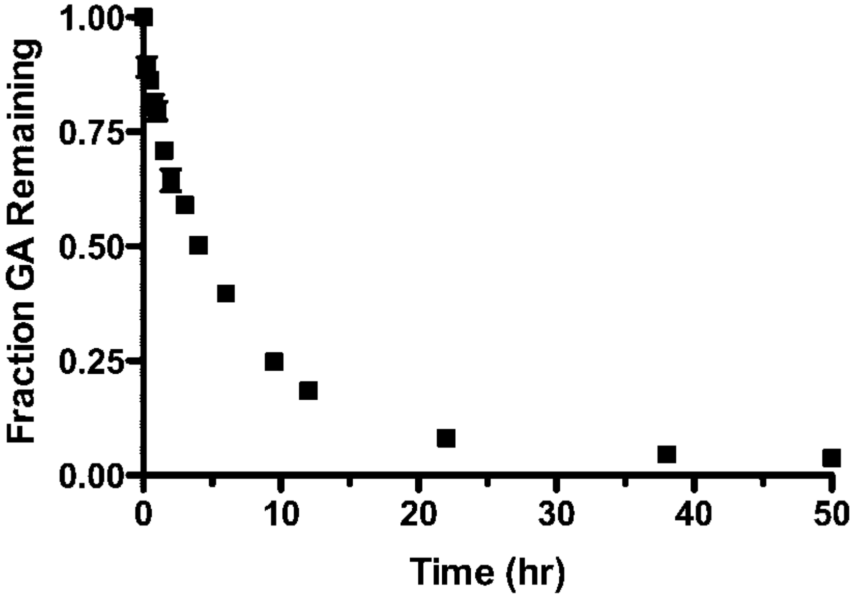

Figure 4.2. Release kinetics of 17-HEAG from the star-GA conjugate in PBS at 37°C (n=3).

4.3.4 B16F10 Murine Melanoma Tumor Model

4.3.4.1 B16F10 Murine Melanoma Tumor Model Optimization

The tumor growth curves for the different concentrations of B16F10 cells that were injected into Balb/c mice are illustrated in Figure 4.3. None of the mice injected with 2.5×10^4 cells/animal (n=4) developed tumors after 48 days (data not shown). Two of the four mice that were implanted with 2.5×10^5 cells/animal developed tumors within two weeks, however the tumor size did not change significantly within three weeks; while the other two mice in the group did not develop tumors within three weeks. The lack of tumor growth over the three week monitoring timeframe, suggests that the "observed tumor" was merely a cell depot that was visualized by the discoloration due to the over-expression of melanin in the B16F10 cells and was not the development of a palpable tumor. All of the mice implanted with 2.5×10^6 cells/animal (n=5) developed tumors by day 11 post implantation, however, the tumor growth was very slow and inconsistent among the five mice. By day 30, one mouse had a tumor of 25 mm^3, another with a 3800 mm^3 tumor, while the remaining three mice developed tumors ca. 1000 mm^3. Similarly, all mice injected with 1×10^7 cells/animal (n=3) developed tumors that appeared to grow steadily; however, their tumor growth was inconsistent. In contrast, all of the mice injected with 5.5×10^6 cells/animal (n=8) developed tumors within three days post-implantation, which grew at a constant and consistent rate. The 5.5×10^6 cells/animal concentration was selected as the optimal cell concentration for future studies.

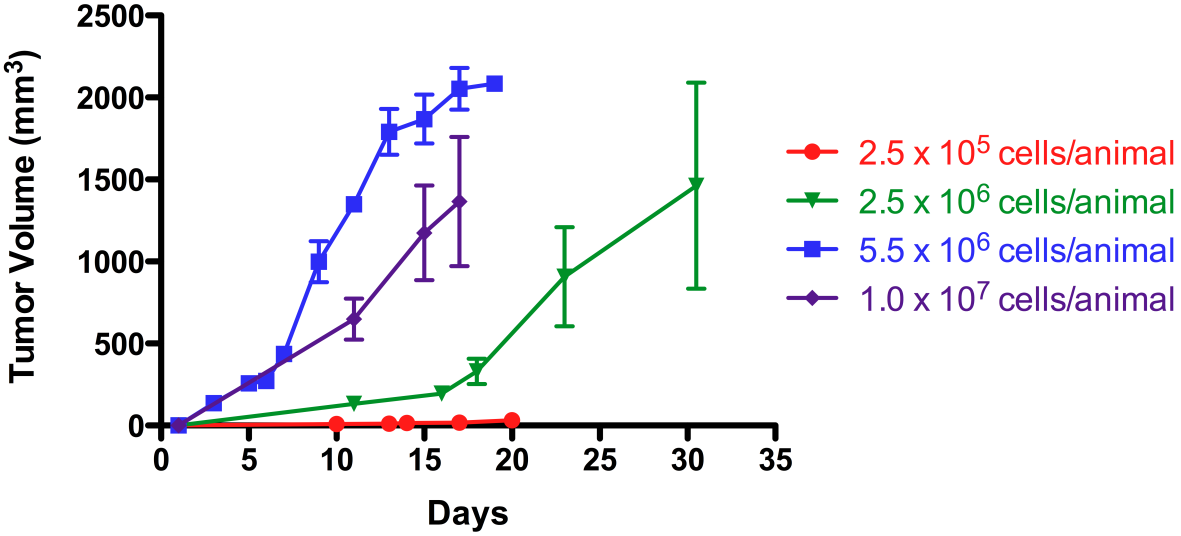

Figure 4.3. Tumor growth curves for mice implanted with (2.5×10^5, 2.5×10^6, 5.5×10^6, and 1×10^7 cells/animal) s.c. in the right hind thigh of Balb/c mice.

4.3.4.2 Effect of B16F10 Tumors on the In Vivo Lymphatic Drainage of 74-kD HA-IR820 using In Vivo Fluorescence Imaging

Mice in the footpad injection group were imaged from both their right and dorsal sides to detect drainage into the popliteal and iliac nodes. The same trends were observed for both imaging positions; but the right side was analyzed as it produced greater signal intensities and a higher signal to noise ratio compared to the dorsal or ventral positions. The ventral position led to a decreased signal to noise ratio due to the increased fluorescence contributions of the organs in the abdomen, along with the inability to visualize the iliac node due to its increased depth in this position. The intense fluorescence signal from the injection site led to saturation of the camera, to circumvent such signal saturations, the injection site was covered allowing visualization of the draining lymphatic vessels and lymph nodes. Both the lymph nodes and draining lymphatic vessels were clearly visualized against the background tissues using fluorescent imaging (Figure 2.3A found in Chapter 2) with the injection site covered. The use of the autoexpose function resulted in different exposure times for each image, which were corrected for in the image analysis where the scaled counts/s normalizes for the exposure time. Due to the limitations of in vivo fluorescence imaging (ca. 1 cm), only shallow nodes were identified; the authors do not discount further drainage of the 74-kD HA-IR820 conjugate past the iliac node.

The lymphatic drainage data for the 74-kD HA-IR820 in normal, non-tumor bearing mice is reproduced from Chapter 2, and is presented here for comparison with the lymphatic drainage after s.c. administration of the 74-kD HA-IR820 in mice bearing a B16F10 murine melanoma tumor.

We examined the effect of a B16F10 melanoma tumor on the lymphatic drainage of both the popliteal (Figures 4.4 A and C) and iliac nodes (Figures 4.4 B and D) using the optimized 74-kD HA-IR820 conjugate. A significant difference was observed in the kinetic profiles for the lymphatic drainage to the popliteal node between the tumor bearing and normal mice ($p=0.0320$, student t-test)(Figure 5A); however, there were no significant differences in the AUC for the popliteal nodes between the two groups (Table 4.2). The drainage from the popliteal node in tumor-bearing mice was almost three times slower than in the normal mice ($t_{50\%}$ of 20 and 6.9 hrs, respectively), whereas the drainage to the iliac node remained unchanged ($t_{50\%}$ of 23 hrs and 21 hrs, respectively) (Figures 4.4A and B, Table 4.2). Furthermore the t_{max} in the popliteal and iliac nodes was unchanged for tumor-bearing mice compared to normal mice (Table 4.2).

Lymph Node	Animal	t_{max} (hr)	$t_{50\%}$ (hr)	AUC (AU)
Popliteal	B16F10 Tumor	2	20	7597±1039
	Normal	1.5-2	6.9	11464±3318
Iliac	B16F10 Tumor	2	23	3086±171
	Normal	1.5-2	21	3627±1644

Table 4.2. t_{max}, $t_{50\%}$, and AUCs for the popliteal and iliac nodes after s.c. administration of 74-kD HA-IR820 into the footpad of normal and B16F10 tumor bearing mice.

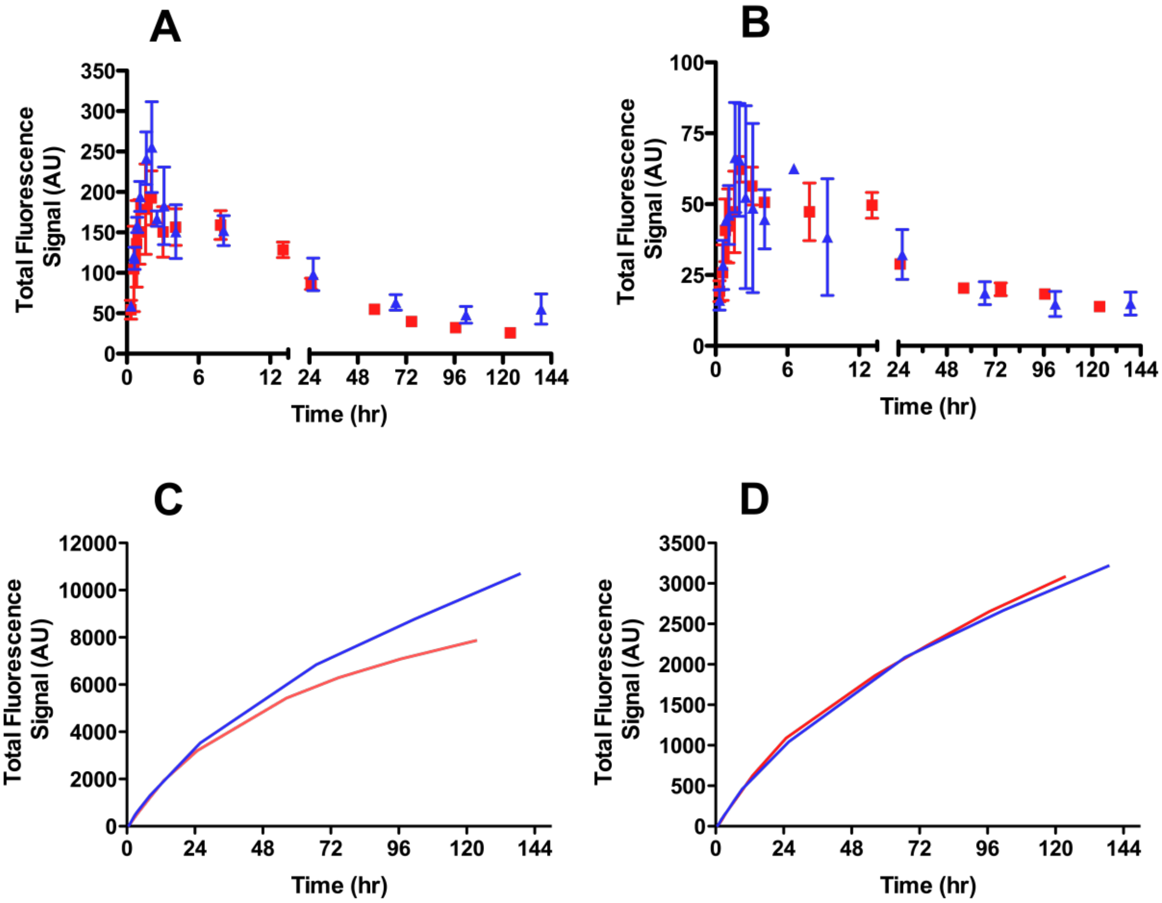

Figure 4.4. Lymphatic drainage kinetics of the 74-kD HA-IR820 into the A) popliteal and B) iliac lymph nodes in normal (blue triangles) and B16F10 tumors bearing mice (red squares). Cumulative drainage of the 74-kD HA-IR820 conjugate vs. time to the C) popliteal and D) iliac lymph nodes in normal (blue line) and B16F10 tumor bearing mice (red line).

4.3.4.3 In Vivo Treatment Efficacy with Melphalan in the B16F10 Murine Melanoma Tumor Model

Mice bearing B16F10 tumors with no treatment exhibited extremely rapid tumor growth, which reached 2000 mm^3 within 19 days post implantation (Figure 4.5). On the contrary, mice treated with i.v. melphalan exhibited a complete response to treatment (p=0.0068, two-tailed unpaired t-test), with signs of tumor regression within two days post-treatment (Figure 4.5). Melphalan treated mice did not exhibit a relapse in tumor growth over the time course of the study.

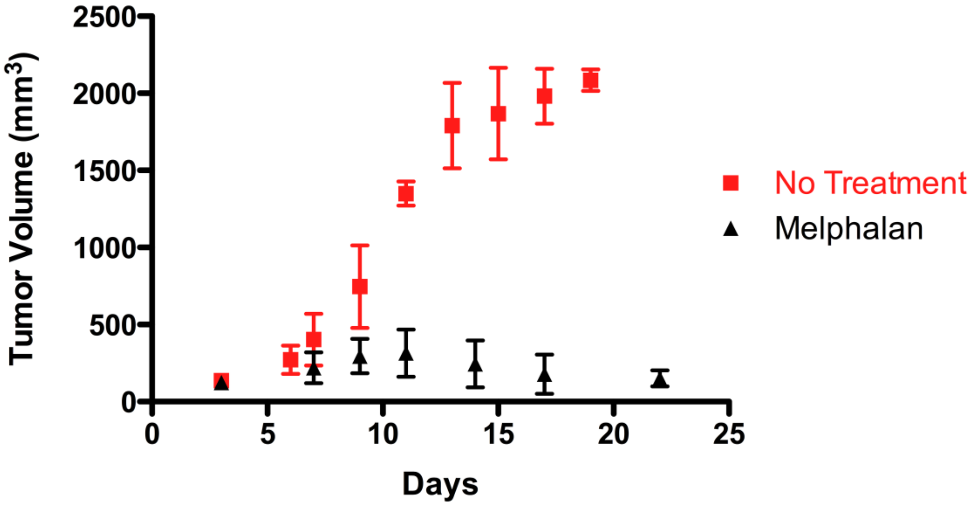

Figure 4.5. B16F10 tumor growth with and without melphalan treatment (5 mg/kg, i.v.), (n=4, no treatment, n=3 melphalan treatment). (p=0.0068)

4.3.4.4 In Vivo Treatment Efficacy with 17-DMAG and Star-GA in the B16F10 Murine Melanoma Tumor Model

Mice bearing B16F10 tumors did not exhibit any statistically significant responses in the inhibition of tumor growth with all treatment groups, 17-DMAG, star-GA, or 60% acid-star polymer, in comparison to no treatment (Figure 4.6 A). Although 17-DMAG and star-GA treatments demonstrated a 400-fold and 24-fold, respectively, increase in toxicity compared to melphalan in the B16F10 cell line *in vitro* (Table 4.1), the *in vivo* B16F10 tumors did not respond to either GA-based treatment, while treatment with melphalan exhibited a statistically significant efficacious response in B16F10 tumors (p=0.0068, Figure 4.5). Further, the star-GA treatments led to a decrease in the mouse's body weight, compared to an increase in body weight seen with mice with both the 60% acid-star polymer and non-treated groups (Figure 4.6 B). However, the loss in body weight after treatment with star-GA was not observed until day 23, which corresponds to only one animal with a decrease in its body weight, and was not statistically significant. The remainder of the mice in the star-GA treatment group did not exhibit more than ±5% change in body weight, whereas the one mouse had a 14% decrease in body weight post-treatment (Figure 4.6 B). No physical signs of toxicities were seen with either the star-GA or 60% acid-star treatments; however, all mice treated with i.v.17-DMAG displayed signs of severe tail necrosis, possibly due to extravasation of either DMSO or 17-DMAG into the subcutaneous space of the tail. Although 17-DMAG has increased water solubility compared to the parent drug, GA, the concentrations required for a 15 mg/kg dose and an injection volume of ca. 50 μL i.v. exceeded the water solubility of 17-DMAG, thus the need for DMSO for the injection of 17-DMAG.

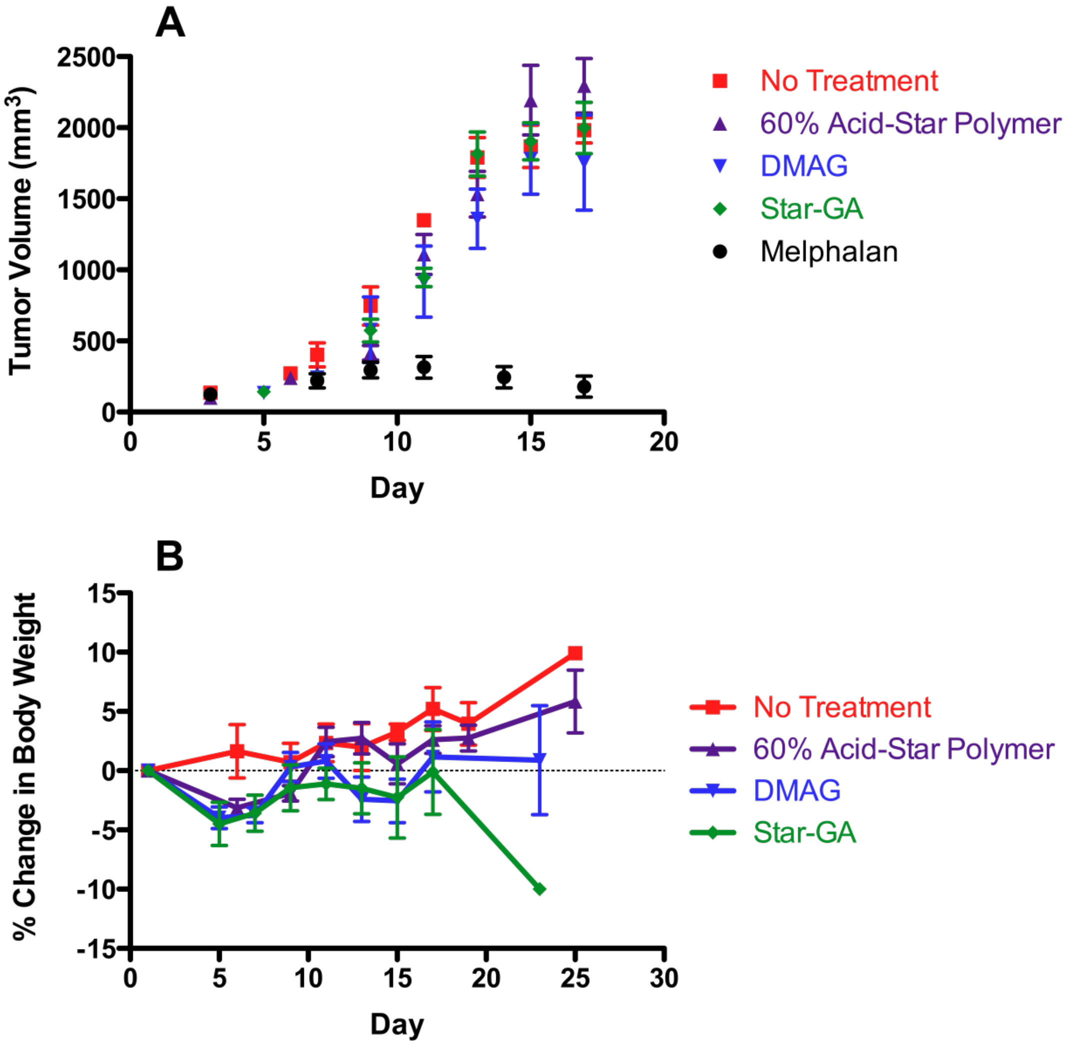

Figure 4.6. A) B16F10 tumor growth in response to no treatment (red, n=4), 60% acid-star polymer (s.c. equivalent star polymer dose to star-GA, purple, n=6), 17-DMAG (i.v. 15 mg/kg, blue, n=4), star-GA (s.c. 15 mg/kg DMAG equivalent, green, n=7), or melphalan treatment (i.v. 5 mg/kg, black, n=3). B) Percent change in body weight in response to no treatment (red, n=5), 60% acid-star polymer (s.c., purple, n=7), 17-DMAG (i.v., blue, n=7), or star-GA (s.c., green, n=8).

4.3.5 4T1.2 Neu Murine Breast Cancer Tumor Model

4.3.5.1 *In Vivo Treatment Efficacy with 17-DMAG and Star-GA in the 4T1.2 Neu Murine Breast Cancer Tumor Model - Pilot Study*

At the end of the pilot study, when the tumors reached ca. 2000 mm^3, no statistical significances were observed between the three treatment groups (no treatment, i.v. 17-DMAG, and s.c. star-GA, Figure 4.7). However, on day 17, there was a statistically significant difference in the tumor sizes in the three treatment groups; both the 17-DMAG and star-GA treatment groups exhibited significant delay in tumor growth in comparison to the non-treated group ($p<0.005$, one-way ANOVA with a Tukey's Multiple Comparison post test) (Figure 4.7). Further analysis with a larger number of animals per treatment group was required to further characterize the treatment of 17-DMAG and star-GA in 4T1.2 Neu tumor bearing mice. The study was repeated with larger treatment groups, with the addition of the free 60% acid-star polymer. Additionally, no visual signs of toxicity from the star-GA conjugate at either 10 or 15 mg/kg (17-DMAG equivalent) doses were observed.

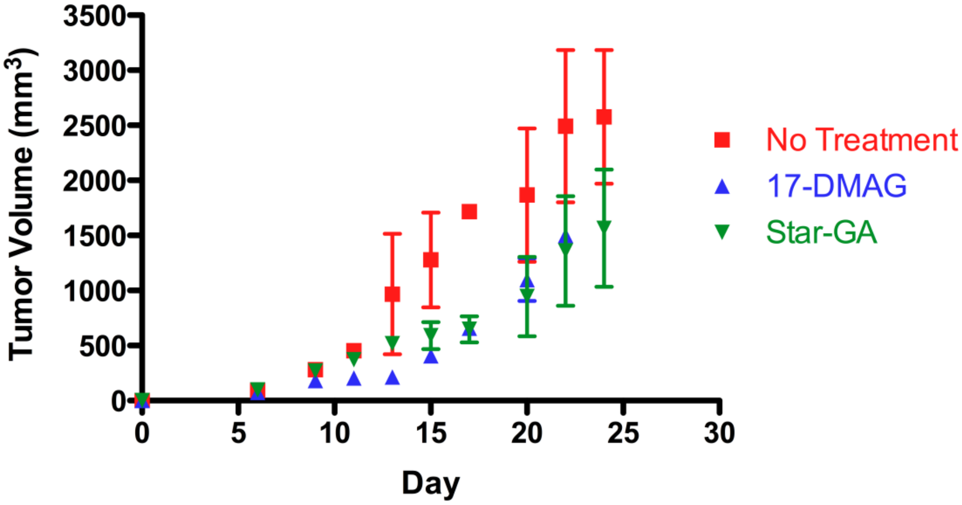

Figure 4.7. 4T1.2 Neu tumor growth in a pilot study after treatment with 17-DMAG (i.v., 10 mg/kg, n=2), star-GA (s.c., 10 mg/kg 17-DMAG equivalent, n=3), and no treatment (n=2).

4.3.5.2 Increased Maximum Tolerable Dose (MTD) of Star-GA

In both the 4T1.2 pilot study and the B16F10 efficacy studies, star-GA was dosed at an equivalent GA dose as the observed 17-DMAG MTD (10 and 15 mg/kg, respectively). We investigated the potential for increasing the MTD of the star-GA with respect to 17-DMAG. For doses of 30 and 50 mg/kg star-GA (17-HEAG basis), no visual signs of toxicity were observed with either treatment group within one week post treatment. Further, after three weeks post dosing, no visual signs of toxicity were observed. Dose escalation studies above 50 mg/kg were not investigated, however, it is possible that the MTD of the star-GA conjugate is higher than 50 mg/kg, on a 17-HEAG basis. Subsequent studies using the 50 mg/kg star-GA (17-HEAG basis) dose was evaluated for the treatment of 4T1.2 tumor model along with an increase in the number animals per treatment group.

4.3.5.3 In Vivo Treatment Efficacy with 17-DMAG and Star-GA in the 4T1.2 Neu Murine Breast Cancer Tumor Model

In the pilot study with 4T1.2 Neu tumor model, 17-DMAG was dosed at 10 mg/kg i.v. in 100% DMSO, however in this study it was administered as a 1:1 sterile DMSO:PBS solution to minimize possible toxicities due to the administration of intravenous DMSO. A dose of 45 mg/kg was used in contrast to the 50 mg/kg used in the MTD study, due to solubility issues and limited quantities of the star-GA conjugate.

Although the MTD of the star-GA conjugate was increased from 15 mg/kg 17-DMAG to at least 45 mg/kg 17-HEAG by utilizing the star-GA conjugate, no statistically significant increases in efficacy were observed by a delay in tumor growth (Figure 4.8 A). Further increases in the survival (Figure 4.8 B) of mice were also not observed with the star-GA conjugate compared to both non-treated and i.v. 17-DMAG treatment groups. In fact, no statistical significances were seen with regards to the tumor response for all three of the treatment (star polymer alone, 17-DMAG, or star-GA) compared to the non-treated mice (Figure 4.8 A). In addition, neither 17-DMAG nor star-GA treatments exhibited an increase in survival (Figure 4.8 B). Further, all but two mice, one treated with the 60% acid-star polymer and the other treated with the star-GA conjugate, exhibited an increase in body weight throughout the duration of the study (Figure 4.8 E). The two aforementioned mice exhibited a decrease in body weight coupled with a significant decrease in body score (body score of 1 or lower). A body score of 1 is representative of a mouse that appears to be "emaciated, with a prominent skeletal structure with little flesh covering, and distinctly segmented vertebrae [45]." The cause of the low body score in these two mice was not investigated further.

4.3.5.4 Metastatic Analysis of Axillary Lymph Nodes by Nodal Volume and Real Time Polymerase Chain Reaction (rtPCR)

In order to assess the metastatic state of the 4T1.2 Neu tumor model, after treatment with 17-DMAG, 60% acid-star polymer, star-GA, or no treatment, the visible axillary lymph nodes on the right sides of the mice were harvested, measured, and analyzed by rtPCR. During the lymph node harvesting, gross visualization of the organs was made to identify any obvious signs of metastases, growths, or toxicities associated with any of the treatments.

All of the mice with 4T1.2 Neu tumors exhibited significantly enlarged spleens of at least twice the size of a normal mouse's spleen. The mouse treated with star-GA (referred to in the previous section, *4.3.5.3*) with the low body score also appeared to have lung metastases and possible cardiac disease. One mouse that did not receive treatment also exhibited signs of cardiac disease. Finally, one mouse treated with the 17-DMAG appeared to have liver metastases. Before the lymph node samples were analyzed for HER2 expression by rtPCR to assess their metastatic state, the lymph nodes were measured with digital calipers and the axillary lymph node volumes were calculated using the same equation used to calculate tumor volume = $0.52 \times (\text{width})^2 \times (\text{length})$. Although there are noticeable differences in the axillary lymph node volumes in Figure 4.8 C, these differences are not statistical significant.

Typically when analyzing rtPCR data the amplification value of the target gene, HER2, would be normalized against the 18S housekeeping gene, however, the HER2 expression was very low in all of the axillary lymph node tissue samples for all treatment groups indicated by the average cycle threshold value of ca. 35 (Figure 4.8 D); indicating that the axillary lymph nodes did not have HER2 expressing metastases. One animal in the star-GA treatment group did present a cycle threshold of ca. 29 for the HER2 expression; however, there were no statistically significant differences between the different treatment groups.

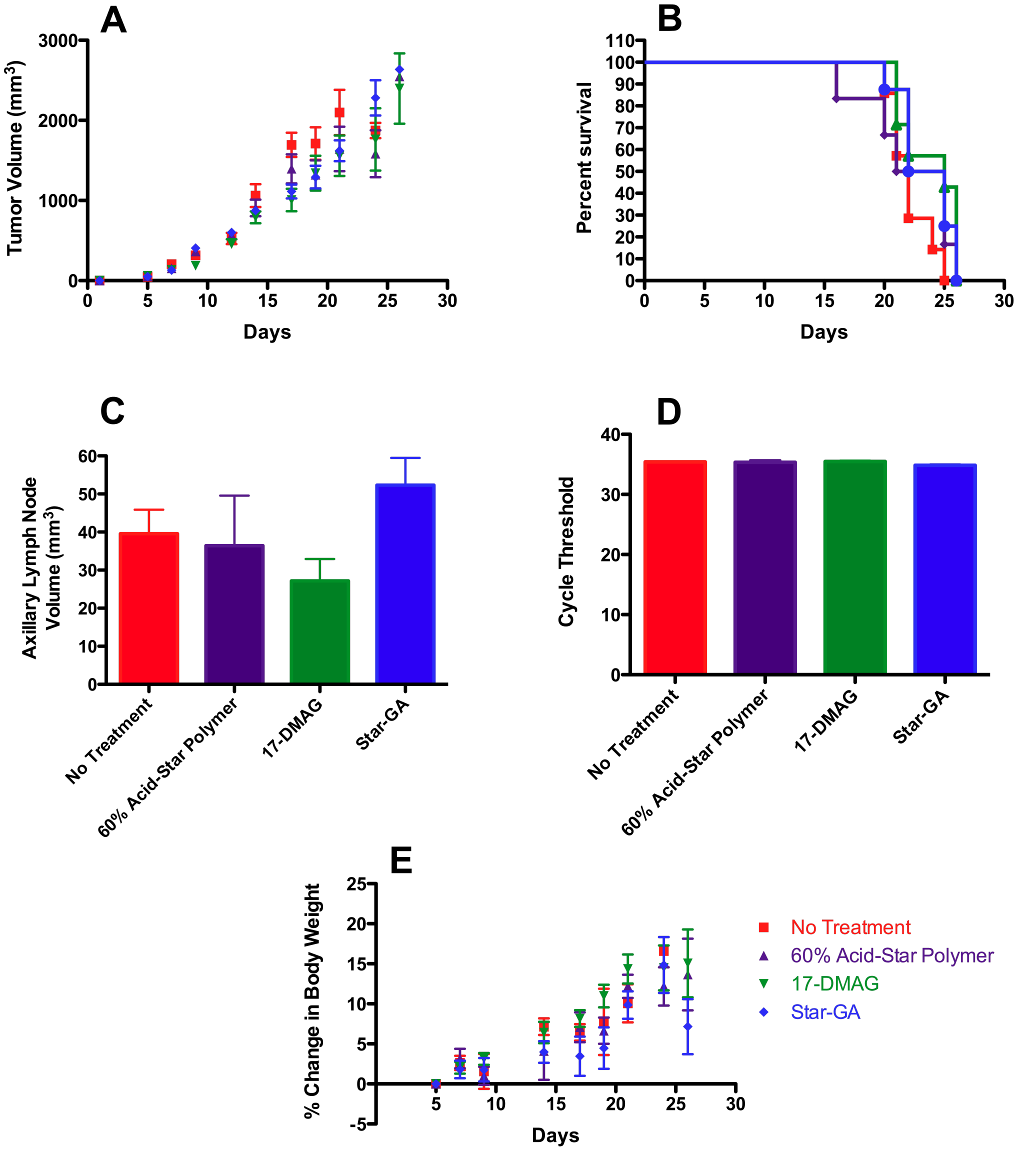

Figure 4.8. A) 4T1.2 Neu tumor growth in mice treated with 17-DMAG (i.v., 10 mg/kg, n=7) (green inverted triangles), star-GA (s.c., 45 mg/kg 17-DMAG equivalent, n=8) (blue diamonds), 60% acid-star polymer (s.c., equivalent star polymer dose to 45 mg/kg Star-GA, n=7) (purple triangles), and no treatment (n=7) (red squares). B) 4T1.2 Neu survival curve after treatment with 17-DMAG (green inverted triangles), star-GA (blue diamonds), 60% acid-star polymer (purple triangles), and no treatment (red squares). C) Right axillary lymph node volumes from mice treated with 17-DMAG (green), star-GA (blue), 60% acid-star polymer (purple), and no treatment (red) after primary tumors reached 2000 mm^3. Axillary lymph node volume = 0.52×(width)^2×(length). D) Metastatic assessment of HER2 expression in axillary lymph nodes from mice treated with 17-DMAG (green), star-GA (blue), 60% acid-star polymer (purple), and no treatment (red) by rtPCR, representative cycle threshold values for HER2 expression in each treatment group. E) Percent change in body weight in mice bearing 4T1.2 Neu tumors after treatment with 17-DMAG (green inverted triangles), star-GA (blue diamonds), 60% acid-star polymer (purple triangles), and no treatment (red squares).

4.3.6 A2058 Human Melanoma Tumor Model Optimization and Efficacy with 17-DMAG and Star-GA – Pilot Study

The two mice implanted with 2×10^6 A2058 cells both developed primary melanoma tumors within two weeks, and both tumors continued to progress throughout the length of the study. The mouse implanted with 5×10^6 cells developed a primary tumor in the inguinal lymph node by day 14, however, once the tumor reached ca. 100 mm^3 on day 19, the mouse's body condition decreased and the mouse was euthanized. The mouse implanted with 7.5×10^6 cells developed a tumor within one week, and it continued to grow to ca. 100 mm^3 by the end of the second week; however, the tumor then disappeared and the mouse did not develop another palpable tumor within one month post implantation. Finally, the mouse implanted with 1×10^7 cells developed a visible tumor by day 5, which continued to grow throughout the length of the study. Of the five mice implanted with A2058 human melanoma cells, four developed palpable tumors, however, only three mice survived through the end of the study (2 mice implanted with 2×10^6 cells and 1 mouse implanted with 1×10^7 cells).

Of the three aforementioned mice with palpable tumors, the mice were divided into three treatment groups once the tumors volumes reached 200-300 mm^3. The treatment groups were as follows: no treatment (2×10^6 cell/animal mouse), i.v. 10 mg/kg 17-DMAG (1:1 DMSO:PBS, 2×10^6 cell/animal mouse), and s.c. 20 mg/kg star-GA (17-HEAG basis, 30:70 DMSO:PBS, 1×10^7 cell/animal mouse). As with the other two in vivo models, neither 17-DMAG nor star-GA exhibited efficacy in the A2058 tumor model (Figure 4.9). It is worth noting that the mouse treated with star-GA did show a slight decrease in tumor volume for a few days post treatment, however, the tumor continued to grow rapidly after the slight tumor recession (Days 16-20).

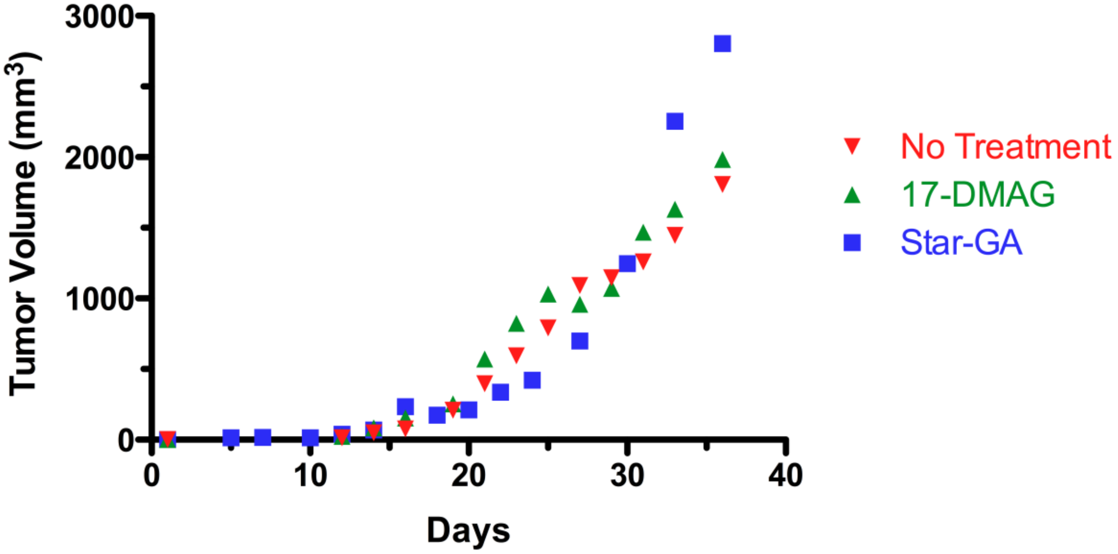

Figure 4.9. A2058 tumor growth in a pilot study after treatment with 17-DMAG (i.v., 10 mg/kg, n=1), star-GA (s.c., 20 mg/kg 17-HEAG equivalent, n=1), and no treatment (n=1). Mice treated with 17-DMAG and no treatment were implanted with 2×10^6 cell/animal; the mouse treated with star-GA was implanted with 1×10^7 cell/animal.

4.4 Discussion

4.4.1 In Vitro Characterization

The procedure for the synthesis of the 17-((2-hydroxyethyl)amino)-17-demethoxygeldanamycin analogue (17-HEAG) was modified from Tian et al. [41]. The loading degree of 15% wt/wt of 17-HEAG on the star polymer limited the water solubility of the conjugate to a minimum requirement of 30% DMSO for solubilization at the concentrations needed for treatment. Higher loading degrees of 27 and 31 % were also synthesized, however these conjugates were not continued with due to the lack of water solubility even in high DMSO concentrations.

The overexpression of HSP90 in malignant melanoma [43,46] combined with the inhibition of HSP90 resulting in the degradation of its client protein HER2 [46], we investigated the in vitro cytotoxicity of the geldanamycin derivatives (GA, 17-AAG, 17-DMAG, 17-HEAG, and star-GA) in both murine and human melanoma and breast cancer cell lines. Previous reports have demonstrated surprising in vitro cytotoxicity of geldanamycin analogues against human melanoma cell lines, given that most melanomas are considered to be chemoresistant [47]. Zhang et al. reported that a 11-methoxy-17-formyl-17-demethoxy-18-*O*-21-*O*-dihydrogeldanamycin analogue exhibited significant anticancer activity (IC_{50} ca. 496 nM) in the SK-MEL-2 human melanoma cell line [48]. Comparable results were observed with 17-AAG in two human melanoma cell lines with IC50 values of 21±5 nM and 13±2 nM in a BRAF mutant of SKMEL28 and the BRAF wild type CHL-1 cell lines [49]. Similar nanomolar range IC_{50} values were observed in both of our B16F10 murine and A2058 human melanoma cell lines. Even though the star-GA conjugate had substantially less toxicity in the B16F10 cells than the 17-

HEAG analogue, the star-GA conjugate was 24-fold more toxic than melphalan, the clinical chemotherapeutic used in ILP of melanoma. Similarly, the star-GA conjugate exhibited less toxicity than GA, 17-DMAG, and 17-AAG in the A2058 human melanoma cell line, but exhibited two orders of magnitude more toxicity than melphalan.

Tian et al. reported that in the SKBr3 cell line, a human HER2 over-expressing breast cancer, 17-AAG, 17-DMAG, and 17-HEAG all exhibited similar cytotoxicities, with IC_{50} values of 33±10, 24±8, and 50 nM, respectively [41]. Further, they all exhibited similar binding coefficients with human HSP90, with reported K_d values of 1.3, 0.5, and 0.8 μM, respectively [41]. Similarly, in our 4T1.2 Neu HER2 over-expressing breast cancer cell line, all of the GA derivatives exhibited similar toxicities with IC_{50} values slightly higher than Tian et al. reported, but still in the nanomolar range (Table 4.1). The low *in vitro* IC_{50} values of 17-HEAG combined with the similar *in vitro* HSP90 binding in comparison to GA (K_d= 0.24 μM) [50], along with the increased toxicity compared to melphalan in both the B16F10 and A2058 cell lines, we decided to proceed with in vivo efficacy studies of the star-GA conjugate in the B16F10, 4T1.2 Neu, and A2058 tumor models despite the short release half-life of 4 hr.

4.4.2 B16F10 Murine Melanoma Tumor Model

In the tumor optimization study, five difference cell concentrations were orthotopically implanted into the hind thigh of Balb/c mice. The lack of consistent tumor development below the 2.5×10^6 cells/animal concentration suggests that there is a minimum amount of B16F10 cells needed for to develop a palpable tumor in Balb/c mice. The 5.5×10^6 cells/animal concentration was chosen as the optimal cell concentration for the B16F10 tumor studies due to its reproducible tumor growth and development. Similar B16F10 tumor growth was observed by

Dirkx et al., where after implanting 10^6 cells subcutaneously into the flank of C57Bl/6 mice, the mice developed tumors of 1.5 cm within two to three weeks [51]. The primary tumor location of the hind flank is in contrast to most published reports of cell implantation into the hind footpad of mice to develop lymphatic metastases, where 2×10^5 cells are subcutaneously injected into the hind footpad and tumors develop to be 2 to 6 mm in diameter within three weeks [7,52,53]. However, the hind thigh was chosen for both humane reasons and as a representative model for localized melanoma. Whereas, implantation into the hind footpad not only limits the mobility of the mouse but also is less likely to be a representative model of the natural progression of melanoma metastases. The footpad model would be representative of a locally advanced lymphatic metastatic model and was developed to intentionally form metastases within the lymph nodes by nature of the subcutaneous cell injection, which allows the B16F10 cells to directly drain into the rich lymphatic network in the mouse footpads leading to popliteal metastases.

Recent reports with QDs, low MW Gd-DTPA, and indocyanine green liposomes have shown increased lymph flow to the SLN in the presence of B16F10 melanoma tumors [7,53,54]. However, these studies only looked at the short term effects on the lymphatic drainage (maximum of two hours), reporting up to a 23-fold increase in lymph flow to the popliteal node in tumor bearing mice two minutes post injection, which later decreased to a two-fold increase 30 min post injection [7]. Given that our HA conjugates are well-suited as sustained release drug carriers with a lymphatic absorption t_{max} of 1.5-2 hrs (74 kD, Figure 4.4 A and Table 4.2) and are retained within the lymph nodes for up to five days, the "downstream" effect of a B16F10 tumor on the lymph flow could not be fully characterized within the first two hours as with the previous reports. Further, the early studies only mentioned an increase in popliteal lymph flow, with no reference to the successive nodes (i.e. iliac).

We examined the effect of a B16F10 melanoma tumor on the lymphatic drainage of both the popliteal (Figures 4.4 A and C) and iliac (Figures 4.4 B and D) nodes using the optimized 74-kD HA-IR820 conjugate. A significant difference was observed in the kinetic profiles for the lymphatic drainage to the popliteal node between the tumor bearing and normal mice ($p=0.0320$, student t-test); however, there were no significant differences in the AUC for the popliteal nodes between the two groups (Table 4.2). The drainage from the popliteal node in tumor-bearing mice was almost three times slower than in the normal mice, whereas the drainage to the iliac node remained unchanged (Table 4.2). Furthermore the t_{max} in the popliteal and iliac nodes was unchanged for tumor-bearing mice compared to normal mice (Table 6). Contrary to the previously published results for liposomes, QDs, and Gd-DTPA, our results indicate similar uptake into the popliteal node regardless of tumor presence; although, the conjugate drains slower from the popliteal node in the presence of a tumor.

One possible reason for the differences in observed lymphatic drainage kinetics compared to the literature is due to the location of the primary tumor site (footpad vs. thigh). Our tumor model on the hind thigh of mice is representative of a localized limb melanoma, whereas the s.c. implantation of B16F10 cells into the footpad is more representative of a lymphatically advanced melanoma model with metastases within the lymph nodes. Further, this difference in tumor location may lead to induction of lymphangiogenesis at different sites leading to different drainage kinetics. As the footpad model has been reported to induce long range lymphangiogenesis within the popliteal lymph node, visualized by the increased lymphatic sinuses without lymphatic or blood vessel growth within the footpad tumor [7]. Another possible reason for the difference is that our conjugates are composed from a naturally occurring polymer, rather than "foreign materials" leading to a different retention mechanisms, such as strong interactions between HA and CD44 receptors on the surface of epithelial, mesenchymal, and lymphoid cells [55]. While the long retention of these conjugates within the sentinel lymph nodes of tumor-bearing animals may not be favorable to imaging, where rapid clearance is desired, it may benefit drug delivery applications. The lymphatic uptake of the HA-IR820 conjugate is not impeded by the presence of a large primary tumor and the conjugate is highly retained in the sentinel lymph node, which may facilitate sustained release of anti-cancer drugs from HA conjugates.

While our objective in this study was to develop an intralymphatic chemotherapy for the treatment of localized melanoma, the present star-GA conjugate does not exhibit increased efficacy over traditional i.v. melphalan. This is consistent with the literature, in that there are no published reports indicating that melanoma exhibits efficacious responses to 17-AAG as a single agent [56]. Although melphalan is unstable and exhibits significant systemic toxicities upon leakage from the ILP perfusate, our studies indicate that it still remains the most effective treatment of melanoma, exhibiting complete rapid (within 2 days post treatment) responses to treatment compared to non-treated animals (p=0.0068). Further, melphalan treated mice did not exhibit a relapse in tumor growth. Based on our *in vitro* toxicity results, we hypothesized that the geldanamycin treatments would exhibit improved efficacy over melphalan treatment; however, the *in vivo* results do not confirm these initial results. Although preliminary data discussed in Chapter 5 suggest that multiple dosing with geldanamycin derivatives may exhibit improved efficacy compared to the non-treated groups in B16F10 tumor bearing mice.

4.4.3 *4T1.2 Neu Murine Breast Cancer Tumor Model*

The pilot study with the treatment of murine breast cancer with 17-DMAG and star-GA demonstrated potentially positive efficacy results with the statistically significant differences in the delayed tumor growth on day 17 with the 17-DMAG and star-GA treatment groups compared to the non-treated group ($p<0.005$). It was hypothesized that if more animals were used in a follow-up study, that these differences would become more pronounced; however, with the addition of more animals in the study, the significance between these early differences in tumor growth proved to be insignificant. Further, no statistically significant differences were observed with any of the treatment groups. However, the use of a multiple dosing schedule is hypothesized to produce more distinct differences between the treatment groups as suggested in the pilot study. Multiple dosing over a period of weeks is commonly used in the clinic rather than a single dose as investigated in these studies. Preliminary data, discussed in Chapter 5, investigates the use of multiple dosing with geldanamycin derivatives to improve efficacy compared to the non-treated groups in 4T1.2 Neu tumor bearing mice.

However, in these studies, the maximum deliverable dose of the star-GA was increased by 5-fold compared to that of i.v. 17-DMAG, with no visual signs of toxicity. Further pathological examination is needed to determine the overall treatment related toxicities associated with the administration of the star polymer and star-GA compared to the liver toxicities often associated with geldanamycin administration [38,41]. Further immunohistopathology of the state of the enlarged spleens in this tumor model is worth investigating. In a similar 4T1 HER2 tumor model, both the spleen and livers were enlarged due to extramedullary hematopoiesis; further, the lungs (6/6), spleen (3/6) and liver (5/6) all exhibited metastases [57]

In addition to developing an intralymphatically delivered chemotherapeutic is the potential for reduction in the lymphatic metastatic potential. Although we did not observe any *in vivo* efficacy against the primary tumor growth of the 4T1.2 Neu tumor model, it is possible that the star-GA lymphatically targeted chemotherapeutic could prevent and/or treat lymphatic metastases. The 4T1.2 Neu tumor model is reported to be characteristic of spontaneous metastatic breast cancer with the formation of bone marrow metastasis within one week post implantation into the mammary fatpad [58]. Where the 4T1.2 tumor model metastasize by both the lymphatic and hematological routes, with metastases in the draining lymph nodes, lungs, and liver [59]. In order to investigate the metastatic state of the mice after treatment, the contralateral axillary lymph nodes were harvested, measured, and analyzed for the HER2 expression. No statistically significant differences were observed in the lymph node volume with all of the treatment groups; however, all of the axillary lymph nodes in the tumor bearing mice appeared to be enlarged compared to that of non-tumor-bearing mice. The HER2 expression was determined in the axillary lymph node samples; however, the HER2 expression was very low in all mice, suggesting that this tumor model was not metastatic at the end of this study.

It is possible that due to the limited size of the mice and the shear massiveness in the size of the tumors relative to the overall body size, that the primary tumor developed around or encompassed the metastatic lymph nodes, thus enabling their individual distinction for harvesting. Additional possibilities for the lack of HER2 expression in the axillary lymph nodes is that the tumor model did not reach a metastatic state by the end of the study (tumor volume = 2000 mm^3), the metastatic cells "lost" their ability to express HER2 (as this was a transfected gene), or the tumor model was not as metastatic as it was originally presented in the reported tumor model [58].

4.4.4 A2058 Human Melanoma Tumor Model

John et al. reported that two weeks post implantation of 5×10^6 A2058 cells into nude mice yielded a tumor 1-cm in diameter [60]. In contrast, the mouse injected with twice the A2058 cell concentration (1×10^7 cells) reported by John et al. developed a tumor 1 cm in diameter by day 16, whereas the implantation with 2×10^6 cells yielded a 1 cm tumor within 20 days. From the pilot study with the A2058 tumor model, we determined that for future studies, mice would be implanted with 1×10^7 cells/animal, in that tumors are visible in less than one week post implantation, but develop at a similar rate as the 2×10^6 cells/animal injection. The early visual conformation of successful tumor implantation in athymic mice is advantageous because the success rate of tumor implantation is often lower than that of "normal" mice, and the tumor growth progression is much slower in athymic mice compared to normal mice. The visualization of the inguinal lymph node tumor is promising in the development of a natural progressing lymphatically metastatic model for human melanoma.

Ideally, one would like to implant all mice in a study with the same concentration of cells, however this was a pilot study to determine if the A2058 tumor model responded to GA treatment. In order to minimize the amount of nude mice used, we decided to continue with the study using mice with different concentrations of implanted A2058 tumor cells. If positive results were observed, then future studies would be designed to utilize more animals per treatment group, and mice would be implanted with 1×10^7 cells/animal. However, as with the other two *in vivo* models, neither 17-DMAG nor star-GA exhibited efficacy in the A2058 tumor model (Figure 4.9). It is worth noting that the mouse treated with star-GA did show a slight decrease in tumor volume for a few days post treatment, however, the tumor continued to grow rapidly after the slight tumor recession (Days 16-20). It is possible that the mouse treated with star-GA did have a slight response to the treatment, however, this response was not significant compared to the non-treated mouse to progress with this conjugate in the A2058 tumor model. Mutiple dosing of 17-DMAG and/or the star-GA conjugate or improving the star-GA conjugate to be a sustained release formulation, could increase the efficacy of the geldanamycin treatment in this tumor model or the 4T1.2 Neu tumor model.

4.5 Conclusions

We developed a star-GA conjugate that exhibited increased solubility over the parent drug geldanamycin and had the potential to be delivered as a localized intralymphatic drug delivery system for the treatment of melanoma and breast cancers. Even though the release half-life of 17-HEAG from the star polymer was less than ideal, ca. 4 hrs *in vitro*, the potential for localization of the chemotherapeutic to the lymphatics still offered promising results as the star polymer drains rapidly (t_{max}= 45-50 min, Table 3.3) to the sentinel lymph node and successive nodes (popliteal $t_{50\%}$= 1.9 hr, and iliac t_{max}= 1 hr, Table 3.3) after s.c. administration, allowing for localized release of the 17-HEAG within the affected tumor draining lymphatic basin. On the other hand, we were able to significantly increase the deliverable dose of the geldanamycin analogue, 17-HEAG, from 10 mg/kg i.v. 17-DMAG to at least 50 mg/kg 17-HEAG without any visual signs of toxicity associated with the star polymer or 17-HEAG.

Despite the promising *in vitro* results with 17-DMAG, 17-HEAG, and star-GA treatment in the B16F10, A2058, and 4T1.2 Neu cell lines, none of the *in vivo* tumor models responded to treatment with the geldanamycin analogues either by i.v. or s.c. intralymphatic administration. Although it was expected that the geldanamycin analogues would offer some efficacy towards the melanoma and breast cancer *in vivo* tumor models, given that the literature has shown evidence of the efficacious responses to HSP90 inhibitors in HER2 positive *in vitro* and *in vivo* models [42], along with the reports that melanomas overexpress HSP90 and role in the progression of melanoma metastases [43,44], we unfortunately did not observe any response to treatment with a single dose of the geldanamycin analogues. It is possible that inhibition of the HSP90 pathway does not play a major role in the anti-proliferative pathways of these particular tumor models in that both melanoma and HER2 positive breast cancers are known to be resilient and develop chemoresistance [30,47]. It is possible that treatment of these tumor models would be feasible with geldanamycin analogues, if the release profile of the geldanamycin analogue was modified to exhibit more of a sustained release character; thus allowing for an increased exposure of the tumor to the chemotherapeutic. In addition, the use of a multiple dosing schedule could increase the chance of the geldanamycin analogue to reach the primary tumor and metastases. In a preliminary study with two mice, we found that treatment of mice bearing B16F10 tumors with three weekly doses of 17-DMAG i.v. exhibited a positive response to treatment, with a temporary halt in the tumor progression of one mouse, and tumor regression in the other mouse. Future studies to optimize the dosage and dosing schedule will be discussed in Chapter 5.

4.6 References

1. Nathanson, S.D., Insights into the mechanisms of lymph node metastasis. *Cancer* **2003**, *98*, 413-423.

2. Eccles, S.A.; Welch, D.R., Metastasis: Recent discoveries and novel treatment strategies. *Lancet* **2007**, *369*, 1742-1757.

3. Landry, C.S.; McMasters, K.M.; Scoggins, C.R., The evolution of the management of regional lymph nodes in melanoma. *J Surg Oncol* **2007**, *96*, 316-321.

4. Hellman, S.; Harris, J.R., The appropriate breast cancer paradigm. *Cancer Res* **1987**, *47*, 339-342.

5. Balch, C.M.; Gershenwald, J.E.; Soong, S.J.; Thompson, J.F.; Atkins, M.B.; Byrd, D.R.; Buzaid, A.C.; Cochran, A.J.; Coit, D.G.; Ding, S.L.*, et al.*, Final version of 2009 AJCC melanoma staging and classification. *J Clin Oncol* **2009**, *27*, 6199-6206.

6. Society, A.C., Facts & Figures 2011. In American Cancer Society: Atlanta, 2011.

7. Harrell, M.I.; Iritani, B.M.; Ruddell, A., Tumor-induced sentinel lymph node lymphangiogenesis and increased lymph flow precede melanoma metastasis. *Am J Pathol* **2007**, *170*, 774-786.

8. White, V.; Harvey, J.R.; Griffith, C.D.; Youssef, M.; Carr, M., Sentinel lymph node biopsy in early breast cancer surgery-working with the risks of vital blue dye to reap the benefits. *Eur J Surg Oncol* **2011**, *37*, 101-108.

9. Wagner, J.D.; Gordon, M.S.; Chuang, T.Y.; Coleman, J.J., 3rd, Current therapy of cutaneous melanoma. *Plast Reconstr Surg* **2000**, *105*, 1774-1799.

10. Essner, R., Experimental frontiers for clinical applications: Novel approaches to understanding mechanisms of lymph node metastases in melanoma. *Cancer Metast Rev* **2006**, *25*, 257-267.

11. Lens, M.B.; Dawes, M., Isolated limb perfusion with melphalan in the treatment of malignant melanoma of the extremities: A systematic review of randomised controlled trials. *Lancet Oncol* **2003**, *4*, 359-364.

12. Yoshimoto, Y.; Augustine, C.K.; Yoo, J.S.; Zipfel, P.A.; Selim, M.A.; Pruitt, S.K.; Friedman, H.S.; Ali-Osman, F.; Tyler, D.S., Defining regional infusion treatment strategies for extremity melanoma: Comparative analysis of melphalan and temozolomide as regional chemotherapeutic agents. *Mol Cancer Ther* **2007**, *6*, 1492-1500.

13. Bartlett, D.L.; Ma, G.; Alexander, H.R.; Libutti, S.K.; Fraker, D.L., Isolated limb reperfusion with tumor necrosis factor and melphalan in patients with extremity

melanoma after failure of isolated limb perfusion with chemotherapeutics. *Cancer* **1997**, *80*, 2084-2090.

14. Obach, R.S.; Lombardo, F.; Waters, N.J., Trend analysis of a database of intravenous pharmacokinetic parameters in humans for 670 drug compounds. *Drug Metab Dispos* **2008**, *36*, 1385-1405.

15. Chatterji, D.C.; Yeager, R.L.; Gallelli, J.F., Kinetics of chlorambucil hydrolysis using high-pressure liquid chromatography. *J Pharm Sci* **1982**, *71*, 50-54.

16. Raymond, A.K.; Beasley, G.M.; Broadwater, G.; Augustine, C.K.; Padussis, J.C.; Turley, R.; Peterson, B.; Seigler, H.; Pruitt, S.K.; Tyler, D.S., Current trends in regional therapy for melanoma: Lessons learned from 225 regional chemotherapy treatments between 1995 and 2010 at a single institution. *J Am Coll Surg* **2011**, *213*, 306-316.

17. Klaase, J.M.; Kroon, B.B.; van Geel, A.N.; Eggermont, A.M.; Franklin, H.R., Systemic leakage during isolated limb perfusion for melanoma. *Br J Surg* **1993**, *80*, 1124-1126.

18. Hocker, T.L.; Singh, M.K.; Tsao, H., Melanoma genetics and therapeutic approaches in the 21st century: Moving from the benchside to the bedside. *J Invest Dermatol* **2008**, *128*, 2575-2595.

19. Robert, C.; Thomas, L.; Bondarenko, I.; O'Day, S.; M, D.J.; Garbe, C.; Lebbe, C.; Baurain, J.F.; Testori, A.; Grob, J.J*., et al.*, Ipilimumab plus dacarbazine for previously untreated metastatic melanoma. *N Engl J Med* **2011**, *364*, 2517-2526.

20. Heuts, E.M.; van der Ent, F.W.; Hulsewe, K.W.; Heeren, P.A.; Hoofwijk, A.G., Incidence of axillary recurrence in 344 sentinel node negative breast cancer patients after intermediate follow-up. A prospective study into the accuracy of sentinel node biopsy in breast cancer patients. *Acta Chir Belg* **2007**, *107*, 279-283.

21. Giuliano, A.E.; McCall, L.; Beitsch, P.; Whitworth, P.W.; Blumencranz, P.; Leitch, A.M.; Saha, S.; Hunt, K.K.; Morrow, M.; Ballman, K., Locoregional recurrence after sentinel lymph node dissection with or without axillary dissection in patients with sentinel lymph node metastases: The american college of surgeons oncology group z0011 randomized trial. *Ann Surg* **2010**, *252*, 426-433.

22. Chu, K.U.; Turner, R.R.; Hansen, N.M.; Brennan, M.B.; Giuliano, A.E., Sentinel node metastasis in patients with breast carcinoma accurately predicts immunohistochemically detectable nonsentinel node metastasis. *Ann Surg Oncol* **1999**, *6*, 756-761.

23. Giuliano, A.E.; Dale, P.S.; Turner, R.R.; Morton, D.L.; Evans, S.W.; Krasne, D.L., Improved axillary staging of breast cancer with sentinel lymphadenectomy. *Ann Surg* **1995**, *222*, 394-401.

24. Querzoli, P.; Pedriali, M.; Rinaldi, R.; Lombardi, A.R.; Biganzoli, E.; Boracchi, P.; Ferretti, S.; Frasson, C.; Zanella, C.; Ghisellini, S*., et al.*, Axillary lymph node

nanometastases are prognostic factors for disease-free survival and metastatic relapse in breast cancer patients. *Clin Cancer Res* **2006**, *12*, 6696-6701.

25. Raj, K.A.; Marks, L.B.; Prosnitz, R.G., Late effects of breast radiotherapy in young women. *Breast Dis* **2005**, *23*, 53-65.

26. Takemura, G.; Fujiwara, H., Doxorubicin-induced cardiomyopathy from the cardiotoxic mechanisms to management. *Prog Cardiovasc Dis* **2007**, *49*, 330-352.

27. Force, T.; Krause, D.S.; Van Etten, R.A., Molecular mechanisms of cardiotoxicity of tyrosine kinase inhibition. *Nat Rev Cancer* **2007**, *7*, 332-344.

28. Slamon, D.J.; Godolphin, W.; Jones, L.A.; Holt, J.A.; Wong, S.G.; Keith, D.E.; Levin, W.J.; Stuart, S.G.; Udove, J.; Ullrich, A*., et al.*, Studies of the HER-2/neu proto-oncogene in human breast and ovarian cancer. *Science* **1989**, *244*, 707-712.

29. Slamon, D.J.; Clark, G.M.; Wong, S.G.; Levin, W.J.; Ullrich, A.; McGuire, W.L., Human breast cancer: Correlation of relapse and survival with amplification of the HER-2/neu oncogene. *Science* **1987**, *235*, 177-182.

30. Chow, A.; Arteaga, C.L.; Wang, S.E., When tumor suppressor TGFbeta meets the HER2 (ERBB2) oncogene. *J Mammary Gland Biol Neoplasia* **2011**, *16*, 81-88.

31. Greenberg, S.; Stopeck, A.; Rugo, H.S., Systemic treatment of early breast cancer--a biological perspective. *J Surg Oncol* **2011**, *103*, 619-626.

32. Murphy, C.G.; Fornier, M., HER2-positive breast cancer: Beyond trastuzumab. *Oncology (Williston Park)* **2010**, *24*, 410-415.

33. Chen, J.H.; Ling, R.; Yao, Q.; Li, Y.; Chen, T.; Wang, Z.; Li, K.Z., Effect of small-sized liposomal adriamycin administered by various routes on a metastatic breast cancer model. *Endocr Relat Cancer* **2005**, *12*, 93-100.

34. Cai, S.; Thati, S.; Bagby, T.R.; Diab, H.M.; Davies, N.M.; Cohen, M.S.; Forrest, M.L., Localized doxorubicin chemotherapy with a biopolymeric nanocarrier improves survival and reduces toxicity in xenografts of human breast cancer. *J Control Release* **2010**, *146*, 212-218.

35. Mendrek, B.; Trzebicka, B., Synthesis and characterization of well-defined poly(tert-butyl acrylate) star polymers. *Eur Polym J* **2009**, *45*, 1979-1993.

36. Cameron, D.J.A.; Shaver, M.P., Aliphatic polyester polymer stars: Synthesis, properties and applications in biomedicine and nanotechnology. *Chem Soc Rev* **2010**, *40*, 1761-1776.

37. Hult, A.; Johansson, M.; Malmström, E., Hyperbranched polymers. In *Branched polymers II*, Roovers, J., Ed. Springer Berlin / Heidelberg: 1999; Vol. 143, pp 1-34.

38. Porter, J.R.; Ge, J.; Lee, J.; Normant, E.; West, K., Ansamycin inhibitors of Hsp90: Nature's prototype for anti-chaperone therapy. *Curr Top Med Chem* **2009**, *9*, 1386-1418.

39. DeBoer, C.; Meulman, P.A.; Wnuk, R.J.; Peterson, D.H., Geldanamycin, a new antibiotic. *J Antibiot (Tokyo)* **1970**, *23*, 442-447.

40. Supko, J.G.; Hickman, R.L.; Grever, M.R.; Malspeis, L., Preclinical pharmacologic evaluation of geldanamycin as an antitumor agent. *Cancer Chemother Pharmacol* **1995**, *36*, 305-315.

41. Tian, Z.Q.; Liu, Y.; Zhang, D.; Wang, Z.; Dong, S.D.; Carreras, C.W.; Zhou, Y.; Rastelli, G.; Santi, D.V.; Myles, D.C., Synthesis and biological activities of novel 17-aminogeldanamycin derivatives. *Bioorg Med Chem* **2004**, *12*, 5317-5329.

42. Schulte, T.W.; Neckers, L.M., The benzoquinone ansamycin 17-allylamino-17-demethoxygeldanamycin binds to Hsp90 and shares important biologic activities with geldanamycin. *Cancer Chemother Pharmacol* **1998**, *42*, 273-279.

43. Fukuyo, Y.; Hunt, C.R.; Horikoshi, N., Geldanamycin and its anti-cancer activities. *Cancer Lett* **2009**, *290*, 24-35.

44. Tsutsumi, S.; Neckers, L., Extracellular heat shock protein 90: A role for a molecular chaperone in cell motility and cancer metastasis. *Cancer Sci* **2007**, *98*, 1536-1539.

45. Ullman-Cullere, M.H.; Foltz, C.J., Body condition scoring: A rapid and accurate method for assessing health status in mice. *Lab Anim Sci* **1999**, *49*, 319-323.

46. Gimenez Ortiz, A.; Montalar Salcedo, J., Heat shock proteins as targets in oncology. *Clin Transl Oncol* **2010**, *12*, 166-173.

47. Wagner, J.D.; Gordon, M.S.; Chuang, T.Y.; Coleman, J.J., 3rd, Current therapy of cutaneous melanoma. *Plast Reconstr Surg* **2000**, *105*, 1774-1801.

48. Zhang, H.; Sun, G.Z.; Li, X.; Pan, H.Y.; Zhang, Y.S., A new geldanamycin analogue from streptomyces hygroscopicus. *Molecules* **2010**, *15*, 1161-1167.

49. Beloueche-Babari, M.; Arunan, V.; Jackson, L.E.; Perusinghe, N.; Sharp, S.Y.; Workman, P.; Leach, M.O., Modulation of melanoma cell phospholipid metabolism in response to heat shock protein 90 inhibition. *Oncotarget* **2010**, *1*, 185-197.

50. Martin, C.J.; Gaisser, S.; Challis, I.R.; Carletti, I.; Wilkinson, B.; Gregory, M.; Prodromou, C.; Roe, S.M.; Pearl, L.H.; Boyd, S.M.*, et al.*, Molecular characterization of macbecin as an Hsp90 inhibitor. *J Med Chem* **2008**, *51*, 2853-2857.

51. Dirkx, A.E.; Oude Egbrink, M.G.; Kuijpers, M.J.; van der Niet, S.T.; Heijnen, V.V.; Bouma-ter Steege, J.C.; Wagstaff, J.; Griffioen, A.W., Tumor angiogenesis modulates leukocyte-vessel wall interactions in vivo by reducing endothelial adhesion molecule expression. *Cancer Res* **2003**, *63*, 2322-2329.

52. Ruddell, A.; Harrell, M.I.; Minoshima, S.; Maravilla, K.R.; Iritani, B.M.; White, S.W.; Partridge, S.C., Dynamic contrast-enhanced magnetic resonance imaging of tumor-induced lymph flow. *Neoplasia* **2008**, *10*, 706-713.

53. Proulx, S.T.; Luciani, P.; Derzsi, S.; Rinderknecht, M.; Mumprecht, V.; Leroux, J.C.; Detmar, M., Quantitative imaging of lymphatic function with liposomal indocyanine green. *Cancer Res* **2010**, *70*, 7053-7062.

54. Ruddell, A.; Harrell, M.I.; Minoshima, S.; Maravilla, K.R.; Iritani, B.M.; White, S.W.; Partridge, S.C., Dynamic contrast-enhanced magnetic resonance imaging of tumor-induced lymph flow. *Neoplasia* **2008**, *10*, 706-713.

55. Liu, N.F., Trafficking of hyaluronan in the interstitium and its possible implications. *Lymphology* **2004**, *37*, 6-14.

56. Dimopoulos, M.A.; Mitsiades, C.S.; Anderson, K.C.; Richardson, P.G., Tanespimycin as antitumor therapy. *Clin Lymphoma Myeloma Leuk* **2011**, *11*, 17-22.

57. Tao, K.; Fang, M.; Alroy, J.; Sahagian, G.G., Imagable 4T1 model for the study of late stage breast cancer. *BMC Cancer* **2008**, *8*, 228.

58. Kim, J.H.; Majumder, N.; Lin, H.; Chen, J.; Falo, L.D., Jr.; You, Z., Enhanced immunity by NeuEDhsp70 DNA vaccine is needed to combat an aggressive spontaneous metastatic breast cancer. *Mol Ther* **2005**, *11*, 941-949.

59. Aslakson, C.J.; Miller, F.R., Selective events in the metastatic process defined by analysis of the sequential dissemination of subpopulations of a mouse mammary tumor. *Cancer Res* **1992**, *52*, 1399-1405.

60. John, C.S.; Bowen, W.D.; Saga, T.; Kinuya, S.; Vilner, B.J.; Baumgold, J.; Paik, C.H.; Reba, R.C.; Neumann, R.D.; Varma, V.M.*, et al.*, A malignant melanoma imaging agent: Synthesis, characterization, in vitro binding and biodistribution of iodine-125-(2-piperidinylaminoethyl)4-iodobenzamide. *J Nuc Med* **1993**, *34*, 2169-2175.

Chapter 5. Summary and Future Work

5.1 Summary

With the development of the HA-Texas Red conjugate we were able to visualize the HA conjugates drain from the injection site around the tumor, confirming our hypothesis that peritumoral injections of HA could potentially deliver chemotherapeutics to tumors via the lymphatics. However, the use of Texas Red was not optimal for deep tissue penetration and large signal to noise ratios, so we decided to pursue a different fluorescent dye in the NIR range, IR820. A series of six different molecular weight HA-IR820 conjugates were synthesized with similar dye loading degrees (ca. 5 % wt/wt). The size of HA was optimized for lymphatic delivery utilizing whole body fluorescent imaging using the series of HA-IR820 conjugates. From the kinetic and cumulative fluorescent data obtained after the image fluorescence analysis, it was determined that 74-kD HA (30-50 nm) was the optimal MW for lymphatic delivery of HA conjugates. This was consistent with the optimal reported liposomal size (40 nm) for lymphatic uptake after s.c. administration [1]. The 74-kD HA-IR820 conjugate drained at a similar rate to both the popliteal and axillary lymph nodes after injections into the footpad and forearm, respectively, with a t_{max} of ca. 2 hr. Furthermore, it was found that the HA conjugates are highly retained by the lymph nodes with $t_{50\%}$ of 6.9, 21, and 15 hrs for the popliteal, iliac, and axillary lymph nodes, respectively. Hyaluronan would be an effective carrier for sentinel lymph node drug delivery as the HA-IR820 conjugate is cleared relatively slowly from the axillary and popliteal nodes.

One issue with the development of HA conjugates is due to the increased viscosities associated with increasing the MW and concentrated HA solutions, along with the limited drug loading degrees due to issues with the solubility and biocompatibility. Therefore we sought to develop a new biodegradable star polymer with variable degrees of anionic charges, to be used as a new lymphatic carrier for imaging and drug delivery. Rao et al. examined the effect of varying the negative charge on the lymphatic uptake of PLGA nanoparticles [2], but this is the first study using defined-structure polymers while varying the negative charge . The authors varied the ratio carboxylic acid terminated to uncharged polymers in their preparation of nanoparticles and determined that an increase in the anionic character of the nanoparticles led to increased lymphatic uptake, both in the SLN and cumulative draining lymph nodes. After fully characterizing the star polymer with four degrees of anionic charge, we found that the polymer is less toxic in vitro than other polyanionic and polycationic polymers used for drug and gene delivery. Further, the star polymer was significantly less viscous than HA solutions, with viscosities similar to that of water (1 Pa·s). A linear decrease in the zeta potential, with respect to the increase in the anionic character, was observed. Although no significant differences were found in the total cumulative drainage of the 40-90 wt% acid star polymers, large differences in the elimination half times for the popliteal and iliac lymph node were observed. Sixty weight percent acid conjugation on the star polymer was determined to be the optimal star polymer formulation for lymphatic delivery using whole body fluorescent imaging, due to its rapid drainage from the popliteal node ($t_{50\%}$ = 1.9 hrs) and increased retention in the iliac node ($t_{50\%}$ = 19 hrs). The results suggest that the 60% wt acid-star polymer would be an ideal candidate for deep lymphatic drug delivery to the subsequent lymph nodes.

After optimizing the star polymer using star-IR820 with in vivo fluorescent imaging, we developed a star-geldanamycin analogue (17-HEAG) conjugate, with 15% wt/wt drug loading, for the treatment of localized melanoma and breast cancer. It was found that the release half-life of the 17-HEAG from the star-GA conjugate was 4 hr, which is shorter than ideal for sustained drug release. However, the in vitro data suggested that the conjugate along with 17-DMAG exhibited cytotoxicity against the B16F10, A2058, and 4T1.2 Neu cell lines, so we decided to proceed with treatment in the in vivo tumor models. However, the 17-DMAG (i.v.) and star-GA formulations did not exhibit any response or a significant tumor regression in all three of the in vivo tumor models (B16F10, A2058, and 4T1.2 Neu). This suggests that either these rapid growing tumor models do no respond to HSP90 inhibitors in vivo or the 17-HEAG released too rapidly from the star polymer before the star-GA conjugate was able to reach the tumor to elicit a sufficient tumor response.

In conclusion, we optimized both the size and charge of two different carriers for the use in intralymphatic imaging and drug delivery. Further, we developed a new biodegradable, less viscous, and water soluble star polymer as a potential carrier for use in lymphatic drug delivery. Hyaluronan may be useful for SLN lymphatic drug delivery, whereas the star polymer may be more useful for deep lymphatic drug delivery. Even though our initial studies with the star-GA conjugate did not delay the tumor progression in the three in vivo tumor models, promising preliminary results show that we may have developed a new multiple dosing treatment option for melanoma, which is a fast growing, resistant disease, for which there are little treatment options if the tumor is not detected and removed early.

5.2 Future Work

5.2.1 Further Optimization of Lymphatic Carriers and Imaging Agents

For future multimodal lymphatic imaging and drug delivery, it would be advantageous to develop a new NIR dye rather than continue using the IR820 dye utilizing an amino group on the linker to displace the chloride (Figures 5.1 A, B, and C). After developing the series of HA-IR820 conjugates, we observed red shifts in the UV absorbance post derivatization of the dye, leading to suboptimal absorbance and fluorescence wavelengths for in vivo imaging. Further, it was found that at high concentrations (e.g. > 0.1 mg/mL IR820), the IR820 dye has the tendency to self-quench leading to reduced fluorescence signals both in vitro and in vivo and limiting the detection of the fluorescent conjugates only at low concentrations. Preliminary work is under way to develop a new derivative of the IR820 dye, which utilizes a thiol group (Figure 5.1 D) rather than an amine (Figures 5.1 B and C) to replace the chloride (Figure 5.1 A). The use of the sulfur in the linker moiety leads to similar UV absorbance and fluorescence spectra (data not shown) as the original IR820, rather than the blue shifts seen for the amino group on the linkers used for HA-IR820 and star-IR820. This is because sulfur is more electron donating, unlike the nitrogen, which destabilizes the conjugated system leading to a shift in the UV absorbance and fluorescence. However, the photostability and quenching characteristics of the new thiol IR820 derivative have not yet been studied. If the new derivative appears to be photo-unstable or quenched, other fluorescent NIR dyes, can be investigated for the use of in vivo fluorescent imaging. One such dye could be the Cy7-NHS ester, which is photostable, easy to conjugate to the polymers, and exhibits bright fluorescence in the NIR range ($\lambda_{ex}/\lambda_{em}$ = 750/773 nm, ε = 199,000 cm^{-1} M^{-1}).

Further, it is likely that the MW/size of the star polymer used in the optimization of the anionic charge was not optimal for lymphatic delivery. The MWs of the star polymers used were approximately 54 kD, 63 kD, 72 kD, and 85.5 kD for the 20, 40, 60 and 90% acid-star polymers, respectively; however these differences in the MW are due to the addition of succinic acid on the sugar moieties along the polymer backbone, which is unlikely to change the overall size significantly. Due to difficulties in optimizing the conditions needed for sizing small particles by dynamic light scattering, the accurate size identification was not conducted for the star polymers; however, it is likely that similar to the size of 6.4 kD HA (ca. 10 nm) based on similar elution times using SEC. Further optimization of the size of the star polymers would be advantageous, in order to maximize the lymphatic uptake of these delivery platforms. The optimization could easily be done in a similar manner as with the IR820-polymer conjugates using whole body fluorescent imaging. However, one limitation to this study is that multiple different MW (at least 2 to 3 additional MW) star polymers must first be synthesized prior to the imaging studies.

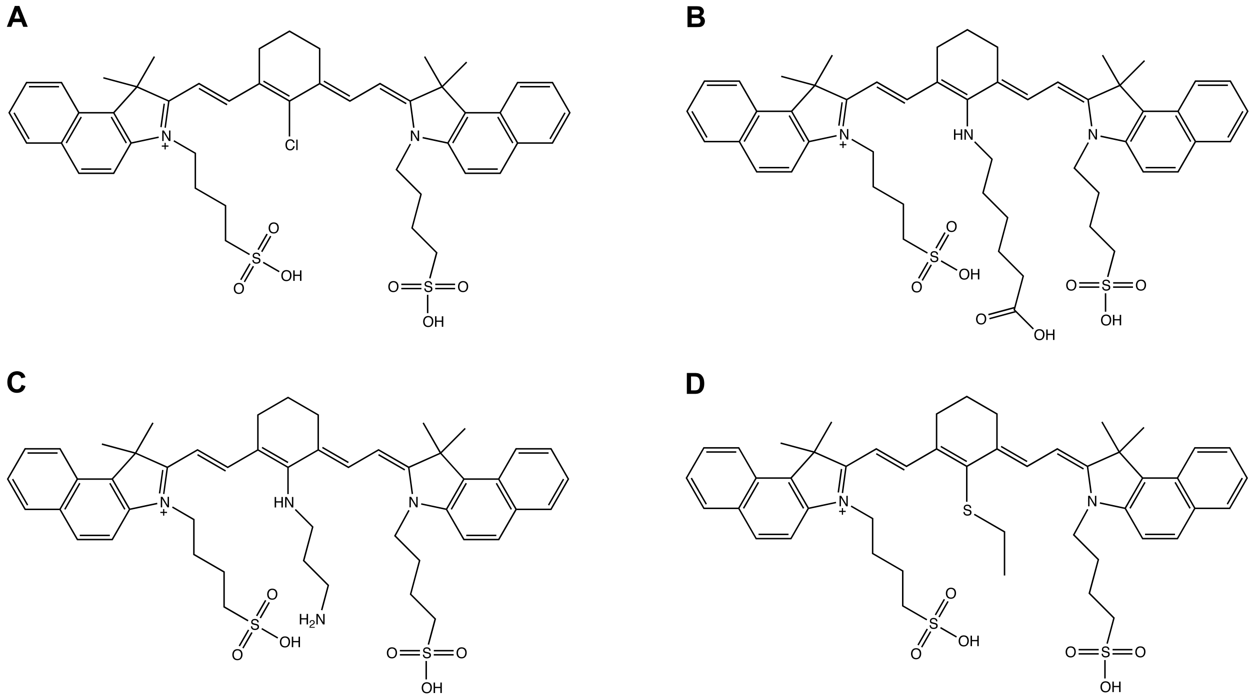

Figure 5.1. Chemical structures of A) IR820, B) 5-carboxypentyl-amino-IR-820 (used in HA-IR820), C) 3-aminopropyl-amino-IR820 (used in star-IR820), and D) ethylthiol-IR820.

5.2.2 Future Optimization of the Star-GA Conjugates and Dosing Regimens

Two possible ways to test if an increased exposure to the GA analogue would result in a tumor response are to 1) treat animals with multiple doses of the GA analogues, either with 17-DMAG or the current star-GA conjugate, and 2) develop an actual sustained release formulation of the star-GA conjugate by modifying the linker between GA and the star polymer. To determine whether increased exposure to the GA drug would improve the outcome, we determined the in vitro toxicity of GA, 17-DMAG, and star-GA at multiple exposure times (24, 48, and 72 hr) in the B16F10, A2058 and 4T1.2 Neu cell lines. The preliminary results suggest that increased incubation with the GA analogues elicits a greater cytotoxic response, indicated by decrease in IC_{50} values with increased exposure times (Table 5.1). Some of the IC_{50} results suggest that the analogues are more toxic when incubated for 48 hr compared to 72 hrs, however, this study was only conducted once and statistical significance could not be determined. Further repetitions of these cytotoxicity assays may validate the observed trend, however, with the limited replicates presented, it is not possible to determine if results are real or experimental error. On the other hand, it is clear, that prolonged exposure of more than 24 hrs does result in a higher cytotoxic response.

IC_{50}

Treatment	B16F10	A2058	4T1.2 Neu
Geldanamycin	35 nM 105 nM 1 μM	44 nM 2.2 μM 3.6 μM	250 nM 175 nM 890 nM
17-DMAG	250 nM 110 nM 3.6 μM	44 nM 3.8 μM 5.4 μM	300 nM 140 nM 1.6 μM
Star-GA (15% GA)	290 nM 450 nM 3.7 μM	700 nM 2.7 μM 11.2 μM	335 nM 310 nM 1.3 μM

Table 5.1. IC_{50} values of geldanamycin, 17-DMAG, and star-GA (15% GA) in B16F10, A2058, and 4T1.2 Neu cell lines with drug exposure times of 72 hr (blue), 48 hr (red), and 24 hr (green).

With the promising results from this preliminary study, we decided to determine whether multiple i.v. dosing of 17-DMAG would result in a delay in the tumor growth of the two murine tumor models, B16F10 and 4T1.2 Neu. Mice were treated with three weekly doses of 17-DMAG (5 mg/kg i.v., 1:1 DMSO:PBS), and the tumor growth was measured and compared to the tumor growth discussed in Chapter 4 for the non-treated and single dosed i.v. 17-DMAG. B16F10 tumor bearing mice (n=2) responded to multiple 17-DMAG dosing (Figure 5.2 A), whereas the 4T1.2 Neu tumor bearing mouse (n=1) did not exhibit a different response compared to a single dose of 17-DMAG (Figure 5.2 B). One of the B16F10 tumor bearing mice with multiple treatments exhibited a ten-day delay in tumor growth, whereas the other mouse exhibited significant tumor regression by doubling its life expectancy (>44 days compared to 19 days). The mouse exhibiting increased survival was euthanized since the approved study period (45 days) had concluded.

Further investigation with multiple dosing of the current star-GA formulation, along with the use of more animals in the 17-DMAG group is needed. Treatment with 10 mg/kg (MTD), rather than the 5 mg/kg used in this study, in three weekly doses may provide additional tumor responses to the observations seen with the 5 mg/kg dose. The animals in this study were limited to three weekly doses with i.v. 17-DMAG, as the mouse's tail needed at least five days between treatments to heal due to the extravasation of the DMSO causing necrosis. Further, a more frequent subcutaneous dosing schedule should be investigated for increased tumor responses, as the healing time is not necessary for s.c. injections as with i.v. injections. Further optimization of the linker would be potentially useful also to achieve sustained release of the GA analogue while the carrier is localized in the draining lymph nodes. Since the hydrolysis of the existing ester bond between GA and the star polymer results in rapid release of GA (4 h release half-life), future studies may us a long-lived pH-sensitive or tumor activated linker, such as a dihydrazide, peptide, or enzymatically cleavable linker. Dr. Cai in our laboratory has previously employed a dihydrazide linker for the sustained release of doxorubicin from HA in which the release half-life decreased with decreasing pH, resembling that of the hypoxic tumor environment [3]. Pathological examination of the tissues of mice treated with the star polymer would provide insight as to if these new biodegradable star polymers are indeed less toxic than their dendrimer counterparts. Additionally, since GA is known to induce liver toxicity, pathology studies of the animal liver tissues in the 17-DMAG and star-GA treatment groups would determine if the star polymer also reduces the liver toxicity associated with GA treatment.

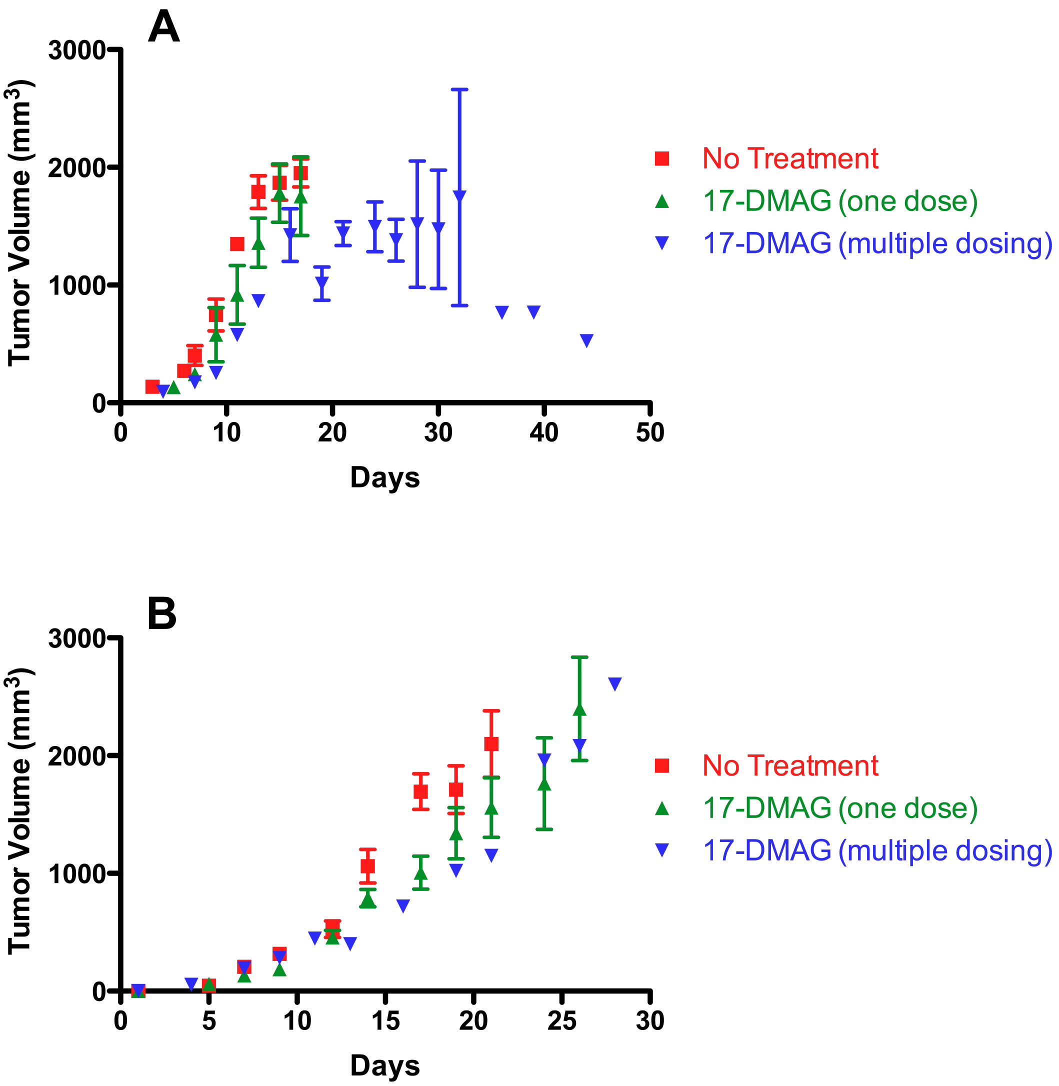

Figure 5.2. Tumor growth curves of mice bearing A) B16F10 were treated with no treatment (red, n=4), one dose of 17-DMAG (i.v . 15 mg/kg, green, n=4), or three weekly doses of 17-DMAG (i.v. 3 × 5 mg/kg, blue, n=2); or B) 4T1.2 Neu tumors were treated with no treatment (red, n=7), one dose of 17-DMAG (i.v . 10 mg/kg, green, n=7), or three weekly doses of 17-DMAG (i.v. 3 × 5 mg/kg, blue, n=1). Tumor volume = 0.52×(width)^2×(length).

5.3 References

1. Oussoren, C.; Storm, G., Lymphatic uptake and biodistribution of liposomes after subcutaneous injection: III. Influence of surface modification with poly(ethyleneglycol). *Pharm Res* **1997**, *14*, 1479-1484.

2. Rao, D.A.; Forrest, M.L.; Alani, A.W.; Kwon, G.S.; Robinson, J.R., Biodegradable PLGA based nanoparticles for sustained regional lymphatic drug delivery. *J Pharm Sci* **2010**, *99*, 2018-2031.

3. Cai, S.; Thati, S.; Bagby, T.R.; Diab, H.M.; Davies, N.M.; Cohen, M.S.; Forrest, M.L., Localized doxorubicin chemotherapy with a biopolymeric nanocarrier improves survival and reduces toxicity in xenografts of human breast cancer. *J Control Release* **2010**, *146*, 212-218.

Appendix 1. Synthesis of 4-Arm-Acid-Star Polymers

The following sections describe the detailed synthesis of the acid-star polymers utilized in Chapters 3 and 4 described in this dissertation. The MADIX agent was synthesized based on the procedure reported previously [1]. The RAFT agent was synthesized according to the procedure reported previously [2].

A.1 Materials

Unless noted otherwise, all reagents and solvents were purchased from Sigma Aldrich and used without further purification. ^{1}H-NMR (400 MH$_z$) and ^{13}C-NMR (100 MH$_z$) spectra were collected on a Bruker DRX 400 spectrometer using compounds dissolved in $CDCl_3$, MeOD or D_2O. Chemical shifts were referenced to δ7.28 and 77.0 ppm for ^{1}H-NMR and ^{13}C-NMR spectra, respectively. High-resolution mass spectrometry (HRMS) data were generated after flow injection analysis (FIA) manually matching peaks on an Applied Biosystems Mariner TOF spectrometer with a turbo-ionspray source.

A.2 Synthesis of Acid-Star Polymers

A.2.1 Synthesis of the Bromide Intermediate Compound (Scheme 3.1)[1]

Pentaerithol (1.36 g, 10 mmol) was dissolved in 25 mL of dry chloroform and 2.5 mL of pyridine and cooled to 0 ^{o}C. The 2-bromo propionyl bromide (10.01 g, 45 mmol) was added dropwise, and the reaction proceeded at ambient temperature (ca. 23°C) for 48 hours. The mixture then was neutralized with aqueous HCl (10 wt %). Then the organic phases were washed with water, sodium bicarbonate solution (5%), and brine, followed by drying with sodium sulfate. Evaporation of the solvent under reduced pressure yielded the desired bromide intermediate compound, and the molecular structure was verified by ^{1}H-NMR and compared with the reported data. The reaction yielded 4.89 g of the desired bromide intermediate compound was obtained with a yield of 72%. ^{1}H-NMR ($CDCl_3$, 400 MHz) δ: 1.85 (d, 12 H, J = 7.0), 4.22-4.23 (m, 4H), 4.33-4.39 (m, 4H), 4.41 (q, 4 H, J = 7.0). The chemical shifts are consistent with the structure and no impurities or unknown peaks were observed.

A.2.2. Synthesis of the MADIX Agent (Scheme 3.1)

A solution of the bromide intermediate compound (2.028 g, 3.0 mmol) in chloroform (45 mL) was treated with a 10-fold excess of *O*-ethylxanthic acid, potassium salt (5.01 g, 30 mmol). The mixture was stirred at ambient temperature for 3 days, and the resulting suspension was filtered and washed with chloroform. Evaporation of the solvent followed by purification through a flash column on silica gel using 3:7 ethyl acetate:hexanes as eluents yielded the desired compound, and the molecular structure was verified by ^{1}H-NMR and compared with the reported data.

A.2.3. Synthesis of the RAFT Agent, 1,2;3,4-di-O-isopropylidene-6-O-acryloyl-α-D-galactopyranose (Scheme 3.2) [2]

To a 100-mL round bottom flask *1,2,3,4-di-O*-isopropylidene-*6-O*-acryloyl-*α-D*-galactopyranose (1.39 g, 5.20 mmol), basic alumina (2.44 g, 23.92 mmol), 20 mL of dry acetonitrile, and acryloyl chloride (2.26 mL, 27.04 mmol), were added dropwise. After stirring under argon for 3 days at ambient temperature, the mixture was filtered through a thin layer of celite, and the solids were washed with 50 mL of acetonitrile. The combined organic layers were concentrated under reduced pressure. The resulting pale yellow residue was purified through a flash column using 1:2 ethyl acetate:hexanes as eluents, and its molecular structure was verified by ^{1}H-NMR and compared with the reported data. The desired RAFT agent was obtained with a yield of 100%. ^{1}H-NMR ($CDCl_3$, 400 MHz) δ: 1.44 (t, 12 H, J = 7.0), 1.60 (d, 12 H, J = 7.2), 4.12-4.22 (m, 8H), 4.44 (q, 4 H, J = 7.2), 4.66 (q, 8 H, J = 7.0). The peak shifts were consistent with the structure and suggested that the compound was pure.

A.2.4. Synthesis of the Protected Sugar-Star Polymer, poly-(1,2:3,4-di-O-isopropylidene-6-O-methacryloyl-α-D-galactopyranose) by MADIX/RAFT Polymerization (Scheme 3.2)

The *1,2,3,4-di-O*-isopropylidene-*6-O*-acryloyl-*α-D*-galactopyranose (3.11 g, 9.9 mmol) was treated with basic alumina and 10 mL of dry α, α, α- trifluorotoluene in a 50-mL round bottle flask. The RAFT agent (0.054 g, 0.0622 mmol) was added to the solution, followed by the addition of AIBN (1.36 mg, 0.00827 mmol), and the reaction flask was placed on ice and purged with argon for 30 min. The flask was then transferred to a thermostatic oil bath at 70 °C for ca. 10 hrs. The mixture was cooled in an ice bath and poured into cold diethyl ether to obtain the precipitate followed by concentration under reduced pressure. The molecular structure and molecular weight of the resulting polymer were determined by ^{1}H-NMR and size exclusion chromatography (SEC), respectively. ^{1}H-NMR (D_2O, 400 MHz) δ: 1.29-2.05 (brs, 1 H), 2.17-2.74 (brs, 2 H), 3.45-4.17 (brs, 6H), 5.26 (brs, 1 H).

A.2.5. Deprotection Reaction to Form the Sugar-Star-Polymer, the Multi-Arm poly-(6-O-methacryloyl-D-galactose) (Scheme 3.2)

The poly-(*1,2:3,4-di-O*-isopropylidene-*6-O*-methacryloyl-α-*D*-galactopyranose) (500 mg) was dissolved in 100 mL of 90% formic acid. The solution was stirred at 60 °C for 24 hours. The solution then was dialyzed (10 kDa MWCO dialysis tubing, Pierce, Rockford, IL) against distilled water for 2 days with water changes every 6 hours to remove the acid. After dialysis, the resulting polymer was lyophilized to obtain the desired multi-arm poly-(*6-O*-methacryloyl-*D*-galactose) (Scheme 3.2). ^{1}H-NMR (D_2O, 400 MHz) δ: 1.29-2.05 (brs, 1 H), 2.17-2.74 (brs, 2 H), 3.45-4.17 (brs, 6H), 5.26 (brs, 1 H).

A.2.6. Modification of Multi-Arm poly-(6-O-methacryloyl-D-galactose) with Succinic Anhydride to Yield the Acid-Star-Polymers

Polymers with increasing degrees of succination (20%, 40%, 60% and 90%) were generated by reacting the star poly-(*6-O*-methacryloyl-*D*-galactose) (100 mg) with succinic anhydride (20, 40, 60 and 90 mg, respectively) in 20 mL of dry dimethyl formaldehyde (Scheme 3.3). The mixtures were stirred at ambient temperature to form a homogeneous solution, followed by dropwise addition of 5 mL of dry pyridine. After 2 days, the solutions were dialyzed (10 kDa MWCO dialysis tubing) against 50% ethanoic water for 1 day followed by absolute ethanol for 1 day, with solvent changes every 6 hrs to remove the dimethyl formaldehyde, pyridine, and other small molecule impurities. The solvent of the resulting solution was removed under reduced pressure, which led to the desired sugar multi-arm polymers with increasing substitution degrees of carboxylic acids. ^{1}H NMR (D_2O, 400 MHz) δ: 1.29-2.05 (brs, 1 H), 2.17-2.74 (brs, 2 H, methylene protons from the sugar polymer and the succinic acid portion overlapped), 3.45-4.17 (brs, 6H), 5.26 (brs, 1 H).

A.3 References

1. Stenzel, M.H.; Davis, T.P.; Barner-Kowollik, C., Poly(vinyl alcohol) star polymers prepared via MADIX/RAFT polymerization. *Chem Commun (Camb)* **2004**, 1546-1547.
2. Ting, S.R.; Gregory, A.M.; Stenzel, M.H., Polygalactose containing nanocages: The RAFT process for the synthesis of hollow sugar balls. *Biomacromolecules* **2009**, *10*, 342-352.